

**Doctoral Dissertation
(Shinshu University)**

**Study on development of novel
materials for organic
light-emitting diodes based on
hole conducting substituents and
their device application**

March 2021

HU Baohua

(胡 葆華)

Catalogue

ABSTRACT	5
Chapter 1 Introduction	9
I . Introduction	10
II. Development of OLED display technology	11
III. Development and application of hole conduction characteristic groups	17
III-1. Application of hole conduction characteristic groups in OPCs.....	17
III-2. Application of hole conduction characteristic groups in OFETs	20
III-3. Application of hole conduction characteristic groups in PSCs	21
III-4. Application of hole conduction characteristic groups in OLEDs.....	22
IV. Research on new OLED materials based on the application of hole conducting groups.....	23
IV-1. TDATA series with triphenylamine (TPA) as the core	24
IV-2. TDAB series with benzene as the core.....	26
IV-3. TPB series with N,N,N',N'-Tetraphenylbenzidine (TPB)....	26
IV-4. N,N,N',N'-Tetraarylaryl diamines series	27
IV-5. The series with Carbazole as the core.....	28
IV-6. The series with Spiral ring.....	29
IV-7. Other types of hole transport materials.....	30
Chapter 2 Design, synthesis and application of hole-conducting materials contain Spiro group	37
I . Introduction.....	37
II. Experiment content.....	39
II-1. Material structures and instrument	39
II-2. Synthesis and characterization	40
II-3. OLED fabrication and measurements.....	44

III. Results and discussion	46
III-1. Simulation of Homo and LUMO values.....	46
III-2. Photophysical properties.....	47
III-3. Electrochemical properties.....	49
III-4. Thermal stability.....	49
III-5. Device application of Spiro compounds.....	50
IV. Chapter summary	59
Chapter 3 Design and synthesis of new EB materials and its application in OLED devices.....	69
I . Introduction.....	70
II. Experiment content.....	71
II-1. Material structure and instrument	71
II-2. Synthesis and characterization	73
II-3. OLED fabrication and measurements.....	77
III. Results and discussion	78
III-1. Theoretical calculation	78
III-2. Photophysical properties.....	78
III-3. Electrochemical properties.....	80
III-4. Thermal properties	80
III-5. Device application of newly designed EB compounds.....	82
IV. Chapter summary	86
Chapter 4 Synthesis and Properties of Diphenylamine/ Xanthone Hybrid Organic Light Emitting Materials	95
I . Introduction.....	96
II. Experiment content.....	98
II-1. General information.....	98
II-2. Synthesis and characterization	99
II-3. Fabrication of PHOLEDs	103
III. Results and discussion	104
III-1. Theoretical calculation.....	104

III-2. Photophysical properties	106
III-3. Thermal analysis.....	109
III-4. Electroluminescent (EL) properties	110
III-5. Device optimization	112
IV. Conclusion.....	117
Chapter 5 High-refractive-index capping layer improves top-light-emitting device performance	127
I . Research background of capping layer materials.....	128
II. Experiment content.....	130
II-1. Materials and measurements	130
II-2. Synthesis and characterizations	131
II-3. Fabrication and electroluminescence measurement of TEOLEDs.....	134
III. Results and discussion	135
III-1. Photophysical properties	135
III-2. Thermal performances.....	136
III-3. Electroluminescence characteristics	137
IV. Conclusion.....	140
Conclusion	147
Acknowledgment	149
Appendix.....	150

ABSTRACT

Organic light-emitting diodes (OLEDs) has the characteristics of low driving voltage, high brightness, wide viewing angle, fast response speed and simple manufacturing process. It is known as the new generation of flat panel display technology, especially in the field of solid-state lighting and small and medium size display. At present, the key problems hindering large-scale marketization are low luminous efficiency, short lifetime and poor performance stability. Therefore, further development of high efficiency and long lifetime electroluminescent materials is still the main goal of current and future research work. In this paper, a series of novel electron blocking materials, phosphorescent host materials and capping layer materials are studied, and a series of materials are designed and synthesized, and their devices performance is characterized; further, the preparation of high efficiency top light-emitting diodes is also studied. The following is a brief introduction to the main contents of each chapter:

1. In the first chapter, the history and development status of OLEDs are introduced. In this paper, the new hole-transport type materials are reviewed from the aspects of material application direction and molecular structure characteristics. And the main research contents of this paper are summarized.

2. In the second chapter, we synthesized **BFS2A**, **BFS3A**, **SF2DDA** and **SF4DDA**, and applied them as electron blocking materials in OLEDs. Among them, the core of **BFS2A** and **BFS3A** is cyclo spiro, and the core of **SF2DDA** and **SF4DDA** is spirofluorene. When the film thickness of **BFS2A** and **BFS3A** is 50nm and the current density is $10 \text{ mA}\cdot\text{cm}^{-2}$, the maximum current efficiency of **BFS2A** and **BFS3A** are $10.46 \text{ cd}\cdot\text{A}^{-1}$ and $9.26 \text{ cd}\cdot\text{A}^{-1}$, respectively, and the lifetime (LT90) is 1592 hours and 1805 hours respectively. When the film thickness of **SF2DDA** and **SF4DDA** is 20nm and the current density is 10

$\text{mA}\cdot\text{cm}^{-2}$, the maximum current efficiency of **SF2DDA** and **SF4DDA** are $9.81 \text{ cd}\cdot\text{A}^{-1}$ and $10.00 \text{ cd}\cdot\text{A}^{-1}$, respectively, and the lifetime (LT90) is 430 hours and 420 hours, respectively. The experimental results show that compared with the traditional electron blocking materials **SF2AF** and **SF4AF**, the above compounds can effectively improve the device efficiency and lifetime.

3. In the third chapter, we synthesized **DFBDDba**, **BDFPDba** and **BDFPDca** by changing the structure of dimethyl-dihydroacridofuran as the basic unit, and applied them as electron blocking materials in OLEDs. These materials exhibit excellent photophysics properties and thermal stability, and have high triplet energy levels, which can effectively improve the external quantum efficiency and lifetime of devices. At $10 \text{ mA}\cdot\text{cm}^{-2}$, the external quantum efficiency (EQE) of the device based on **DFBDDba** reaches 7.15%, and the lifetime of the device reaches 277 hours (LT90), which is 8 times longer than that of the device based on **TCTA**. The experimental results show that compared with the traditional electron blocking material **TCTA**, the above compounds can effectively improve the device efficiency and lifetime.

4. In Chapter 4, we synthesized **XanCarDipha**, **p-XanCarDipha** and **m-XanCarDipha** by changing the branched chain structure of Xanthone, which were used as main materials in green phosphorescent OLEDs. Due to the difference of the connection mode between carbazole unit and Xanthone, the compounds have different photophysical properties and device performance. The glass transition temperature of these compound is higher than 120°C , which indicates that these compounds have good thermal stability. As a single host green phosphorescent device, **p-XanCarDipha** has a maximum current efficiency of $62.55 \text{ cd}\cdot\text{A}^{-1}$ and a maximum power efficiency of $42.60 \text{ lm}\cdot\text{W}^{-1}$. Furthermore, the maximum external quantum efficiency, current efficiency and power efficiency of **p-XanCarDipha:cartria** (double host) are 20.93%, $77.40 \text{ cd}\cdot\text{A}^{-1}$ and $93.15 \text{ lm}\cdot\text{W}^{-1}$, respectively. Compared with the

single host device, the device efficiency of the double host device is significantly improved.

5. In Chapter 5, we synthesized **CPL-1** and **CPL-2** with triazine structure as the basic unit by changing the branched chain structure, and applied them as capping layer materials in top light-emitting diodes. Compared with **CPL-ref**, the device efficiency of **CPL-1** and **CPL-2** is improved by 3.4% and 9.1%, and they have higher luminous brightness and smaller color deviation in the 0~75° viewing angle range because of the higher refractive index(n) and lower extinction coefficient(K).

Key words: Electron blocking layer; cyclo spiro; Dimethyl-dihydrobenzofuran; Xanthone; Phosphorescent host material; Capping layer material; Top light-emitting diodes

Chapter 1 Introduction

- I . Introduction
- II. Development of OLED display technology
- III. Development and application of hole conduction characteristic groups
 - III-1. Application of hole conduction characteristic groups in OPCs
 - III-2. Application of hole conduction characteristic groups in OFETs
 - III-3. Application of hole conduction characteristic groups in PSCs
 - III-4. Application of hole conduction characteristic groups in OLEDs
- IV. Research on new OLED materials based on the application of hole conducting groups
 - IV-1. TDATA series with triphenylamine (TPA) as the core
 - IV-2. TDAB series with benzene as the core
 - IV-3. TPB series with N,N,N',N'-Tetraphenylbenzidine (TPB)
 - IV-4. N,N,N',N'-Tetraarylaryl diamines series
 - IV-5. The series with Carbazole as the core
 - IV-6. The series with Spiral ring
 - IV-7. Other types of hole transport materials
- V . The main research contents of this paper

I . Introduction

One night in 1979, Dr. C. W. Tang, a Chinese scientist who was engaged in scientific research at Kodak company, suddenly remembered something forgotten in the laboratory on his way home. Back in the lab, he found something bright in the dark. Turn on the light, it turns out that an organic battery is emitting light. What's going on? This is the beginning of the study of organic light-emitting diodes (OLED), and Dr. C. W. Tang is also known as the father of OLED. This is the origin of OLED technology, which was later known as "the next generation of flat panel display after LCD". In recent years, OLED has received great attention from the industry. OLED from its birth to the present, after decades of years, is now starting to enter the stage of industrialization at an alarming speed, occupying a place in the competitive flat panel display market.

OLED refers to the technology that organic semiconductor materials and organic light-emitting materials lead to luminescence through carrier injection and recombination driven by electric field. The principle is to use ITO glass transparent electrode and metal electrode as anode and cathode respectively, and driven by a certain voltage, electrons and holes are injected from the cathode and anode to the electron transport layer and hole transport layer respectively, and then migrate to the luminescent layer respectively. After recombination of electrons and holes, excitons are formed to excite the luminescent molecules, and the latter emit visible light after radiation. The radiation can be observed from the ITO side, and the metal electrode film also acts as a reflecting layer.

Organic synthesis can synthesize a large number of organic luminescent materials by molecular design. The luminescent materials can be small molecular organic compounds or polymer materials. The former is suitable for sublimation and deposition, the latter is suitable for spin coating. The multilayer organic thin film electroluminescent display technology, with its outstanding technical performance, is threatening and challenging almost all the flat panel display products with the mainstream of liquid crystal display. It is expected that OLED will be widely used in national defense, family, and various digital instruments and equipments. As one of the scientific and technological

standards of a country in the information age, OLED will play an important role in the national economy and national defense industry.

OLEDs are not only a highlight of the new generation of flat panel display technology, but also one of the world's preferred green light sources. It is believed that this new flat panel display technology will make a revolutionary leap in the display area in the near future.

II. Development of OLED display technology

Electroluminescence (EL) refers to the luminescent phenomenon that luminescent materials are excited by electric current and electric field. It is a kind of luminous process that converts electric energy into light energy directly. Organic electroluminescence refers to the electroluminescence phenomenon of organic materials excited by electric current or electric field. The device made according to this principle is called organic electroluminescent device. The early research work of organic electroluminescence mainly focused on the following two aspects: organic molecular crystal electroluminescence and organic thin film electroluminescence. As early as the 1950s, organic materials have been explored to make electroluminescent devices. At that time, the materials used were limited to some organic crystal materials that may be due to the structure of inorganic semiconductor luminescence. At first, A. Bernanose et. al.⁽¹⁾ observed the luminescence phenomenon by applying DC voltage on both sides of anthracene single crystal, which opened the prelude of obtaining electroluminescence from organic compounds. In 1963, the blue electroluminescence of anthracene single crystal was also obtained by M. Pope et. al.⁽²⁾ However, due to the thickness of the single-crystal light-emitting layer reaches 20 μm and the driving voltage is as high as 400V, it has not attracted extensive research interest. Subsequently, W. Helfrich et al.^(3,4) made further study on the electroluminescence of anthracene single crystal. In 1969, J. Dresner et al.⁽⁵⁾ introduced solid electrodes into organic light-emitting devices. Early studies have established the understanding of the whole process of organic electroluminescence (OLED). ①electron and hole are injected from cathode and anode respectively; ②carrier recombination; ③exciton generated by recombination completes energy attenuation through

radiation. In 1973, the single crystal was replaced by anthracene thin film deposited in vacuum. ⁽⁶⁾

In 1982, P.S. Vincett ⁽⁷⁾ group began to use various thin films (such as Langmuir Blodgett thin film and vacuum deposition film) to replace the crystal, using aluminum and gold as cathode and anode, which reduced the working voltage and improved the brightness of light. The thickness of anthracene deposition film is 0.6 μm in vacuum, and the operating voltage of the device is controlled within 30 V. But at that time, the device life was still very short, and the luminescent efficiency was very low. These shortcomings have not attracted much attention. Until 1987, Kodak's C.W. Tang and S.A.VanSlyke⁽⁸⁾ used aromatic diamine as hole transport layer and 8-hydroxyquinoline aluminum as luminescent layer (as shown in Fig.1) to prepare thin film OLED with driving voltage less than 10 V, high luminous efficiency(1.5 $\text{lm}\cdot\text{W}^{-1}$) and high brightness(over 1000 $\text{cd}\cdot\text{m}^{-2}$). The research work of organic light-emitting devices has achieved epoch-making development. Its main contribution can be summarized as follows: (1) A double layer device structure was proposed; (2) Excellent luminescent material Alq₃ was fabricated and hole transport layer was introduced for the first time; (3)the use of ultra thin film technology; (4) The Mg/Ag alloy with low and stable work function was used as cathode.

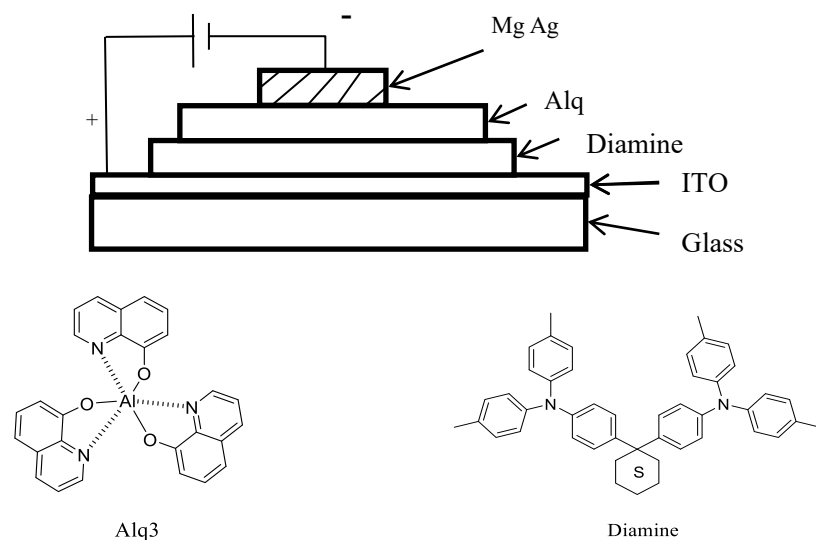


Fig.1 Configuration of EL cell and molecular structures

This breakthrough research work not only shows the outstanding advantages and great application prospects of organic thin film electroluminescence, but also reveals the key points of the OLED design—the balanced injection and effective recombination of positive and negative

carriers. It points out the direction of OLED material and device efforts. It is known as the milestone of organic electroluminescence.

Subsequently, Salto and Tsutsui et. al.^(9,10) from Kyushu University of Japan proposed the device model of multilayer structure. The performance of the device is further improved by sandwiching the light-emitting layer between the electron transport layer and the hole transport layer. The typical device structure is ITO/hole transport layer (TPD)/light emitting layer/electron transport layer(NPB)/Mg:Ag. A blue light emitting device with a luminance of 700 cm^{-2} was obtained at a voltage of 10V and a current density of $100 \text{ mA}\cdot\text{cm}^{-2}$. In multilayer devices, different luminescent colors can be obtained by using different luminescent materials. At the same time, the selection range of organic materials and electrode materials is greatly widened, which lays the foundation for the research of organic thin film electroluminescent devices.

In the following ten years, breakthroughs have been made in the color, brightness, efficiency and lifetime of OLED by continuously improving the properties of electrode materials, light-emitting materials and transport layer materials, as well as device manufacturing technology, sealing conditions and so on. Its single index has basically met the practical requirements, the maximum luminous brightness has exceeded $10^6 \text{ cd}\cdot\text{m}^{-2}$, the luminous efficiency has reached $15 \text{ lm}\cdot\text{W}^{-1}$, the quantum efficiency is 8%, the working life is 10000h, and the red, blue, green and white luminescence are realized.⁽¹¹⁾ Japan pioneer company has launched a 64×256 pixel green flat panel display at the end of 1998.

In 1990, Burroughes et al.⁽¹²⁾ Of Cavendish Laboratory, Cambridge University reported the electroluminescence of PPV (p-phenylene-vinylene) for the first time in the journal Nature. In 1991, D. Braun and A.J. Heeger⁽¹³⁾ of the University of California, Santa Barbara, spin coated the MEH-PPV derivative of PPV into a film on ITO to produce orange OLED with quantum efficiency of 1%. Since then, the research of organic polymer electroluminescence was opened. Organic polymer luminescent materials have attracted much attention due to their easy modification, easy cutting, easy film-forming, soft screen display and good thermal stability. The emergence and development of polymer light-emitting devices indicate that the research of organic thin film devices has entered a new stage.

At present, European and American countries mainly focus on Electroluminescence of polymer materials, while Japan focuses on Electroluminescence of small organic materials. Through hard work, OLED products are constantly emerging.

In the field of small molecule electroluminescence, the Northeast pioneer (located in mi'ze) assisted by Japan's Pioneer company invested US \$280 million to establish a multi-color OLED display production line with a monthly output of 30000 pieces of 64×256 pixels. Pioneer company also launched a 5.2-inch passive matrix display with pixel spacing of 0.11 mm. This panchromatic display is made by moving the mask in turn and depositing red, green and blue emitting materials respectively. The first OLED full-color display driven by low-temperature polysilicon thin-film transistor was successfully manufactured by using Kodak's film forming technology and Sanyo's TFT low-temperature polysilicon technology in September 1999. The size of the display is 2.4 inches, the pixel size is 0.057×0.165 mm², and the driving voltage is 12 V, which is only the thickness of a coin.

In terms of polymer electroluminescence, the first LEP (Light Emitting Polymer) company is Holland Philips company. They produce 1000000 mm² devices every year, initially planning to produce back lighting, and later produced a pixel 87×80 and a gray level display of 256. Holland Philips company and Uniax company of California, USA, under the leadership of Nobel Prize winner Heeger (the patent is the University of California), 4000 passive dot matrix displays with size of 2 inches and 64×96 pixels were produced each month in December 1994. They also launched the pixel 160×160 flat panel personal digital palm computer monitor. Hoechst company in Germany has carried out LEP technology development and research very early. GmbH of Frankfun company of Germany was founded in 1999. It mainly provides soluble derivatives of PPV with various luminescent colors for the organic EL industry. Holland Philips company and Covion company have CDT (Color Display Tube) patent license, and also provide patent technology to DuPont, Hewlent-Packard, and Seiko-Epson company. It is reported that Seiko-Epson company has produced full-color dot matrix addressing display using inkjet printing technology. Small molecules and polymers have made great progress in displaying applications, but their applications are different

because of their different characteristics. For example, small organic molecules may have more characteristics in high resolution applications, and polymers may have broad prospects in large area flexible displays. Cambridge University of England and Epson company of Japan cooperated to develop a color polymer display screen driven by low temperature polysilicon thin film transistor. In addition, Philips company, Uniax company and German Covin company have also developed organic EL displays with high efficiency, high brightness and long life.

In 1994, the Kido research group of Yamagata University of Japan made white light OLEDs for the first time, ⁽¹⁴⁾which opened the door of white light OLED research and made it possible for organic light-emitting devices to be used for lighting.

In 1998, the research group of Förrest of Princeton University in the United States doped the high efficiency luminescent organic phosphorescent material into the main material to make the singlet and triplet excitons luminescence at the same time, and achieved the high efficiency phosphorescence OLED.^(15,16) It breaks through the limit of 25% of the maximum internal quantum efficiency of organic electroluminescence and achieves 100% internal quantum efficiency. This work creates a new field of organic electroluminescence phosphorescent OLED, which greatly promotes the development of organic electroluminescence. In the same year, Hebner, et al in the another research group of Princeton University used ink-jet printing technology to prepare organic light-emitting devices,^(17,18) which gradually made organic light-emitting devices from the laboratory to the market, and greatly promoted the development of OLED.

In 2004, Liao et al. of Kodak company and Kido group of Yamagata University of Japan used tandem device structure to fabricate OLED. The device efficiency reached $136.3 \text{ cd} \cdot \text{A}^{-1}$,^(19,20) and the lifetime of the device was extended.

In recent years, due to the huge advantages and broad commercial prospects of organic light-emitting display technology, it has become a very popular emerging display product in the world (as shown in Fig.2), and is known as the "ultimate display".

In terms of information display, OLEDs have many advantages over the

current popular liquid crystal display (LCD), such as: (1) Thickness can be less than 1 mm, only 1/3 of the LCD screen, and lighter weight; (2) There is almost no visual angle problem, even if viewed from a large angle of view, the picture is still not distorted; (3) Solid structure, no liquid material, so anti-seismic performance is better; (4) Low temperature characteristic is good, it can display normally at -40°C ; (5) The response time is one thousandth of that of LCD, and there is absolutely no dragging phenomenon when displaying fast moving images; (6) The manufacturing process is simple and the cost is lower; (7) It has higher luminous efficiency and lower energy consumption than LCD; (8) It can make a very small single pixel, especially suitable for use in micro display devices; (9) It can be manufactured on different substrates and can be made into flexible displays.

In terms of solid-state lighting, OLED lighting has the advantages of soft light color, high energy efficiency, light, soft, fast response speed, wide temperature range and strong anti-seismic ability. Moreover, OLED is surface emitting, so there is no need to add lampshade, heat dissipation and other devices, it has unique advantages in the field of lighting. Compared with LED, OLED lighting also has certain advantages, mainly reflected in the following aspects: (1) The OLED light source is a flat light source, which can emit any color, and the depth and intensity of the tone. The color rendering index is close to 100, which can simulate the daylight color; (2) Because of its light, soft and transparent characteristics, OLED lighting can be used as a whole piece of surface light when it is turned on; it can be used as a transparent window when it is closed, so OLED has obvious advantages in the field of indoor lighting; It is generally believed that if the luminous efficiency of OLED exceeds $100 \text{ lm}\cdot\text{W}^{-1}$, it is expected to replace the general lighting products. Due to the unique advantages of OLED lighting, major lighting manufacturers in Europe and the United States have successively invested in the field of OLED lighting.

As a result of joint efforts of the global technology community, OLED has developed very rapidly. With the improvement of luminous efficiency and brightness, and the decrease of turn-on voltage, the stability of spectrum and the lifetime of OLED have been greatly improved. However, there are still higher requirements for efficiency and lifetime in terms of commercial applications in display and lighting.

III. Development and application of hole conduction characteristic groups

There are many kinds of organic semiconductor materials, which can be divided into carrier injection materials, carrier transport materials and luminescent materials according to their different uses. Carrier transport materials can be divided into hole transport materials (HTMs) and electron transport materials (ETMs). In recent years, the research of electron transport materials has entered the bottleneck, and it is difficult to make breakthrough progress. Because of its changeable structure, the good performance of hole transport materials has become a research hotspot.

III-1. Application of hole conduction characteristic groups in OPCs

OPCS (Organic Photoconductors) are the core components of xerography, laser printing, holography and light printing plate making, which directly determines the quality of printed matter. With the increasing automation of office equipment, the development of organic information electronic material technology and human's attention to the environment, the selenium drum made of traditional inorganic photosensitive materials such as selenium and cadmium sulfide is gradually replaced by organic photoconductor. Due to the advantages of organic photoconductive materials, such as sensitivity, high efficiency, stability and reliability, low price and low non-toxic pollution, organic photocopiers and almost 100% of laser printers, which account for 98% of the total global output, use organic photoconductors.⁽²¹⁾ The commercialized organic photoconductors usually adopt the multi-layer device structure with function separation. The typical structure is shown in Fig.2.

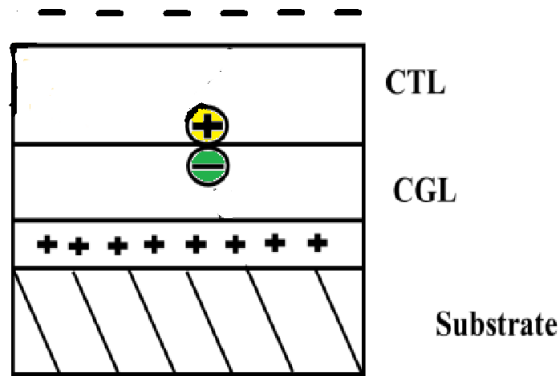


Fig.2 The structure of Organic photo conductor

The working principle of xerography is that with the help of high voltage charge sensor (corona discharge), the surface of charge transfer layer (CTL) is charged with uniform negative charge, and then the light containing image information irradiates the charge generation layer (CGL) to generate carrier pairs (electron hole pairs), and the holes pass through the CTL and recombined with surface charges, and the electron is transferred to the conductive substrate to form the electrostatic latent image of the image. Through the development and negative voltage transfer device, the developing powder is transferred to the paper to form an image, and then hot pressed and fixed to obtain a clear image.⁽²²⁾

In the double-layer structure, charge generation and charge transfer are completed in two layers respectively. The main task of charge generation layer (CGL) is to generate charge, while charge transfer layer (CTL) is responsible for transferring charge. CGL absorbs a large amount of irradiated light, and its thickness is about 0.1~2 μm CTL not only needs to transfer charge, but also acts as the protective layer of CGL to improve the mechanical strength of photoconductive devices, and its thickness is 15~20 μm .⁽²³⁾

The organic photoconductive materials used in high performance electrostatic copier need to meet the following requirements: high sensitivity, low dark attenuation, low residual potential, spectral response in the range of 450~650 nm. Because the carrier transport material is in the surface layer, it is

in direct contact with the paper when used, and it has to undergo frequent charge and discharge. Therefore, the performance of carrier transport material directly determines the service life of OPC. Triphenylamine compounds are commonly used in OPC devices because of their high hole mobility, good matching with charge generating materials, good compatibility with resin, no substantial absorption of visible light, strong charge discharge tolerance and simple purification method. They are commonly used in OPC devices and have good photosensitivity. The Fig.3 shows the structure of typical hole transport materials used in OPC by major companies in the world.

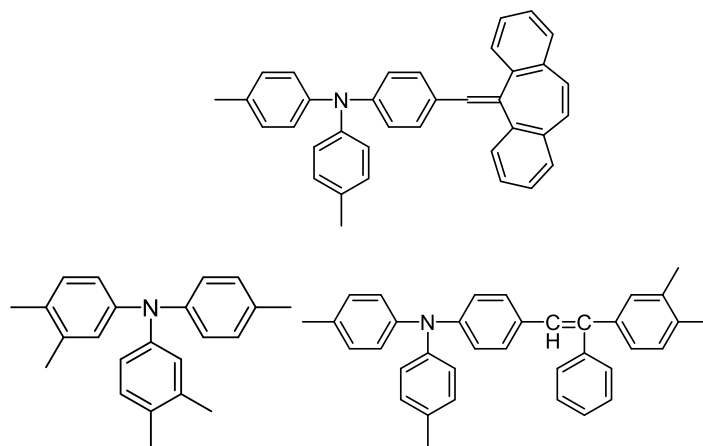


Fig.3 The structure of HTMs in OPCs

Li et al.^(24, 25) prepared a series of styrene triphenylamine compounds with the general structure formula as shown in Fig.4 Organic photoconductors were prepared by using Y-TiOPc as charge generating material and synthesized compounds as hole transporting material. The photoelectric properties were tested, the photosensitivity was 0.04~0.05 lx·s, indicating that triphenylamine compounds are excellent charge transfer materials.

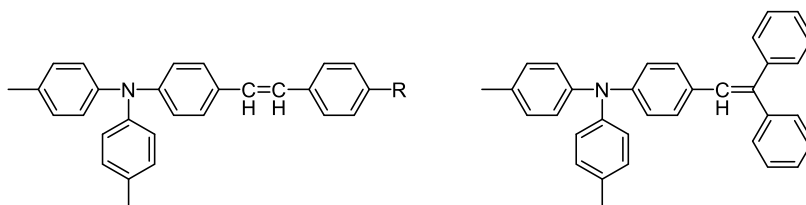


Fig.4 The structure of HTMs in OPCs

III-2. Application of hole conduction characteristic groups in OFETs

OFETs (Organic Field Effect Transistors) is a three terminal device which uses organic conjugated molecules as active semiconductor layer, inorganic or polymer dielectric materials as insulating gate, and regulates on-off state by gate voltage. It can be used in large area, low-cost, flexible integrated circuits, liquid crystal display, organic light-emitting and electronic ink drive circuits, smart cards and sensors.^(26, 27)

The working principle of organic field effect transistor⁽²⁸⁾ is to form charge accumulation layer at the interface between semiconductor and insulating layer by applying insulating gate voltage, and realize the on and off state of device by regulating the carrier density between source and drain electrode by gate voltage. The important parameters of the performance of OFET are mobility, switching current ratio and threshold voltage. The switching ratio is determined by the mobility. Only high mobility can ensure a large switching ratio and be applied to integrated circuits. Therefore, the mobility of organic charge transfer materials is the key factor to determine the performance of OFET devices.⁽²⁹⁾

Sonntag et al.⁽³⁰⁾ synthesized a series of star shaped hole transport materials centered on triphenylamine (TPA). The structures are shown in Fig.5. The hole mobility is $3 \times 10^{-4} \text{ cm}^2 \text{V}^{-1} \text{s}^{-1}$. It has been successfully applied to OFET devices by spin coating, and the switching current ratio is up to 10^5 .

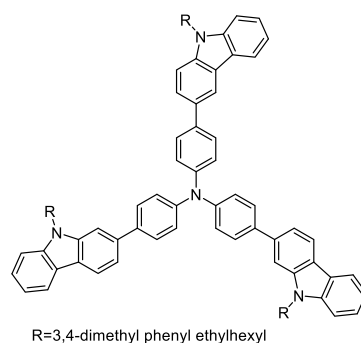


Fig.5 The structure of HTMs in OFETs

III-3. Application of hole conduction characteristic groups in PSCs

PSCs (Perovskite Solar Cells) are new energy cells that convert solar energy into electric energy by organic semiconductor materials. This new type of solar cell is different from the traditional solar cell, mainly including the unique micro cell structure and the preparation of large surface area to control the photovoltaic performance.⁽³¹⁾ Perovskite solar cells, with simple structure and low cost, have become the focus of current research. The working principle of perovskite solar cell is similar to that of organic solar cell. It uses organic metal halide semiconductor with perovskite structure as light absorbing material, which is equivalent to donor (PCBM) and acceptor (P3HT) in organic solar cell. As shown in Fig.6, its working principle is mainly divided into three steps: 1) The perovskite layer absorbs photons to generate carriers (electron-hole pairs); 2) The carriers transmit to the electron transport layer and the hole transport layer respectively; 3) The electrons and holes are collected at the electrode interface.⁽³²⁾ Perovskite type solar cells mainly include the following parts ⁽³³⁾: transparent conductive glass (FTO), electron transport layer, perovskite layer, hole transport layer and counter electrode, as shown in Fig.6.

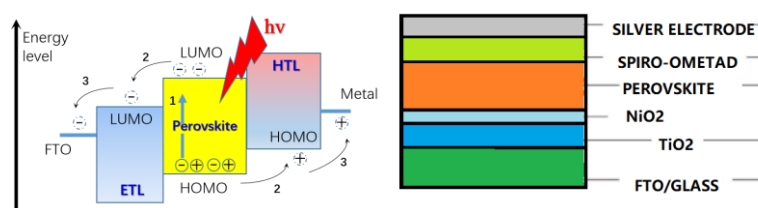


Fig.6 The working principle and structure of perovskite solar cells

Spiro-OMeTAD is the most effective hole transport material in perovskite solar cells. The structure is shown in Fig.7. Kim et al.⁽³⁴⁾ prepared FTO/dense TiO₂/mesoporous TiO₂/CH₃NH₃PbI₃/HTM/Au structure perovskite solar cells by

spin-coating Spiro-OMeTAD as a solid electrolyte for the first time. Under the condition that the solar cell is not encapsulated, the stability of the cell is improved by using the solid electrolyte compared with the liquid electrolyte, and the efficiency reaches 9.7%. Moreover, a rapid reduction quenching occurs in the excited state of the perovskite layer after using the hole transport material (Spiro-OMeTAD). Both millisecond laser spectra and photoinduced absorption spectra show that the separation of excitons involves the transport of holes and electrons, that is, the diffusion of holes into the hole transport material (Spiro-OMeTAD) layer through the excited state $\text{CH}_3\text{NH}_3\text{PbI}_3$, and the electron transport to the electron transport material (TiO_2) layer.

Grimsdale et al.⁽³⁵⁾ achieved an efficiency of 13.8% using H101 as a hole transport material. Compared with the harsh Grignard reaction conditions of Spiro-OMeTAD, the synthesis method of the compound is simple, which provides the possibility for the industrialization of perovskite solar cells.

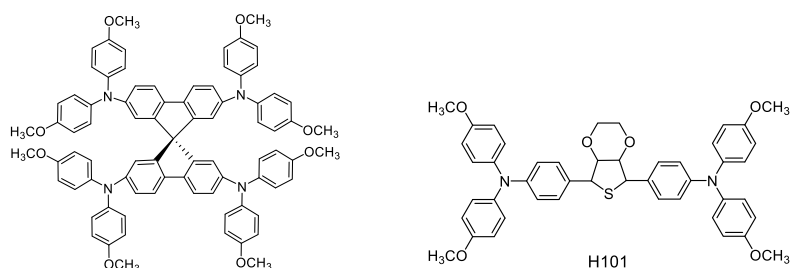


Fig.7 The HTMs of perovskite solar cells

III-4. Application of hole conduction characteristic groups in OLEDs

In OLED, the role of the hole transport layer is to improve the efficiency of hole transport in the device, and block the electrons in the light-emitting layer to achieve the maximum recombination of carriers. The hole transport layer can reduce the energy barrier in the process of hole injection, increase the efficiency of hole injection, and improve the brightness and lifetime of devices.

Wu IY et al. ⁽³⁶⁾ synthesized a series of triphenylamine hole transport materials with hexathiophenylbenzene as the core. These compounds have

high glass transition temperature (T_g) (80~111°C) and are oxidized to polycation at 150 mV. The double-layer EL device ITO/HTM (40 nm)/Alq₃ (46 nm)/Mg:Ag, the turn-on voltage at 6~8 V, external quantum efficiency of 1.2~1.6%, and maximum brightness of 14000~20000 cd·cm⁻².

Wu CC et al. ⁽³⁷⁾ used TCTA as the hole transport material and TADF as the blue light-emitting material. The OLED structure was ITO/PEDOT:PSS/TCTA (40 nm)/ TADF (30 nm)/TPBI (30 nm)/LiF/Al, the turn-on voltage is only 2.5 V, the external quantum efficiency is 5.3%, which is equivalent to the blue OLED reported in the past, but the CIE coordinates are (0.158, 0.041). These values exceed the standard of blue light in NTSC and are ultra pure blue light.

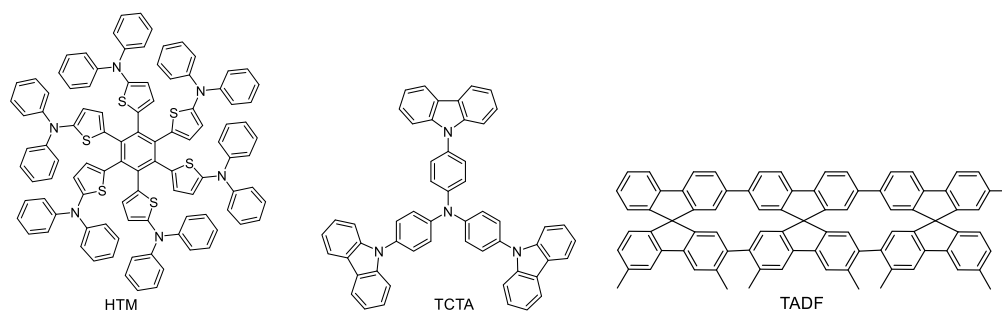


Fig.8 The structure of materials in OLEDs

In the next chapter, the corresponding hole conducting groups for new OLED materials will be introduced.

IV. Research on new OLED materials based on the application of hole conducting groups

As functional layer materials in OLED devices, hole transport materials should not only have high hole mobility, but also meet the following conditions: (1) they can form uniform amorphous film without defects; (2) they have good thermal stability and can still maintain the amorphous shape under long-term operation. Although the aging mechanism of OLED is not very clear, some studies have shown that the change of physical morphology of organic layer is

one of the influencing factors ⁽³⁸⁾, such as melting and crystallization of organic layer caused by heat generated during device operation; (3) It has a suitable highest molecular occupied orbital (HOMO) energy level to ensure the effective injection and transmission of holes between the interfaces, and prevent the material recrystallization caused by excessive Joule heat in the device operation. This kind of crystallization will destroy the uniformity of the film, and destroy the good interface contact between the hole transport layer and the anode and organic layer, resulting in the decrease of device life.⁽³⁹⁾ Therefore, materials with high T_g are usually used to improve the lifetime of devices.

According to the molecular weight, hole transport materials can be divided into “small molecule” (molecular weight <2000) and polymer (molecular weight >10000). Among them, small molecule hole transport materials have attracted much attention due to their advantages such as easy synthesis, convenient purification and excellent performance. According to the different structures of small molecular compounds, small molecule hole transport materials are divided into the following categories:

IV-1. TDATA series with triphenylamine (TPA) as the core

These compounds are a class of hole transport materials, including TDATA, 2-TNADA, TFATA and so on. In general, these compounds have the advantages of high T_g , low ionization energy (~ 5.1 eV) ⁽⁴⁰⁾, high quality amorphous films and good transparency in the visible region. These compounds can also be used as hole injection materials in OLED ⁽⁴¹⁾, they are the most widely used small molecules hole injection material. In addition, based on the structural adjustment, the compounds TCTA, TPTTA, TPOTA, FATPA-T and FATPA-Cz was synthesized. Due to the introduction of rigid groups, the glass transition temperature of these compounds has been significantly

increased, and the T_g of FATPA-Cz has reached 272°C , It is the highest T_g among the known small molecule HTMs.⁽⁴²⁾ Compounds with similar structure include TPTE series compounds (TPTE(1), TPTE(2)), which can also be used as hole injection materials.⁽⁴³⁾ Because of the large HOMO-LUMO orbital energy level difference (E_g), TCTA can be used not only as hole transport material, but also as host for green phosphorescence doping.⁽³⁷⁾

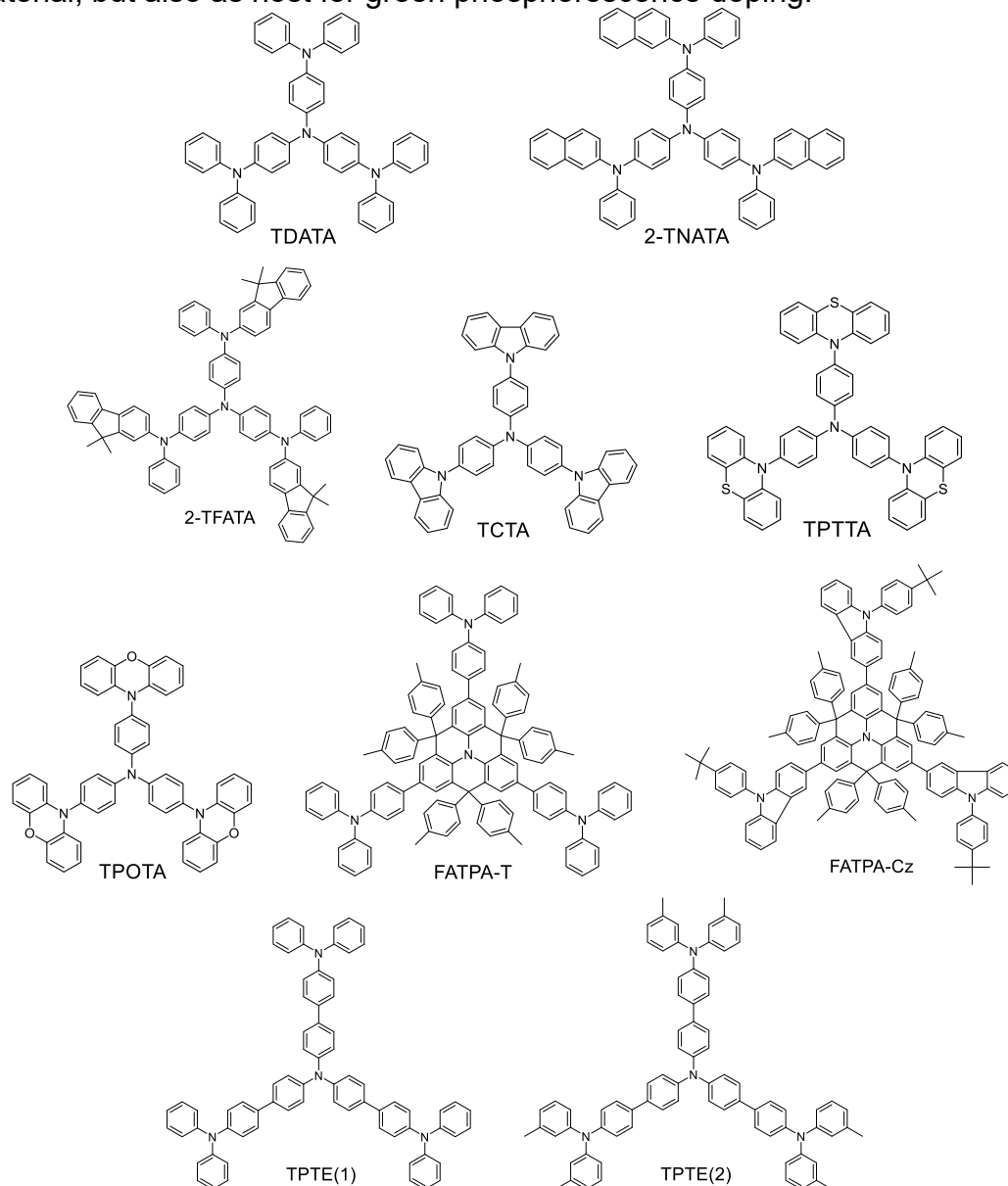


Fig.9 The structures of TDATA series materials

IV-2. TDAB series with benzene as the core

TDAB series amorphous molecular materials include TCB, *p*-DPA-TDAB, TECEB, EPEB, etc. Among them, the carbazole group 3 and 6 of TCB molecule can be further expanded to obtain (BTTC, BTDTC) and TCB is the main material of blue phosphorescent OLEDs.⁽⁴⁴⁾

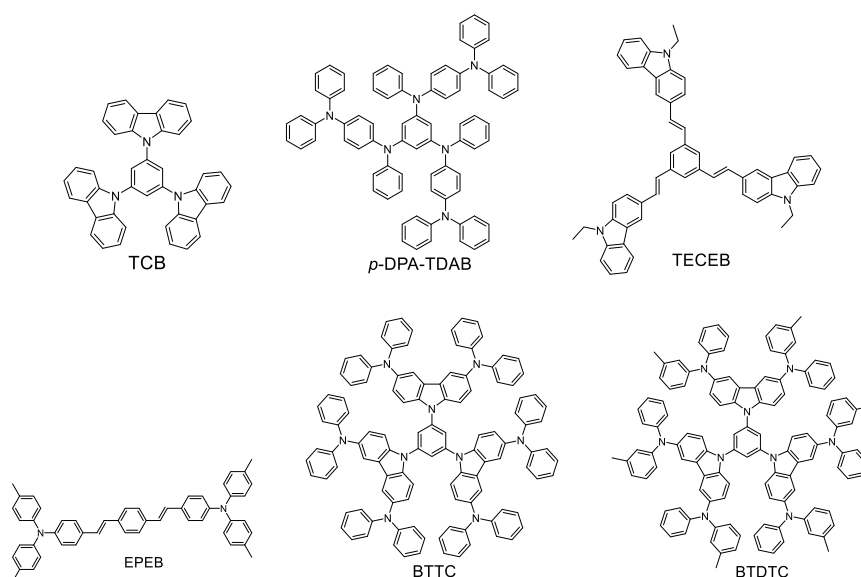


Fig.10 The structures of TDAB series materials

IV-3. TPB series with N,N,N',N'-Tetraphenylbenzidine (TPB)

As a hole transport material, TPB has been widely used in organic photoconductive drum,⁽⁴⁵⁾ and also widely used in green OLED with 8-Hydroxyquinoline aluminum (Alq₃).⁽⁴⁶⁾ TPB molecules have poor thermal and morphological stability and are easy to crystallize.⁽⁴⁷⁾ Therefore, the stability of TPB can be improved by structural modification on the benzene ring of triphenylamine to increase the molecular molar mass and steric hindrance. A series of compounds substituted by naphthalene, diphenyl, phenanthrene, fluorene and carbazole have been studied. The representative compounds are TPD, α -NPD, CBP, FFD, BTB, etc. In addition to the modification of the terminal triphenylamine benzene ring, the core diphenyl group can also be further modified, such as NPF, two-dimensional TPB compounds: TPTE, BPBA

etc. CBP as the host has been widely used in phosphorescent OLEDs. TPD and α -NPD can be used in blue fluorescent OLEDs with high quantum yield. (48, 49)

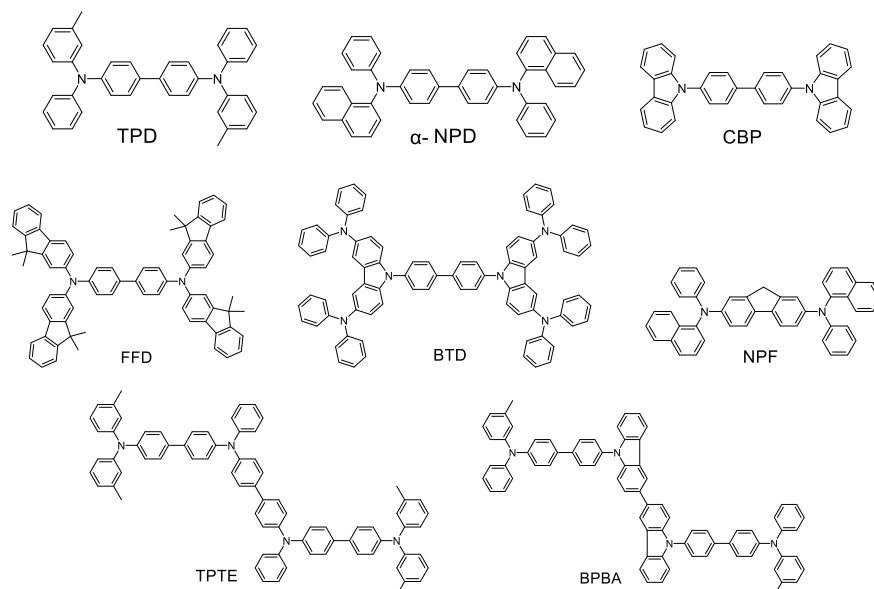


Fig.11 The structures of TPB series materials

IV-4. N,N,N',N'-Tetraarylaryl diamines series

These compounds are synthesized by functional assembly of aromatic rings (benzene ring, naphthalene ring, anthracene ring, etc.), such as $DN_{\alpha}P$ and $TN_{\beta}P$, $N_{\alpha}N_{\alpha}P$ and $N_{\beta}N_{\alpha}P$, PPA TPA; α -NPA and β -NPA, etc. α -NPA was synthesized from 9,10-dibromoanthrene and N-phenyl-1-naphthylamine in xylene by palladium catalysis. The HOMO and LUMO orbital energy levels of 9,10-bis (diarylamine) anthracene are between -5.5~-5.6 eV and -3.1~-3.3 eV, respectively. The diarylamine group can be substituted by carbazole group to give series compounds of 1-(N-carbazole)-4-diarylaminophenes (DCP and TCP; $N_{\alpha}CP$ and $N_{\beta}CP$ and PDCA, PTCA, PDTCA etc.). These compounds have relatively low ionization energy (50) and can be used as hole injection materials.

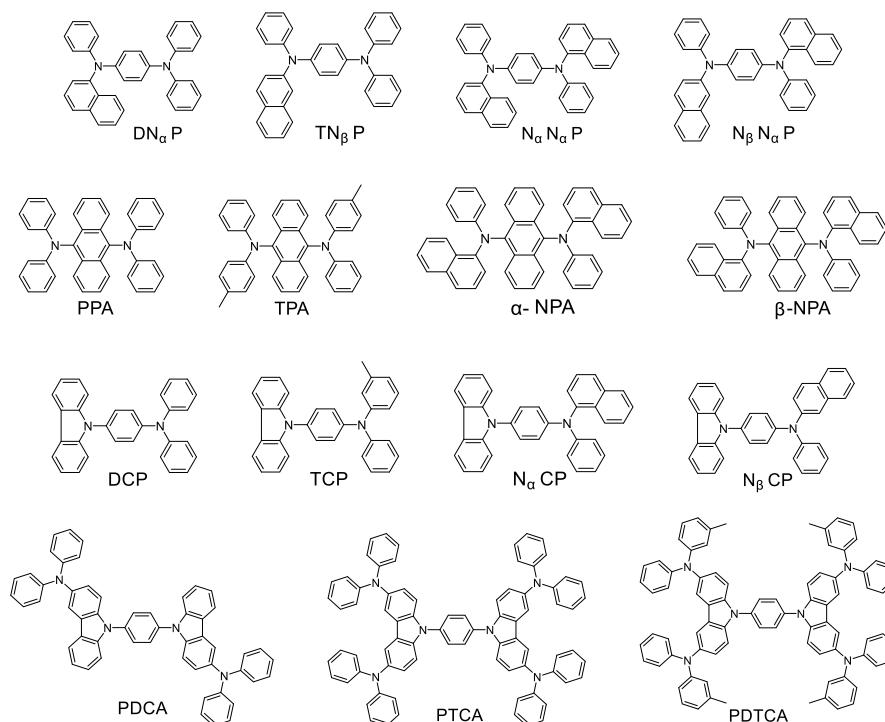


Fig.12 The structures of Tetraaryl diamines series materials

IV-5. The series with Carbazole as the core

This series of compounds are a series of amorphous molecules, which are similar to the core TPA of TADTA, which are replaced by rigid carbazole, and then modified at positions 3, 6 and 9 of carbazole, such as CEBT and PCD, PPCD. The modification of carbazole groups at positions 3 and 6 leads to the formation of amorphous forms, and the increase of conjugated area significantly reduces the ionization energy.⁽⁵¹⁾ The introduction of rigid carbazole ring results in the high T_g of compounds, such as DTPD and DPTPD, which is about 180°C.

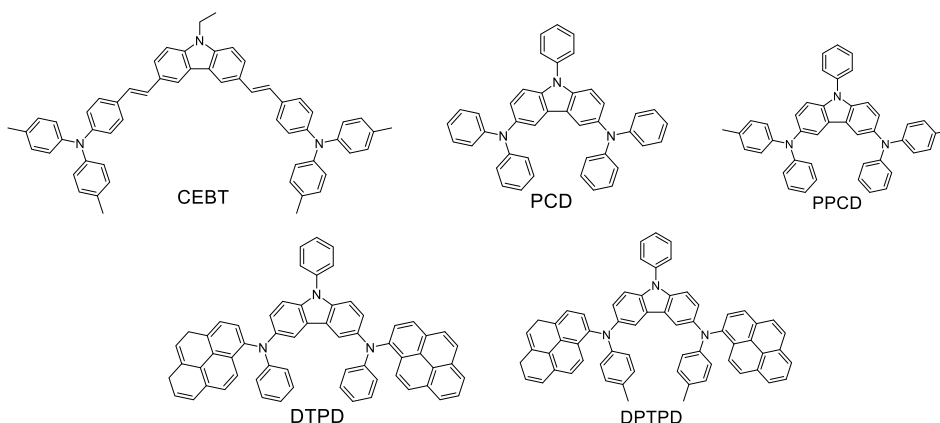
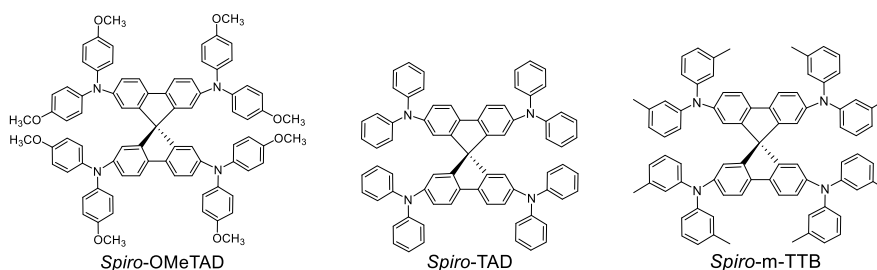


Fig.13 The structures of Carbazole series materials

IV-6. The series with Spiral ring

These compounds are usually obtained by linking spirofluorene with triphenylamine groups. Spirofluorene causes the distortion of the whole molecule and the steric hindrance between molecules, which makes it easy to form amorphous films, a kind of material which is widely used now. For example: *Spiro-OMeTAD*, *Spiro-TAD* and *Spiro-m-TTB*, *Spiro-CARB*, TX-F6S, etc. *Spiro-OMeTAD* is widely used in perovskite solar cells (PSC), its good film-forming performance and appropriate orbital energy level can effectively improve the efficiency and life of the solar cells. It has become a standard whether other small molecule hole transport materials are suitable for PSC.⁽⁵²⁾ However, the complex synthesis and purification process and high price (about 10 times of gold) greatly limit its application.



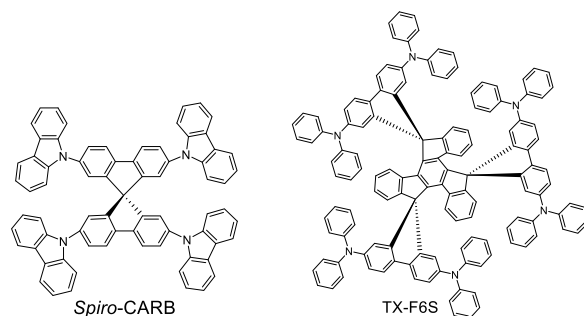


Fig.14 The structures of Spiral series materials

IV-7. Other types of hole transport materials

Some materials do not contain triarylamines or carbazole groups, but can still transport holes, such as bDB, PF6(52), BPFB, HPCzI(54), and organosilicon compounds BD3, etc.

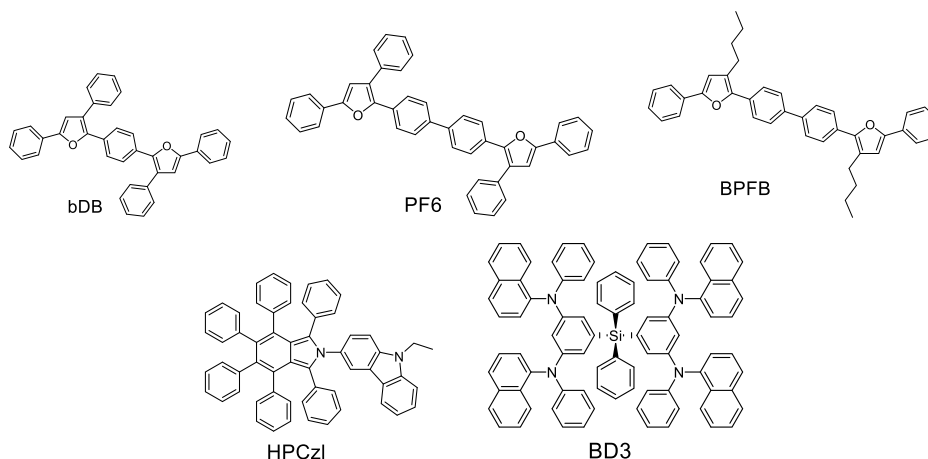


Fig.15 The structures of other type series materials

V. The main research contents of this paper

Based on the above-mentioned problems and shortcomings of organic electroluminescent devices, we have done some work on the performance optimization of fluorescent devices and the development and application of new materials. The details are as follows:

Chapter 2: The design, synthesis and application of hole conducting materials with spiro group characteristics. We synthesized two compounds, BFS2A

(N-([1,1'-biphenyl]-2-yl)-N-(9,9-dimethyl-9H-fluoren-2-yl)spiro[dibenzo[a,d][7]a

nnulene-5,9'-fluoren]-2'-amine) and BFS3A (N-([1,1'-biphenyl]-2-yl)-N-(9,9-dimethyl-9H-fluoren-2-yl)spiro[dibenzo[a,d][7]annulene-5,9'-fluoren]-3-amine) based on a spiro backbone with dimethylfluorene side-chain groups to impart hole-transporting properties and electrochemical stability to electron-blocking materials in the hole-transporting region of OLEDs. Both materials exhibited high electrochemical and thermal stability.

Chapter 3: The design, synthesis and application of new EB materials in OLED devices. The molecular structures of the EBL materials were based on dimethyl-dihydroacridobenzofuran. 7-(5-(dibenzo[b,d]furan-4-yl)-[1,1'-biphenyl]-3-yl)-12,12-dimethyl-7,12-dihydrobenzofuro[3,2-b]acridine (**DFBDDbA**), 7-(3,5-bis(dibenzo[b,d]furan-4-yl)phenyl)-12,12-dimethyl-7,12-dihydrobenzofuro[3,2-b]acridine (**BDFPDDbA**) and 13-(3,5-bis(dibenzo[b,d]furan-4-yl)phenyl)-5,5-dimethyl-5,13-dihydrobenzofuro[3,2-c]acridine (**BDFPDDcA**) were synthesized. The performances of the devices were measured.

Chapter 4: The design and synthesis of D-A phosphorescent host material and its application in OLED devices. we design and synthesize three new xanthone derivatives as host materials, 3-(4-(diphenylamino)-9H-carbazol-9-yl)-9H-xanthen-9-one (**XanCarDipha**), 2-(4-(4-(diphenylamino)-9H-carbazol-9-yl)phenyl)-9H-xanthen-9-one (**p-XanCarDipha**), and 2-(3-(4-(diphenylamino)-9H-carbazol-9-yl)phenyl)-9H-xanthen-9-one (**m-XanCarDipha**), fabricate corresponding single- and double-host materials systems for use as the EML in PHOLEDs. Their properties of PHOLEDs were systematically investigated in order to understand the structure-energy level-device performance correlations for developing efficient PHOLED materials.

Chapter 5: The fabrication of high efficiency top emitting OLEDs based on self-developed organic materials with the highest refractive index were

researched. The effects of capping materials with different refractive indices on the performance of TEOLEDs were investigated. Specifically, N4,N4,N4',N4'-tetra([1,1'-biphenyl]-4-yl)-[1,1'-biphenyl]-4,4'-diamine (**CPL-ref**), 2,2'-((6-([1,1'-biphenyl]-4-yl)-1,3,5-triazine-2,4-diyl)bis(4,1-phenylene))bis(1-phenyl-1H-benzo[d]imidazole) (**CPL-1**), and 2,2'-((6-(9-phenyl-9H-carbazol-3-yl)-1,3,5-triazine-2,4-diyl)bis(4,1-phenylene))bis(benzo[d]oxazole) (**CPL-2**) were used as the capping materials.

Chapter 1 References

- (1) A. Bernanose, F. D. Pharmacie, and U. D. Nancy, *Br. J. Appl. Phys.*, 6, S54-S55 (1955).
- (2) M. Pope, H. P. Kallmann, and P. J. Magnante, *J. Chem. Phys.*, 38, 2042-2049 (1963).
- (3) W. Helfrich, and W. G. Schneider, *Phys. Rev. Lett.*, 14, 229-231(1959).
- (4) W. Helfrich, and W. G. Schneider, *J. Chem. Phys.*, 44, 2902-2909 (1966).
- (5) J. Dresner, *RCA Rev.*, 30, 322-334 (1969).
- (6) N. V. Vityuk, and V. V. Mikho, *Phys. Semicond.*, 6, 1479 (1973).
- (7) P. S. Vincett, W. A. Barlow, R. A. Hann, and G. G. Roberts, *Thin Solid Films*, 94, 171-183 (1982).
- (8) C.W. Tang, S. A. VanSlyke, *Appl. Phys. Lett.*, 51, 913-915 (1987).
- (9) C. Adachi, S. Tokito, T. Tsutsui, and S. Saito, *Jan. J. Appl. Phys.*, 27, L269-L271 (1988).
- (10) C. Adachi, T. Tsutsui, S. Saito, *Appl. Phys. Lett.*, 76,779-781 (1990).
- (11) J. R. Sheats, H. Antoniadis, M. Hueschen, W. Leonard, J. Miller, R. Moon, D. Roitman, and A. Stocking, *Science*, 273, 884 (1996).
- (12) J. H. Burroughes, D. D. C. Bardley, A. R. Brown, et al, *Nature*, 65, 3610 (1989).
- (13) D. Braun and A. J. Heeger, *Appl. Phys. Lett.*, 58, 1982 (1991).
- (14) J. Kido, K. Hongawa, K. Okuyama, K. Nagai, *Appl. Phys. Lett.*, 64, 815 (1994).
- (15) M. Baldo; D. O'brien, Y. You, A. Shoustikov, S. Sibley, M. Thompson, and S. R. Rorrest, *Nature*, 395, 151 (1998).
- (16) M. Baldo; S. Lamansky, P. Burrows, M. Thompson, and S. R. Rorrest, *Appl. Phys. Lett.*, 75, 4 (1999).
- (17) T. R. Hebner, C. C. Wu, D. Marcy, H. Erohne, O. Nuyken, H. Becker, and K. Meerholz, *Appl. Phys. Lett.*, 72, 519 (1998).
- (18) T. R. Hebner, and J. C. Sturm, *Appl. Phys. Lett.*, 73, 1775 (1998).
- (19) L. S. Liao, K. P. Klubek, and C. W. Tang, *Appl. Phys. Lett.*, 84, 167 (2004).

- (20) J. Kido, T. Matsumoto, T. Nakada, J. Endo, K. Mori, N. Kawamura, and A. Yokoi, *SID' 03 Dig.*, 27, 964 (2003).
- (21) T. Murayama, *Society for Imaging Science and Technology*, (2001).
- (22) Y. Q. Wang, R. S. Rui, K. J. Jiang, J. W. Zhou, Q. Sui, Q. C. Zhang, D. Y. Ren, Z. W. Di, *High Technology Letters*, 10(7):93-95 (2000).
- (23) D. M. Pai, A. R. Melnyk, *Imaging Science and Photochemistry*, 9(3):198-208 (1991).
- (24) L. Y. Han, X. G. Li, S. R. Wang, and Y. Xiao, *Fine Chemicals*, 30(10):1096-1101 (2013).
- (25) H. X. Zhang, X. G. Li, S. R. Wang, and F. Jiang, *Fine Chemicals*, 24(2):105-107 (2007).
- (26) C. D. Dimitrakopoulos, D. J. Mascaro, *IBM Journal of Research and Development*, 45(1):11-27 (2001).
- (27) Y. Y. Noh, D. T. Kim, and K. Yase, *Journal of applied physics*, 98(7):74505 (2005).
- (28) W. P. Wu, W. Xu, W. P. Hu, Y. Q. Liu, D. B. Zh, *Chemistry*, 69(6):404-409 (2006).
- (29) H. E. Katz, Z. N. Bao, S. L. Gilat, *Accounts of Chemical Research*, 34(5):359-369 (2001).
- (30) M. Sonntag, K. Kreger, D. Hanft, P. Strohrriegl, S. Setayesh and D. M. de Leeuw, *Chemistry of materials*, 17(11):3031-3039 (2005).
- (31) J. Burschka, N. Pellet, S. J. Moon, R. Humphry-Baker, P. Gao, M. K. Nazeeruddin, and M. Grätzel, *Nature*, 499(7458):316-319 (2013).
- (32) D. D. S. Fung, and W. C. H. Choy, London: *Springer London*, pp 1-16, (2013).
- (33) K. W. Tan, H. Sai, and M. Saliba, *Journal of Physical Chemistry C Nanomaterials & Interfaces*, (2014).
- (34) H. S. Kim, C. R. Lee, J. H. Im, K. B. Lee, T. Moehl, A. Marchioro, S. Jin. Moon, R. Humphry-Baker, J. H. Yum, J. E. Moser, M. Grätzel, N. G. Park, *Scientific reports*. 2012, 2:591, (2012) .
- (35) H. Li, K. Fu, A. Hagfeldt, M. Grätzel, S. G. Mhaisalkar, and A. C. Grimsdale, *Angewandte Chemie International Edition*, 53(16):4085-4088 (2014).

- (36) I. Y. Wu, J. T. Lin, Y. Tai. Tao, and E. Balasubramaniam, *Advanced Materials*, 12(9):668-669 (2012).
- (37) C. C. Wu, Y. T. Lin, K. T. Wong, R. T. Chen, and Y. Y. Chien, *Advanced Materials*, 16(1):61-65 (2004).
- (38) S. Tokito, Y. Taga, *Applied Physics Letters*, 66 (6), 673~675 (1995).
- (39) C. Adachi, K. Nagai, and N. Tamoto, *Applied Physics Letters*, 66 (20), 2679~2681 (1995).
- (40) Y. Shirota, Y. Kuwabara, H. Inada, T. Wakimoto, H. Nakada, Y. Yonemoto, S. Kawami, and K. Imai, *Applied Physics Letters*, 65(7):807-809 (1994).
- (41) Y. Shirota, Y. Kuwabara, D. Okuda, R. Okuda, H. Ogawa, H. Inada, T. Wakimoto, H. Nakada, Y. Yonemoto, S. Kawami, K. Imai, *Journal of Luminescence*, 72:985-991 (1997).
- (42) Z.Q. Jiang, T. L. Ye, C. L. Yang, D. Z. Yang, M. R. Zhu, C. Zhong, J. G. Qin, D.G. Ma, *Chemistry of Materials*, 23(3):771-777 (2010).
- (43) M. Y. Chou, M. K. Leung, Y. O. Su, Chang, L. Chiang, C. C. Lin, J. H. Liu, C. K. Kuo, C. Y. Mou, *Chemistry of Materials*, 16(4):654-661 (2004).
- (44) R. J. Holmes, S. R. Forrest, Y. J. Tung, R. C. Kwong, J. J. Brown, S. Garon, M. Thompson, *Applied Physics Letters*, 82(15):2422-2424 (2003).
- (45) M. Stolka, J. F. Yanus, and D. M. Pai, *The Journal of Physical Chemistry*, 88(20):4707-4714 (1984).
- (46) C. Adachi, T. Tsutsui, S. Saito, *Applied Physics Letters*, 55(15):1489-1491 (1989).
- (47) S. Feng, *Doctoral dissertation, Tsinghua University*, 2012.
- (48) M. A. Baldo, M. E. Thompson, S. R. Forrest, *Nature*, 403(6771):750-753 (2000).
- (49) B.W. D'Andrade, M. Thompson, S.R. Forrest, *Advanced Materials*, 14(2):147-151 (2002).
- (50) Q. Zhang, J. S. Chen, Y. X. Cheng, L. X. Wang, D. G. Ma, X. B. Jing, F. S. Wang, *Journal of Materials Chemistry*, 14(5):895-900 (2004).
- (51) J. Thomas K R, J. T. Lin, Y. T. Tao, and C. W. Ko, *Advanced*

Materials, 12(24):1949-1951 (2000).

(52) S. W. Shi, Y. F. Li, X. Y. Li, and H. Q. Wang, *Materials Horizons*, 2(4):378-405 (2015).

Chapter 2 Design, synthesis and application of hole-conducting materials contain Spiro group

- I . Introduction
- II. Experiment content
 - II-1. Material structures and instrument
 - II-2. Synthesis and characterization
 - II-3. OLED fabrication and measurements
- III. Results and discussion
 - III-1. Simulation of Homo and LUMO values
 - III-2. Photophysical properties
 - III-3. Electrochemical properties
 - III-4. Thermal stability
 - III-5. Device application of Spiro compounds
- IV. Chapter summary

I . Introduction

Hole-transporting materials (HTMs) are integral to the construction of a wide variety of state-of-the-art semiconductor devices today.⁽¹⁾ Considerable research effort has been devoted to improve the lifetime of organic light-emitting diodes (OLEDs) by optimizing each functional layer.⁽²⁻⁸⁾ The electrochemical stability and hole mobility of the hole-transporting layer (HTL) strongly influence the device lifetime.⁽⁹⁻¹³⁾ Of course, there are other necessary criteria, which should be additionally met before an easily-oxidizable organic compound can be employed as a HTM in OLED devices. These criteria are as follows ⁽¹⁴⁾: First, a HTM should preferably exhibit reversible redox properties and possess a low oxidation potential to aid facile removal of an electron from the HOMO. Second, the HOMO energy of a HTM should be comparable to that of the work-function of the employed anode

(typically ITO) to ensure facile injection of holes. Third, it should possess good thermal stability and amorphous properties.

A large number of small molecules as well as polymeric materials that meet the above criteria and exhibit hole-transporting properties have been developed over recently years. In addition, It is important for the EBL to have an amorphous glassy state, which prevents grain boundaries and ensures spatial homogeneity of the transport properties. The EB material of linear planar arrangement structure type has a lower glass-transition temperature ($T_g < 100^\circ\text{C}$).⁽¹⁵⁾ Rigid orthogonal planes in a molecule considerably improve the thermal stability. Bach et al.⁽¹⁶⁾ reported that spirobifluorenes display high thermal and morphological stabilities. Wong and coworkers⁽¹⁷⁾ capitalized on this idea and reported a series of differently functionalized spirobifluorenes, which displayed moderate T_g s in the range of $112\sim 156^\circ\text{C}$. The spirocyclic compounds, however, display low hole mobilities at the expense of minimization of intermolecular interactions.

In the present work, we synthesized four compounds, **BFS2A**, **BFS3A**, **SF2DDA** and **SF4DDA** (Fig.1). Among them, **BFS2A** and **BFS3A** based on a spiro backbone with dimethylfluorene side-chain groups to impart hole-transporting properties and electrochemical stability to electron-blocking materials in the hole-transporting region of OLEDs. The introduction of double bonds improves the hole mobility of the compound, and the excellent hole transport performance allows more holes to be injected into the light-emitting layer, and the light-emitting recombination area is far away from the interface between EBL and emitting layer, which effectively prevents the accumulation of excitons at the interface and promotes the stability of the devices. Therefore, the devices exhibit satisfactorily long lifetime.⁽¹⁸⁾ **SF2DDA** and **SF4DDA** based on spirocyclic feature with the parallel ring structure can improve T_g more obviously, and the planar structure improves the hole-transporting performance. These materials exhibited high electrochemical and thermal stability. The improved lifetime of multilayer OLEDs based on the four materials proved that they have the potential as EBL application, which is closely related to the good carrier transport properties of them.

II. Experiment content

II-1. Material structures and instrument

The materials used in this study are shown in Fig.1. Organic materials including a hole-injection material, **HATCN**, a hole-transport material, **BPBPA**, a reference electron-blocking material, **SF2AF**, a fluorescent host, **BH**, a fluorescent dopant, **BD**, electron-transport materials **ZADN** and **LiQ** were obtained from Valiant Company.⁽¹⁹⁻²⁰⁾ The synthesis and preparation of electron-blocking materials **BFS2A** and **BFS3A** are described below. ¹H NMR and ¹³C NMR spectra were measured on an AVIII 400-MHz spectrometer (Bruker Technology Co., Ltd.) in deuterated chloroform with tetramethylsilane as a reference. Liquid chromatography–mass spectrometry (LC-MS) was performed using a 6460 LC-MS instrument (Agilent Technologies, Inc.). For photophysical characterization, 80nm-thick films were deposited by thermal sublimation onto pre-cleaned silica substrates. Ultraviolet–visible (UV-vis) absorption and photoluminescence (PL) spectra of the films were measured by using an HP-8453 UV-vis Spectrophotometer (Agilent Technologies, Inc.) and a Fluoromax-4 spectrophotometer (Horiba Ltd.), respectively. Differential scanning calorimetry (DSC) were obtained using a DSC 200F3 Netzsch analyzer with a heating rate of 10°C·min⁻¹ and a cooling rate of 20°C·min⁻¹ under a nitrogen atmosphere. Film crystallization heat resistance experiment was carried out to confirm whether the surface of films crystallized after heating for a long time on an electric blast drying oven (DHG-9030A type Shanghai Huitai Instrument Manufacturing Co., Ltd.). These films were stood at 80°C for 1000 h and at 115°C for 200 h. The surface of films were observed with an optical microscope (DM8000M Leica, Germany). HOMO energy levels were measured by an IPS-3 ionization potential spectrometer (Bunkoukeiki Co., Ltd.). Cyclic Voltammetry (CV) was conducted on a CorrTest-CS150 instrument (Wuhan Corrttest Instruments Co., Ltd.) in anhydrous CH₂Cl₂ using tetrabutylammonium hexafluorophosphate as a supporting electrolyte with a scan rate of 100 mV·s⁻¹. All the materials for OLED devices were further purified by sublimation under vacuum conditions and obtained purities more than 99.9%.

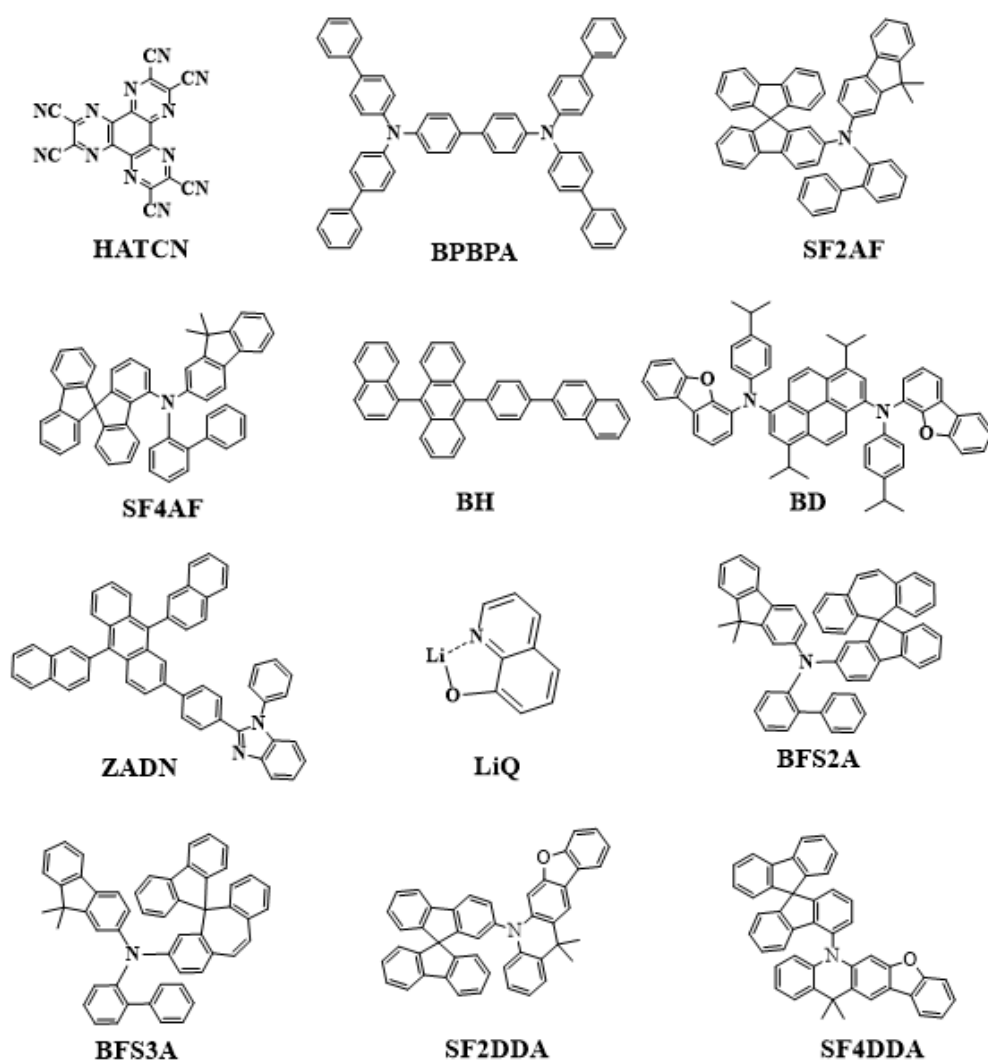
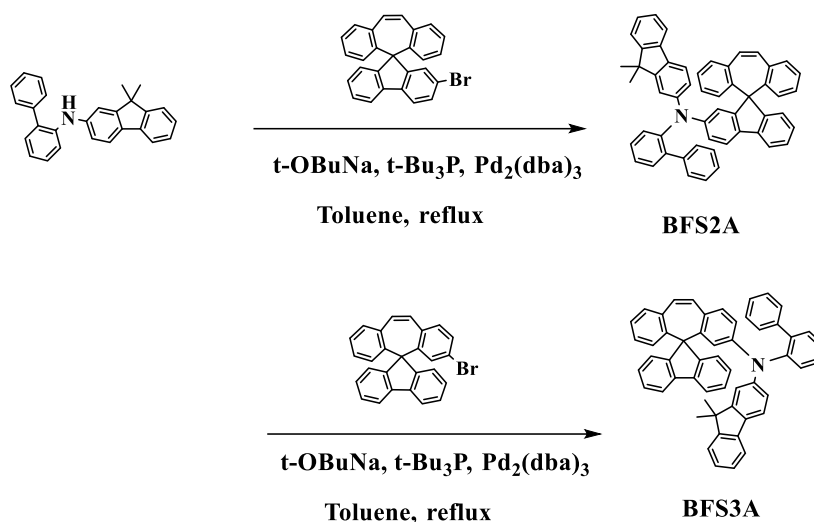


Fig.1 Molecular structures of the materials used

II-2. Synthesis and characterization

II-2-1. Synthesis and characterization of BFS2A and BFS3A

The synthesis routes of **BFS2A** and **BFS3A** are shown in Scheme 1. N-([1,1'-biphenyl]-2-yl)-9,9-dimethyl-9H-fluoren-2-amine was prepared and coupled to a spiro core to prepare **BFS2A** and **BFS3A**. Characterization of the synthesized materials by ^1H and ^{13}C spectroscopy (Fig.S1) and LC-MS confirmed their chemical structure.



Scheme 1 Synthetic scheme of **BFS2A** and **BFS3A**

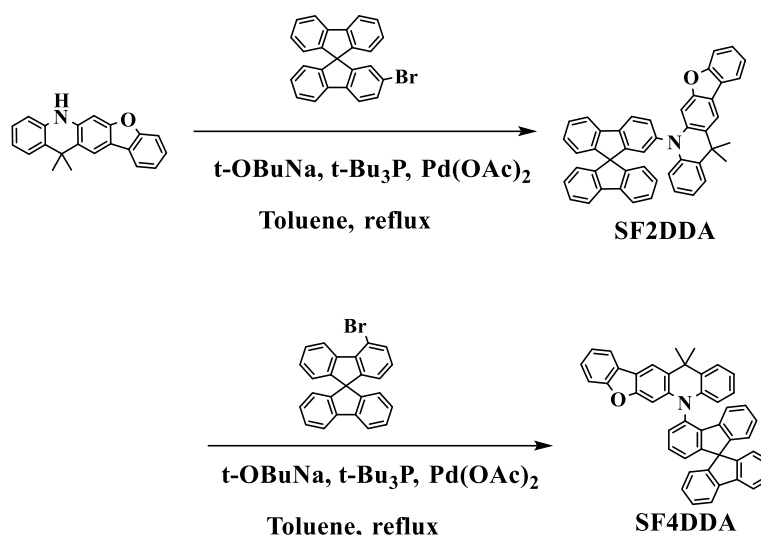
The synthesis method of **BFS2A** is as follows: a mixture of N-([1,1'-biphenyl]-2-yl)-9,9-dimethyl-9H-fluoren-2-amine (451.5 mg, 1.25 mmol), 2'-bromospiro[dibenzo[a,d][7]annulene-5,9'-fluorene] (693.1 mg, 1.65 mmol), *t*-BuONa (173.5 mg, 1.88 mmol), Pd₂(dba)₃ (34.8 mg, 0.038 mmol), *t*-Bu₃P (10% in toluene solution, 0.23 mL, 0.25 mmol) and dry toluene (25 mL) were added in flask. After stirring and degassing, the resulting mixture was refluxed for 24 h under a nitrogen atmosphere. After cooled to room temperature, dichloromethane (35 mL) was added and stirred for 30 min. The organic layer was washed with water and brine, dried over anhydrous MgSO₄, filtered, and concentrated in vacuum. The residue was recrystallized in the methanol to provide off-white crude product, and subsequently it was purified by silica gel column chromatography using dichloromethane/petroleum at 1:15 by volume as the eluant to afford pure white product (723 mg, 82.5% yield). ¹H NMR (400 MHz, Chloroform-*d*) δ = 7.72 (d, *J* = 7.6 Hz, 1H), 7.59 (d, *J* = 8.3 Hz, 1H), 7.51 (d, *J* = 7.1 Hz, 1H), 7.40 (s, 1H), 7.35 – 7.26 (m, 7H), 7.25 – 7.16 (m, 4H), 7.15 – 7.04 (m, 5H), 7.03 – 6.95 (m, 4H), 6.94 – 6.69 (m, 6H), 6.62 – 6.43 (m, 3H), 1.00 (s, 3H), 0.97 (s, 3H). ¹³C NMR (100 MHz, Chloroform-*d*) δ = 154.25, 153.51, 147.43, 146.97, 146.61, 144.69, 143.31, 139.14, 135.33, 134.37, 131.92, 129.79, 129.55, 128.80, 128.40, 128.38, 127.79, 127.69,

127.38, 127.13, 126.96, 126.84, 126.09, 125.93, 123.29, 122.37, 122.32, 121.65, 121.28, 121.09, 120.78, 120.10, 119.64, 119.20, 116.71, 116.10, 68.43, 46.48, 26.80, 26.74. MS m/z (ESI) Calcd for C₅₄H₃₉N: 701.31; Found: 702.84 [M+H]⁺.

The synthesis method of **BFS3A** is as follows: a mixture of N-([1,1'-biphenyl]-2-yl)-9,9-dimethyl-9H-fluoren-2-amine (451.5 mg, 1.25 mmol), 2'-bromospiro[dibenzo[a,d][7]annulene-5,9'-fluorene] (693.1 mg, 1.65 mmol), *t*-BuONa (173.5 mg, 1.88 mmol), Pd₂(dba)₃ (34.8 mg, 0.038 mmol), *t*-Bu₃P (10% in toluene solution, 0.23 mL, 0.25 mmol) and dry toluene (25 mL) were added in flask. After stirring and degassing, the resulting mixture was refluxed for 24 h under a nitrogen atmosphere. After cooled to room temperature, dichloromethane (35 mL) was added and stirred for 30 min. The organic layer was washed with water and brine, dried over anhydrous MgSO₄, filtered, and concentrated in vacuum. The residue was recrystallized in the methanol to provide off-white crude product, and subsequently it was purified by silica gel column chromatography using dichloromethane/petroleum at 1:15 by volume as the eluant to afford pure white product (708 mg, 80.8% yield). ¹H NMR (400 MHz, Chloroform-d) δ 7.85 (d, *J* = 7.5 Hz, 2H), 7.51 (d, *J* = 7.1 Hz, 1H), 7.47 (s, 1H), 7.42 (d, *J* = 7.4 Hz, 1H), 7.37 (td, *J* = 1.1, 7.5 Hz, 2H), 7.33 – 7.27 (m, 3H), 7.26 – 7.18 (m, 6H), 7.15 (dt, *J* = 3.8, 7.5 Hz, 2H), 7.00 – 6.87 (m, 8H), 6.75 (d, *J* = 8.9 Hz, 2H), 6.69 (d, *J* = 2.0 Hz, 1H), 6.61 (dd, *J* = 2.8, 8.6 Hz, 3H), 6.45 (d, *J* = 7.6 Hz, 1H), 1.23 (s, 6H). ¹³C NMR (100 MHz, Chloroform-d) δ 154.14, 153.52, 148.88, 147.51, 147.26, 144.70, 141.80, 140.52, 139.69, 133.18, 131.85, 129.35, 128.70, 128.51, 127.96, 127.77, 127.72, 127.67, 127.19, 126.90, 126.71, 126.54, 126.22, 125.84, 125.52, 123.61, 122.43, 122.37, 121.97, 120.74, 120.54, 119.99, 119.33, 117.57, 46.64, 27.05. MS m/z (ESI) Calcd for C₅₄H₃₉N: 701.31; Found: 702.89 [M+H]⁺.

II-2-2. Synthesis and characterization of SF2DDA and SF4DDA

The synthesis routes of **SF2DDA** and **SF4DDA** are shown in Scheme 2. 12,12-dimethyl-7,12-dihydrobenzofuro[3,2-*b*]acridine and 9,9'-spirobi[fluorene] was coupled to prepare **SF2DDA** and **SF4DDA**. Characterization of the synthesized materials by ^1H and ^{13}C spectroscopy (Fig.S2) and LC-MS confirmed their chemical structure.



Scheme 2 Synthetic scheme of **SF2DDA** and **SF4DDA**

The synthesis method of **SF2DDA** is as follows: 12,12-dimethyl-7,12-dihydrobenzofuro[3,2-*b*]acridine (3.590 g, 0.012 mol) and 2-bromo-9,9'-spirobi[fluorene] (3.940 g, 0.01 mol) were dissolved in 150 ml anhydrous toluene in a round bottom flask under a nitrogen atmosphere. *t*-BuONa (2.883 g, 0.03 mol), Pd(OAc)₂ (22.5 mg, 1×10⁻⁴ mol) and *t*-Bu₃P (1.0 M in toluene solution, 50 μL, 5×10⁻⁵ mol) were added to the solution. The reaction mixture was refluxed for 24 h at 105°C. After cooling to room temperature, the mixture was filtered and the filtrate was evaporated under reduced pressure to remove solvent. The residue was purified by silica gel column chromatography to afford pure white product (4.863 g, 79.3% yield). ^1H NMR (400 MHz, Chloroform-*d*) δ 8.13 (dd, *J* = 8.0, 0.6 Hz, 1H), 7.94 (dt, *J* = 7.6, 1.0 Hz, 1H), 7.90 (s, 1H), 7.85 – 7.80 (m, 1H), 7.78 (dt, *J* = 7.6, 1.0 Hz, 2H), 7.48 – 7.37 (m, 4H), 7.36 – 7.22 (m, 4H), 7.16 (dtd, *J* = 10.5, 7.5, 1.1 Hz, 3H), 6.96 – 6.84 (m, 4H), 6.81 – 6.73 (m, 2H), 6.40 (s, 1H), 6.27 – 6.23 (m, 1H), 1.68 (s, 6H). ^{13}C NMR (100 MHz, Chloroform-*d*) δ 156.13, 155.56, 152.07, 149.52, 148.07, 142.13, 141.78, 141.55, 140.80, 140.69, 140.34, 130.77, 130.03, 128.36,

128.04, 127.94, 126.94, 126.43, 126.34, 125.30, 124.84, 124.71, 124.19, 123.89, 122.49, 122.16, 120.81, 120.32, 120.08, 119.48, 116.97, 116.61, 114.11, 111.07, 96.82, 36.36, 31.21. MS m/z (ESI) Calcd for C₄₆H₃₁NO: 613.24; Found: 614.56 [M+H]⁺.

The synthesis method of **SF4DDA** is as follows: 12,12-dimethyl-7,12-dihydrobenzofuro[3,2-*b*]acridine (3.590 g, 0.012 mol) and 4-bromo-9,9'-spirobi[fluorene] (3.940 g, 0.01 mol) were dissolved in 150 ml anhydrous toluene in a round bottom flask under nitrogen atmosphere. *t*-BuONa (2.883 g, 0.03 mol), Pd(OAc)₂ (22.5 mg, 1×10⁻⁴ mol) and *t*-Bu₃P (1.0 M in toluene solution, 50 μL, 5×10⁻⁵ mol) were added to the solution. The reaction mixture was refluxed for 24 h at 105°C. After cooling to room temperature, the mixture was filtered and the filtrate was evaporated under reduced pressure to remove solvent. The residue was purified by silica gel column chromatography to afford pure white product (5.010 g, 81.7% yield).

¹H NMR (400 MHz, Chloroform-*d*) δ 8.10 (dd, *J* = 8.0, 0.6 Hz, 1H), 7.92 – 7.87 (m, 3H), 7.64 – 7.60 (m, 1H), 7.47 – 7.38 (m, 3H), 7.38 – 7.23 (m, 6H), 7.23 – 7.16 (m, 1H), 7.06 – 6.88 (m, 6H), 6.81 (dd, 1H), 7.72 – 7.66 (m, 1H), 6.59 (s, 1H), 6.50 – 6.42 (m, 1H), 2.09 (s, 3H), 1.80 (s, 3H). ¹³C NMR (100 MHz, Chloroform-*d*) δ 156.17, 156.00, 151.78, 148.74, 148.44, 148.24, 141.85, 141.82, 141.70, 139.88, 139.26, 139.16, 134.92, 130.51, 130.45, 130.03, 128.27, 128.20, 128.17, 128.00, 127.96, 127.03, 126.46, 125.98, 125.48, 124.72, 124.45, 124.31, 123.97, 123.62, 123.57, 122.60, 121.09, 120.19, 120.12, 119.52, 117.89, 117.32, 114.02, 111.10, 96.56, 36.50, 31.80. MS m/z (ESI) Calcd for C₄₆H₃₁NO: 613.24; Found: 612.29 [M-H]⁻.

II-3. OLED fabrication and measurements

Fig.2(a) shows the ionization potential of each functional layer and device matching about materials with low HOMO level. The HOMO energy levels of **BFS2A** and **BFS3A** were measured to be -5.5 and -5.47 eV, respectively. The smaller hole-injection barrier (0.01 eV) from **BPBPA** to **BFS3A** may make contribution to a lower voltage of OLED. According to the formula: $E_{\text{HOMO}} = E_{\text{LUMO}} - E_g$, the calculated LUMO energy levels of **BFS2A** and **BFS3A** were

-2.42 and -2.58 eV, respectively. A shallow LUMO value can effectively prevent electron leakage from emissive layer into the HTL.⁽²¹⁾ To investigate the electroluminescence performance of the **BFS2A** and **BFS3A**, OLEDs were fabricated. The thicknesses of the EBLs were optimized to balance the carriers and increase exciton utilization.

Fig.2(b) shows the ionization potential of each functional layer and device matching about materials with high HOMO level. The HOMO energy levels of **SF2DDA** and **SF4DDA** were measured to be -5.62 and -5.69 eV, respectively. Compared with **BFS2A** and **BFS3A**, **SF2DDA** and **SF4DDA** have larger energy level difference and better injection ability.

The OLEDs were fabricated by vacuum thermal deposition on a glass substrate coated with indium tin oxide (ITO, thickness =150 nm) as the anode, and the weight ratio of BH and BD was 100:5. Before device fabrication, the glass substrates were cleaned sequentially with detergent (SemiClean M-L20) and deionized water, and then dried in a vacuum oven at 250°C for about 30 min. Next, the cleaned glass substrate was treated with argon plasma for 5 minutes to remove organic residues and increase the ITO work function. Finally, all organic layers and a metal cathode layer were evaporated under high vacuum (1.0×10^{-6} torr); the thickness and deposition rate of each layer were controlled through a quartz-crystal thickness monitor. The deposition rates of the organic layers were in the range of 0.5–1 Å·S⁻¹. The active area of the OLEDs was 4 mm². After the thin-film deposition, the devices were encapsulated in a nitrogen-purged glove box. Current density–voltage–current efficiency measurements were recorded with a Keithley 2400 source meter, and the electroluminescence spectra were obtained using a Minolta CS-2000 spectroradiometer. The OLED lifetime was measured using an EAS-62C device (Japan SYSTEM Technology Co., Ltd.) with an Electrical Aging lifetime operating system. The operational lifetime (LT90), which is defined as the time at which the luminance drops to 90% of its initial value, and the OLEDs was determined under a constant current 10 mA·cm⁻² and temperature of 25°C with a varying initial brightness levels.

The OLED structures are as follows.

ITO/HATCN (10 nm)/BPBPA (X nm)/SF2AF (Y nm)/BH: 5wt% BD (25 nm)/ZADN: Liq= 1:1 (35 nm)/Al (80 nm).

ITO/HATCN (10 nm)/BPBPA (X nm)/SF4AF (Y nm)/BH: 5wt% BD (25 nm)/ZADN: Liq= 1:1 (35 nm)/Al (80 nm).

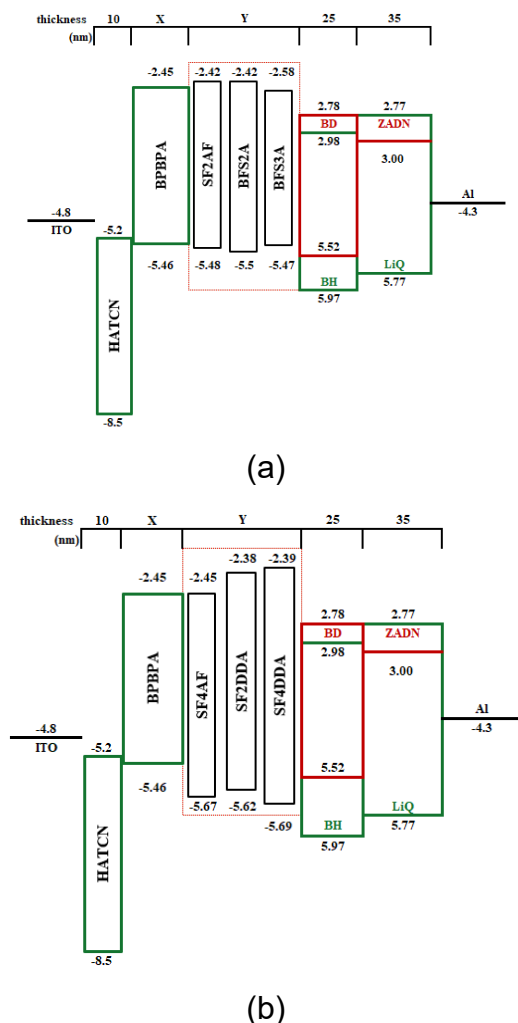


Fig.2 The frontier orbital energy levels and thicknesses of the organic materials .

III. Results and discussion

III-1. Simulation of Homo and LUMO values

To verify the suitability of these four synthetic structures as electron-blocking materials, the HOMO–LUMO distribution was predicted using electronic orbital calculations. Fig.3 shows the distribution of HOMO–LUMO.

The HOMO of **BFS2A** and **BFS3A** was distributed on part of the spiro, side fluorene unit and one benzene of side chain biphenyl, which indicates that they may work as hole transporting carriers through extensive intermolecular p-orbital overlap.⁽²²⁾ The LUMO distribution of both **BFS2A** and **BFS3A** mainly

populates on the spiro backbone, but the LUMO distribution of **BFS3A** populates a small residue on the 9,9-dimethyl-9*H*-fluorene unit. The separation between HOMO and LUMO levels might be favorable to the efficient hole transporting behaviors,⁽²³⁾ which indicates that **BFS2A** might has better hole transport than that of **BFS3A**.

For **SF2DDA** and **SF4DDA**, the HOMO was distributed at the dimethyl dihydroacridofuran. Different from the above two structures, the attachment site of the side chain group is different, but the HOMO distribution is same. This may be due to different structural types of compounds. The side chains of **BFS2A** and **BFS3A** are connected by nitrogen atoms, while **SF2DDA** and **SF4DDA** are connected directly.

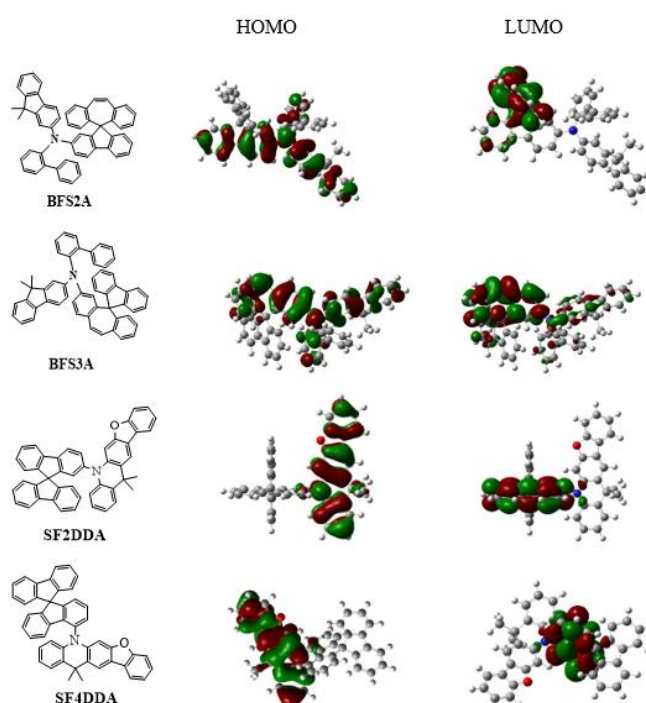


Fig.3 HOMO and LUMO of **BFS2A** , **BFS3A**,**SF2DDA** and **SF4DDA**

III-2. Photophysical properties

Fig.4(a) shows the UV–visible absorption and photoluminescence emission spectra of **BFS2A** and **BFS3A** thin films. The optical band gaps (E_g) were estimated from the intersections of the absorption spectra, according to the formula, $E_g^{\text{opt}}=1240/\lambda_{\text{onset}}$, to be 3.08 and 2.89 eV, respectively. Compared with **BFS2A**, the UV–visible absorption spectrum of **BFS3A** was red-shifted owing

to the enhanced molecular conjugation of **BFS3A** caused by the differences in the modifying positions of the spiro backbone.⁽²⁴⁾ It is noted that **BFS2A** and **BFS3A** hardly absorb light at wavelengths longer than 420 nm, indicating their high transparency to visible light and thus high light-collecting efficiency. The photoluminescence spectrum of the **BFS3A** also red-shifted, and the peak wavelengths of the **BFS2A** and **BFS3A** were 407 and 437 nm, respectively. The triplet-energies (E_T) were calculated from the first triplet emission peak of the low-temperature photoluminescence spectrum measured in cryogenic medium (liquid N₂) at 77 K. The E_T values for **BFS2A** and **BFS3A** were 2.66 and 2.04 eV, respectively, which were higher than that of BH. This indicates that **BFS2A** and **BFS3A** as EBLs in blue fluorescent OLEDs can confine triplet excitons within the emitting layer.⁽²⁵⁾

Fig.4(b) shows the UV–visible absorption and photoluminescence emission spectra of **SF2DDA** and **SF4DDA** thin films. The UV absorption spectra and photoluminescence of the two materials have little difference. The optical band gaps (E_g) was 3.24 and 2.89 eV, respectively. This shows that the two materials do not absorb blue light. The E_T values for **SF2DDA** and **SF4DDA** have the same E_T value 2.71 eV, which indicates that these materials can confine triplet excitons within the emitting layer.

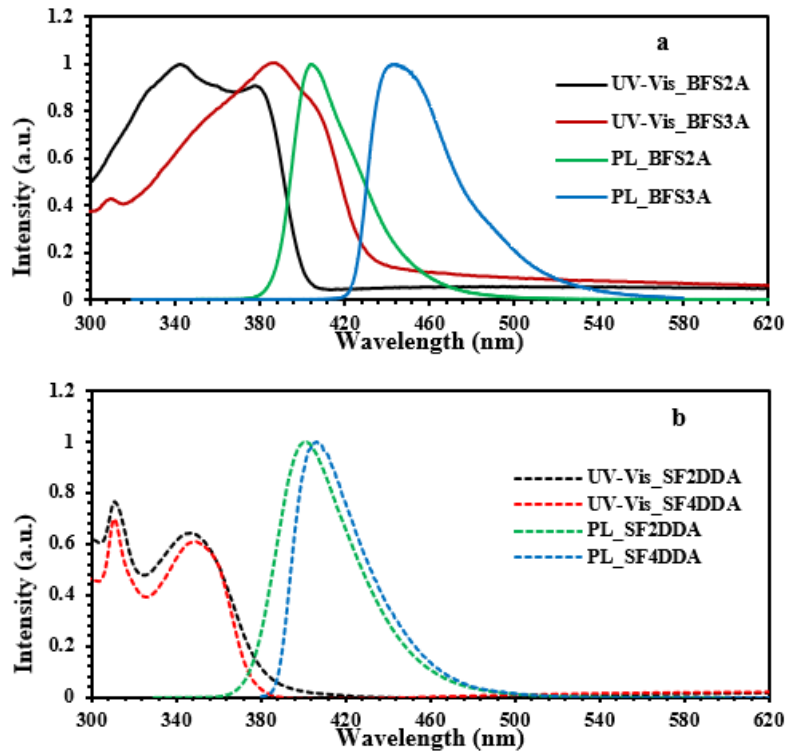


Fig.4 (a) UV–visible absorption and photoluminescence emission spectra of **BFS2A**

and **BFS3A**,(b) UV–visible absorption and photoluminescence emission spectra of **SF2DDA** and **SF4DDA**.

III-3. Electrochemical properties

CV was conducted to evaluate the electrochemical properties of **BFS2A**, **BFS3A**, **SF2DDA** and **SF4DDA** at room temperature. Fig.5 shows the CV scans of 100 cycles of the four materials exhibit nearly identical curve profiles, oxidation potential and current values. From these curves, we conclude that these materials have high electrochemical stability, which is crucial for achieving good device performance.^(18,26)

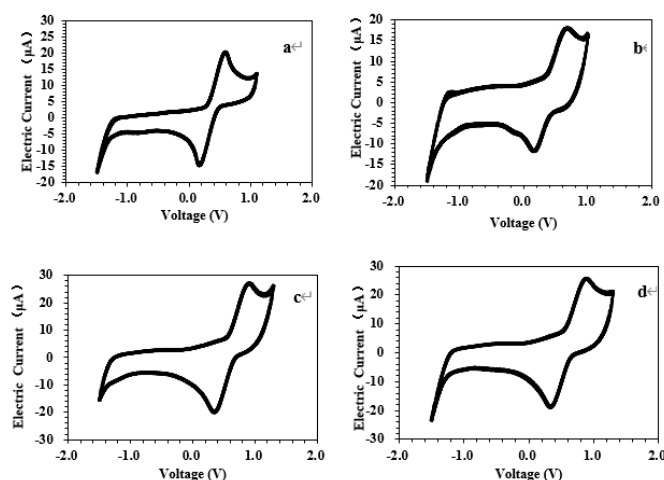


Fig.5 Cyclic voltammograms for **BFS2A** (a) , **BFS3A** (b),**SF2DDA**(c) and **SF4DDA**(d)

III-4. Thermal stability

The thermal properties of BFS2A, BFS3A, SF2DDA and SF4DDA were investigated using DSC and film crystallization heat resistance experiment. The DSC curves of BFS2A and BFS3A shown in the Fig.S3. The T_g values of these structures are 136, 132, 146 and 152°C, respectively. Because these structures had high T_g (T_g>120 °C), the materials were not easily crystallized after film formation. Both films in Fig.6 showed smooth surface morphology with a thickness of 80 nm. We attribute the high thermal stability to the rigidity provided by the spiro backbone. High thermal stability is essential for maintaining the stability of device performance by preventing crystallization, and reducing the formation of grain boundaries and defects. The physical data of BFS2A, BFS3A, SF2DDA, SF4DDA, SF2AF and SF4F are summarized in Table 1.

Table 1 Physical data for **BFS2A**, **BFS3A** and **SFAF**

Compound	$\lambda_{\max}^{\text{abs}}/n$ m	$\lambda_{\max}^{\text{em}}/n$ m	HOMO/eV	LUMO/eV	E_g /eV	ET	$T_g/^\circ\text{C}$
BFS2A	378	407	-5.5	-2.42	3.08	2.66	136
BFS3A	386	437	-5.47	-2.58	2.89	2.04	132
SF2DDA	348	409	-5.62	-2.38	3.24	2.71	146
SF4DDA	349	404	-5.69	-2.39	3.30	2.71	152
SF2AF	378	402	-5.48	-2.42	3.06	2.52	140
SF4AF	342	407	-5.67	-2.46	3.21	2.59	138

a: Film UV

b: Excited at the absorption maxima.

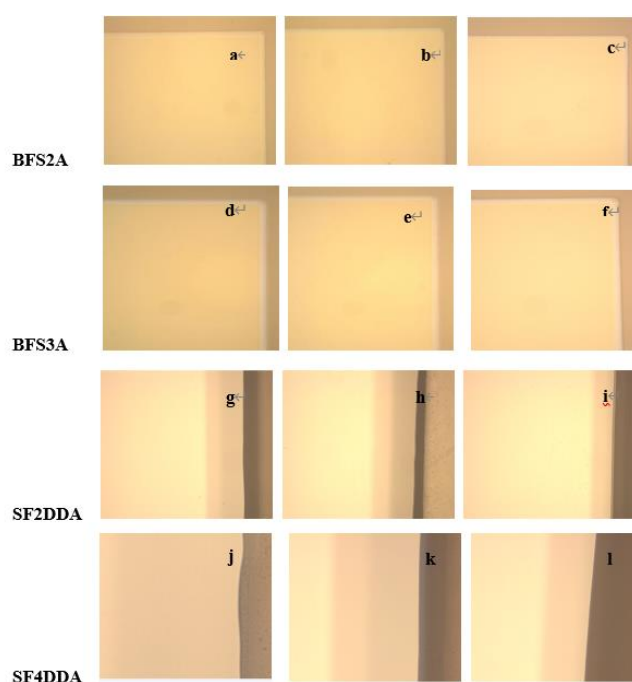


Fig.6 Surface morphology films of **BFS2A** as-deposited (a), annealed at 85°C (b) and annealed at 115°C (c); Surface morphology films of **BFS3A** as-deposited (d), annealed at 85°C (e) and annealed at 115°C (f). Surface morphology films of **SF2DDA** as-deposited (g), annealed at 85°C (h) and annealed at 115°C (i); Surface morphology films of **SF2DDA** as-deposited (j), annealed at 85°C (k) and annealed at 115°C (l).

III-5. Device application of Spiro compounds

To investigate the influence of the spiro backbone on the EL performances of the structures, devices using these two series of structures as electron-blocking material were fabricated, respectively.

Table 2 Key characteristics of devices with A-C different EBLs and thicknesses

Device	EBL Thickness (nm)	Voltage	CE (cd/A)	Luminance (cd/m ²)	CIE x	CIE y	LT90(h)
A1	SF2AF (10)	3.96	9.62	962	0.12	0.17	1285
A2	BFS2A (10)	4.11	8.88	888	0.12	0.18	1265
A3	BFS3A (10)	3.90	9.26	926	0.13	0.16	989
B1	SF2AF (50)	3.92	8.20	820	0.12	0.18	724
B2	BFS2A (50)	3.90	10.46	1047	0.12	0.17	1592
B3	BFS3A (50)	3.94	9.26	926	0.13	0.17	1805
C1	SF2AF (120)	4.25	7.62	762	0.13	0.16	167
C2	BFS2A (120)	4.18	8.46	846	0.13	0.15	1145
C3	BFS3A (120)	4.14	7.93	793	0.13	0.15	1329

Recorded at 10 mA·cm⁻²

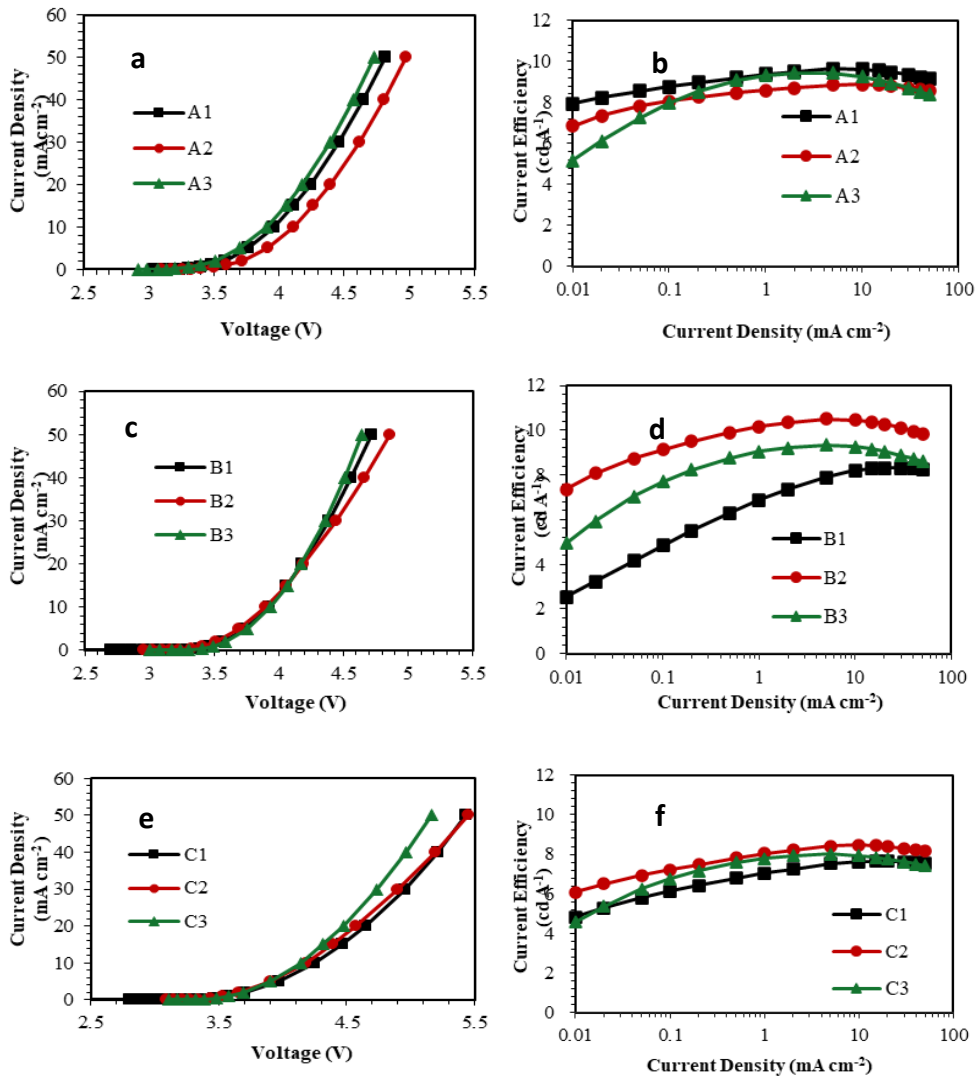


Fig.7 Electrical characteristics of the fabricated devices A-C with **SF2AF**, **BFS2A** and **BFS3A**

The current density–voltage (J–V) and current efficiency (CE) characteristics of the fabricated devices A–C with **SF2AF**, **BFS2A** and **BFS3A** are shown in Fig.7, and EL data are summarized in Table 2. Fig.7a shows that the voltage values of devices A1–A3 with **SF2AF**, **BFS2A** and **BFS3A** of 10 nm were 3.96 V, 4.11 V and 3.90 V at 10^{-2} mA·cm⁻², respectively, which verified that a larger hole injection barrier from HTL to EBL will cause an increase in voltage. As shown in Fig.7b, the CEs of devices A2 and A3 were lower than that of device A1 at low current densities ($\sim 10^{-2}$ mA·cm⁻²), which may be due to unbalanced carrier injection. However, this difference decreased with enhanced electron transporting at higher current densities (>1 mA·cm⁻²), mainly owing to the improved carrier balance. The CE roll-off characteristics of each device were also obviously different. The CE of device A1 decreased from 9.62 cd·A⁻¹ at 10 mA·cm⁻² to 9.15 cd·A⁻¹ at 50 mA·cm⁻², and the reduced CE value was 0.49 cd·A⁻¹. However, the CE of device A2 just started to decrease at higher current densities of 15 mA·cm⁻², which was attributed to the increase of charge balance, and the reduced CE value was 0.16 cd·A⁻¹ smaller than that of device A1. Compared with devices A1 and A2, device A3 began to show a decrease in CE at a lower current density of 5 mA·cm⁻², and the CE value reduced by 1.08 cd·A⁻¹. The difference in EQE roll-off of these three devices was further visually reflected in the corresponding difference in device lifetime, which was due to the degradation caused by continuous quenching during operation.

The thickness of EBL is one of the crucial factors affecting the carrier balance of the device. Therefore, we also fabricated and tested devices B1–B3 with **SF2AF**, **BFS2A** and **BFS3A** of 50 nm, keeping the total thickness of the hole transport region unchanged, respectively. Fig.7(c, d) shows that the voltage of device B2 significantly reduced and the voltages of devices B1 and B3 hardly changed, the voltages of the three were almost the same, at 10 mA·cm⁻². The CE of device B1 was greatly reduced, indicating that the hole and electron balance was poor. In contrast, the CE of device B2 increased from 8.88 cd·A⁻¹ to 10.46 cd·A⁻¹ at 10 mA·cm⁻². The increased thickness of EBL had no obvious effect on the CE of device B3. These results indicated that devices B2 and B3 had better carrier balance than device B1, thus revealing that **BFS2A** and **BFS3A** have better hole transport mobilities than **SF2AF**.

To further explore the hole transport ability of **SF2AF**, **BFS2A** and **BFS3A**,

we increased the thickness of EBL to 120 nm and fabricated devices C1-C3, respectively. Fig.7(c, d) shows that the increased thickness of EBL led to obvious increase of voltage and decrease of CE. Compared with devices A1–A3, the voltages of devices C1–C3 increased by 0.29, 0.07, and 0.24 V, and the CE decreased by 20.8%, 4.7%, and 14.4%, respectively. These results revealed that the hole transport performance of **BFS2A** was the best among the three materials.

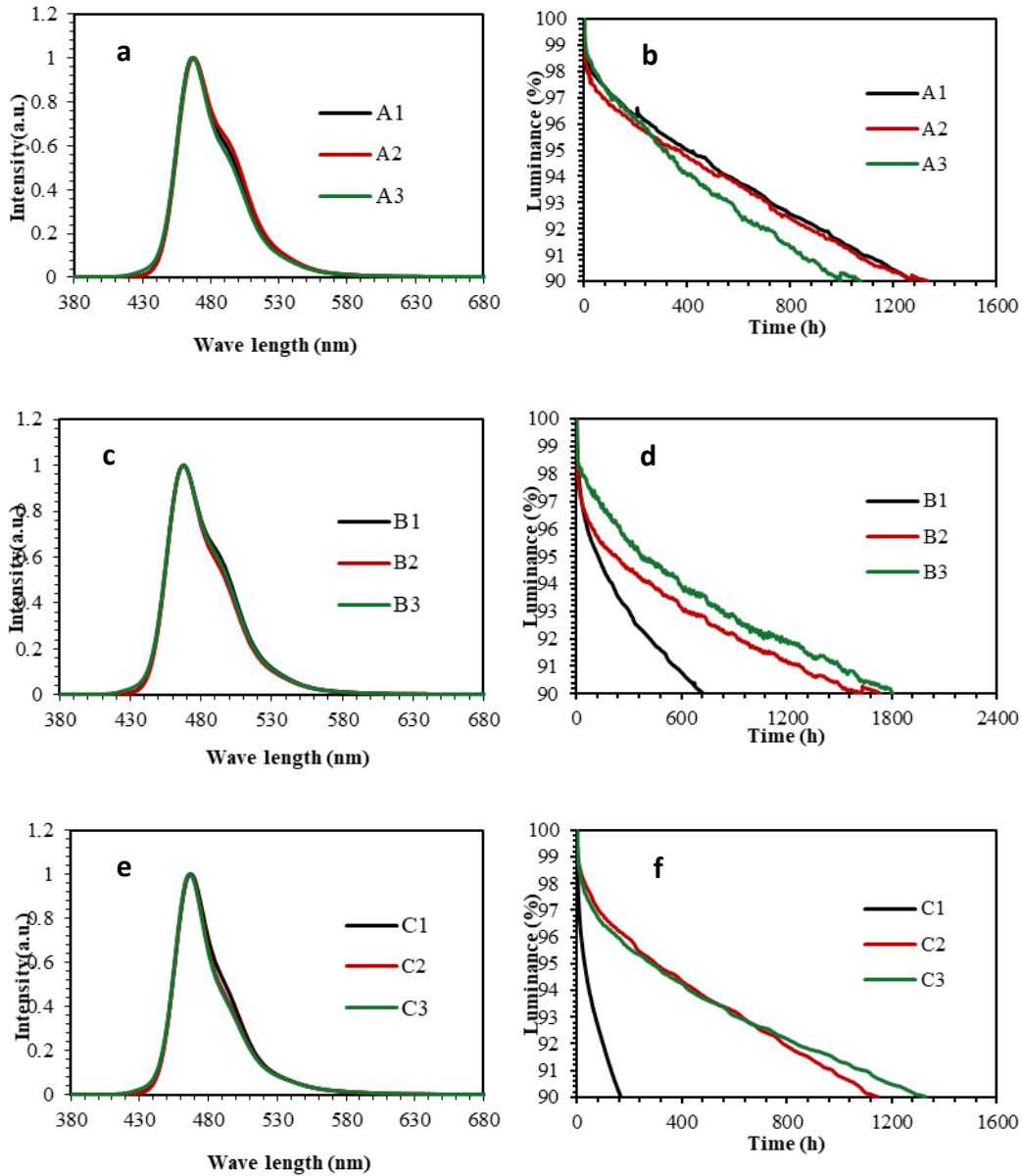


Fig.8 The normalized EL spectra (a,c,e) of the devices and device lifetime (b,d,f) at 10 mA·cm⁻²

The pure blue emission from the EL spectra of all devices is attributed to

the emission of BD, and no detectable exciplex emission at long wavelengths is observed in Fig.8(a,c,e), which indicates that **BFS2A** and **BFS3A** have good hole mobility and can effectively transport holes into the emitting layer. The LT90 of the devices A1–A3 were 1285, 1265 and 989 h, respectively, a longer lifetime is usually related to a better charge balance. Device A3 had a lower voltage and current efficiency, but its lifetime was shorter than that of device A1, which may be due to the instability of the thin film of **BFS3A** near the exciton recombination area.⁽²⁹⁾ Compared with that of devices A1–A3, the LT90 of devices B1–B3 increased by -43.7%, 25.8% and 82.5%, respectively, suggesting that the devices B2 and B3 have broadened exciton recombination zone which resulted in lower exciton density and reduced severity of bimolecular quenching processes. Without changing the structure of the EML, the hole mobility in the EML of devices B2 and B3 can be adjusted to achieve balanced electron and hole mobilities by increasing the proportion of the EBL in the hole transport region. When the thickness of EBL was increased from 10 nm to 120 nm, the LT90 of device C1 was significantly decreased by 87%, while the LT90 of device C2 and C3 was increased by -1% and 34.4%, respectively. The results demonstrate that when **BFS2A** and **BFS3A** are used as electron-blocking materials, they can not only improve the carrier balance of the devices, but also reduce the accumulation of excitons at the interface between EBL and EML, thus prolonging the lifetime of the devices. Therefore, considering the voltage, the current efficiency and the lifetime, we conclude that the optimum thickness for **BFS2A** and **BFS3A** is 50 nm among EBL thicknesses of 10, 50, and 120 nm. We attribute this to a better charge balance and the E_T being higher than that of the host, thus confining electrons and excitons within the EML.^(30,31)

Table 3 Calculated value of μ_0 and β

Devices	$\mu_0/\text{cm}^2 \cdot \text{V}^{-1} \cdot \text{s}^{-1}$	$\beta/(\text{cm} \cdot \text{V}^{-1})^{1/2}$
D1	0.094	0.0022
D2	0.266	0.001

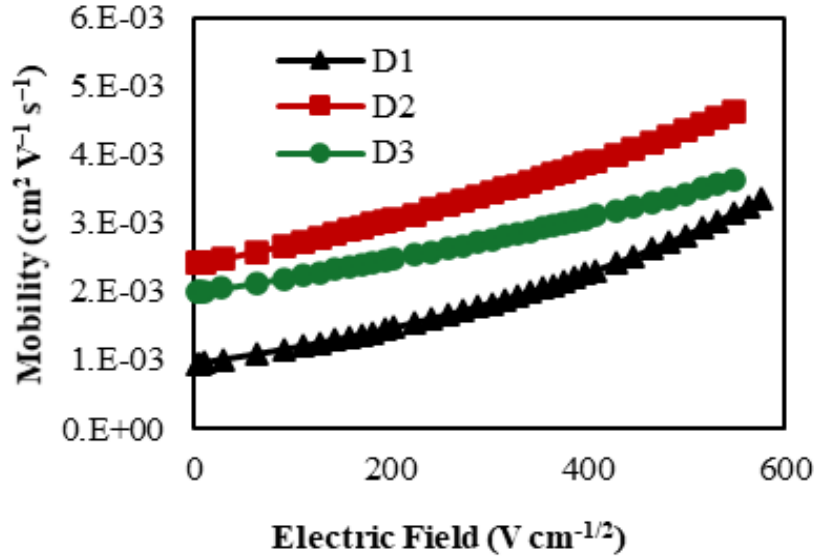


Fig.9 Mobility-square root of electric field for devices D1, D2 and D3.

To explore the reasons for the difference in charge balance of these devices, we fabricated the hole only devices (HODs) D1-D3 of ITO/BPBPA:3%HATCN (10 nm)/EBL (120 nm)/Liq (1 nm)/Ag (80 nm), respectively, to compare the charge transport properties of **SF2AF**, **BFS2A** and **BFS3A**. The carrier mobility of electric field dependence, $\mu(E)$, was obtained from the following semi-empirical SCLC equation of the mobility field dependence : $\ln(J/E^2) = \ln[9/8 (\epsilon_r \epsilon_0 \mu_0)/L] + \beta E^{1/2}$, where J is the density of current, L is the thickness of the film, and E is the electric field, the slope and the y-intercept give the Poole Frenkel factor β and the zero-field mobility μ_0 , respectively.⁽³²⁾ The relative dielectric constant ϵ_r is assumed to be 3 and the permittivity of the free space ϵ_0 is 8.85×10^{-12} F·m⁻¹. Carrier mobility depending on electric field of devices was plotted as shown in Fig.8, based on Poole Frenkel equation, $\mu(E) = \mu_0 \exp(\beta E^{1/2})$. All performances of various hole transport materials are summarized in the Table 3. For an electric field at 0.3 MV/cm, the estimated electron mobilities of devices D1, D2 and D3 were ~ 0.0018 , ~ 0.0034 and

$\sim 0.0028 \text{ cm}^2 \cdot \text{V}^{-1} \cdot \text{s}^{-1}$, respectively. Considering that only the electron-blocking materials are different, the difference in mobility of the devices can be attributed to the differences in hole mobilities of the electron-blocking materials. It can be *inferred* that the hole mobility order of these three electrons blocking materials is **BFS3A** > **BFS2A** > **SF2AF**, and the higher hole mobility of electron-blocking materials will result in less accumulation of holes between EBL and EML, thus contributing to a broaden recombination zone in the EML.⁽⁶⁾

Table 4 Key characteristics of devices a-b with different EBLs and thicknesses

Device	EBL Thickness (nm)	Voltage	CE (cd · A ⁻¹)	Luminance (cd · m ⁻²)	CIE x	CIE y	LT90 (h)
a1	SF4AF (10)	4.25	9.40	940	0.129	0.15331	649
a2	SF2DDA (10)	3.92	9.50	919	0.129	0.1433	511
a3	SF4DDA (10)	4.09	9.80	980	0.127	0.1511	616
b1	SF4AF (20)	4.41	9.35	935	0.129	0.1511	429
b2	SF2DDA (20)	3.96	9.81	981	0.130	0.1428	430
b3	SF4DDA (20)	4.28	10.00	1000	0.128	0.1479	422

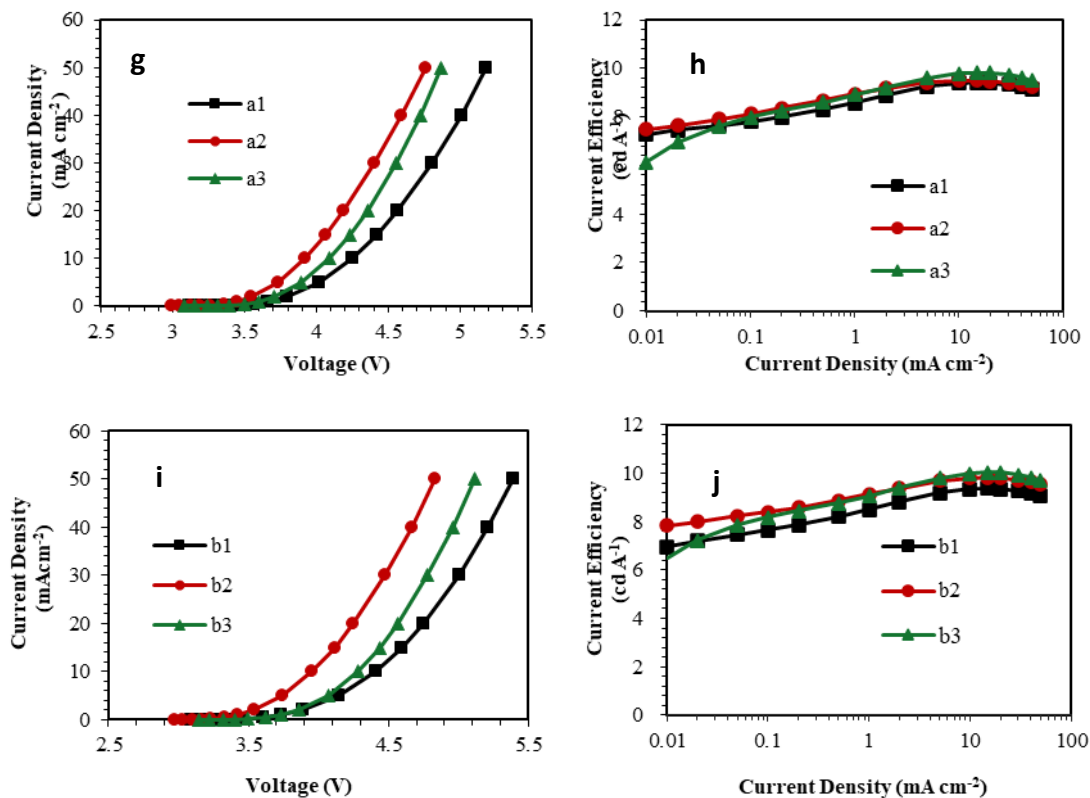


Fig.10 Electrical characteristics of the fabricated devices a-b with **SF4AF**, **SF2DDA** and **SF4DDA**

The current density–voltage (J–V) and current efficiency (CE) characteristics of the fabricated devices a-b with **SF4AF**, **SF2DDA** and **SF4DDA** are shown in Fig.10 and EL data are summarized in Table.4. Fig.10g shows that the voltage values of devices a1–a3 with **SF4AF**, **SF2DDA** and **SF4DDA** of 10 nm were 4.25V, 3.92V and 4.09 V at 10 mA·cm⁻², which verified that a larger HOMO energy level is beneficial to lower hole injection barrier from HTL to EBL, thus decreasing the voltage of the device. The voltage of device a3 was lower than that of device a1, which was attributed to the better hole transport performance of **SF4DDA** than that of **SF4AF**. As shown in Fig.10h, the CE of device a2 was almost the same as that of device a1, but the CE of device a3 was higher than that of device a1, which may be due to the improved carrier balance.

We also fabricated and tested devices b1-b3 with **SF4AF**, **SF2DDA** and **SF4DDA** of 20 nm, keeping the total thickness of the hole transport region unchanged, respectively, to explore the impact of the thickness of EBL on the

carrier balance of the device. Fig.10i shows that the increased thickness of EBL resulted in obvious increase of voltage. As shown in Fig.10j, the CE of device a1 hardly changed, but the CEs of device b2 and b3 significantly increased. These results indicated that devices b2 and b3 had better carrier balance than device b1, thus revealing that **SF2DDA** and **SF4DDA** have better hole transport mobilities than **SF4AF**.

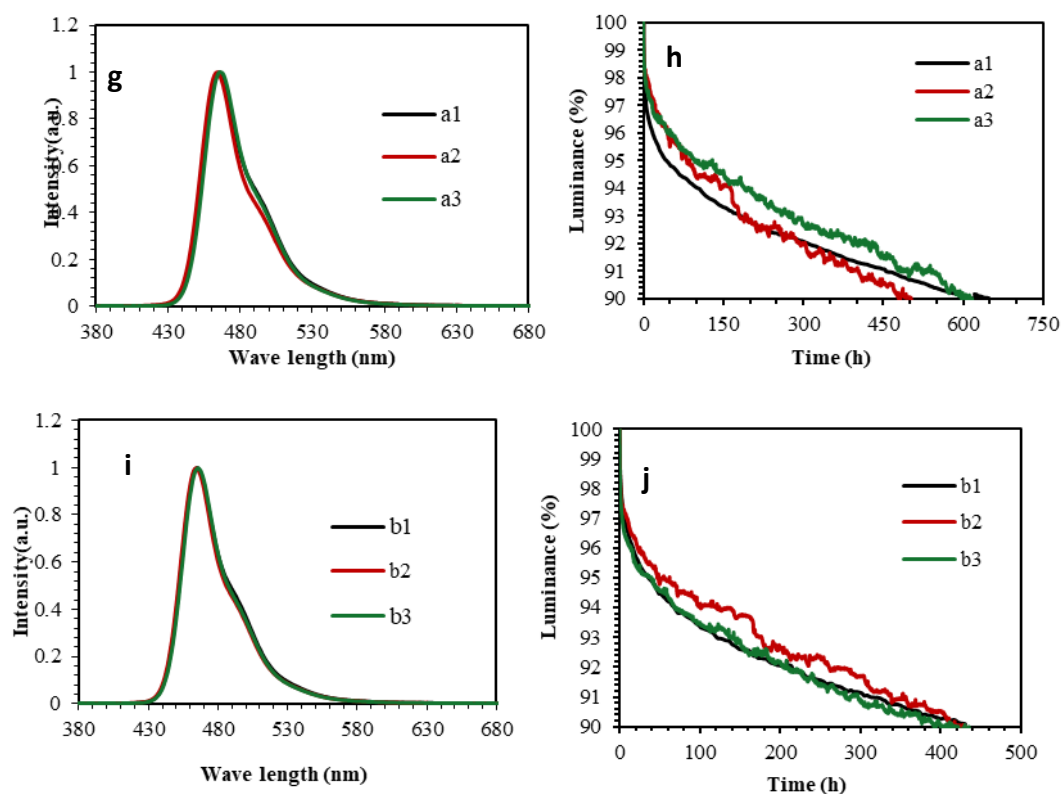


Fig.11 The normalized EL spectra (g, i) of the devices and device lifetime (h, j) at $10 \text{ mA} \cdot \text{cm}^{-2}$

As shown in Fig.11(g, i), no detectable exciplex emission at long wavelengths is observed and the pure blue emission from the EL spectra of all devices is attributed to the emission of BD, which indicates that **SF2DDA** and **SF4DDA** have good hole mobility and can effectively transport holes into the emitting layer. The LT90 of the devices a1–a3 were 649, 511 and 616 h, respectively, a longer lifetime is usually related to a better charge balance. Device a2 had a lower voltage and a higher current efficiency, but its lifetime was shorter than that of device a1, which may be due to the instability of the thin film of **SF2DDA** near the exciton recombination area.⁽²⁹⁾ When the

thickness of EBL was increased from 10 nm to 20 nm, the LT90 of the devices b1–b3 was all significantly decreased and almost the same, which indicated that the stability of the thin film of **SF2DDA** near the exciton recombination area was improved with the increasing thickness of EBL.

IV. Chapter summary

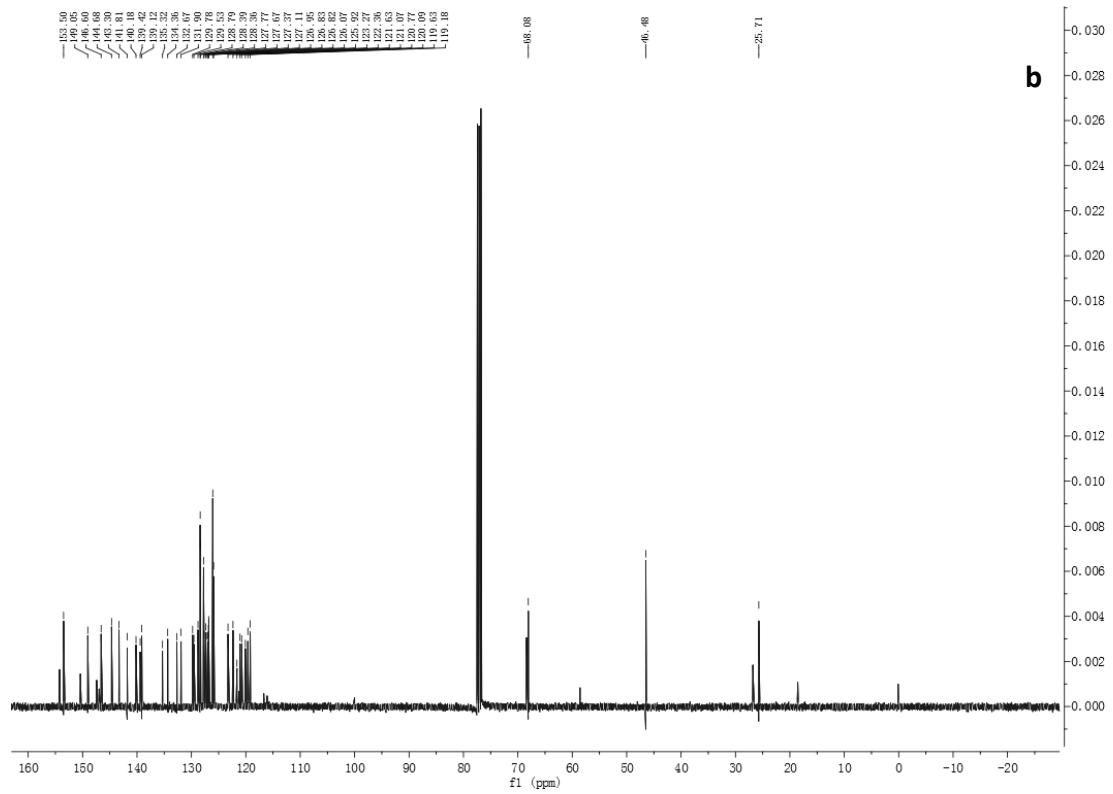
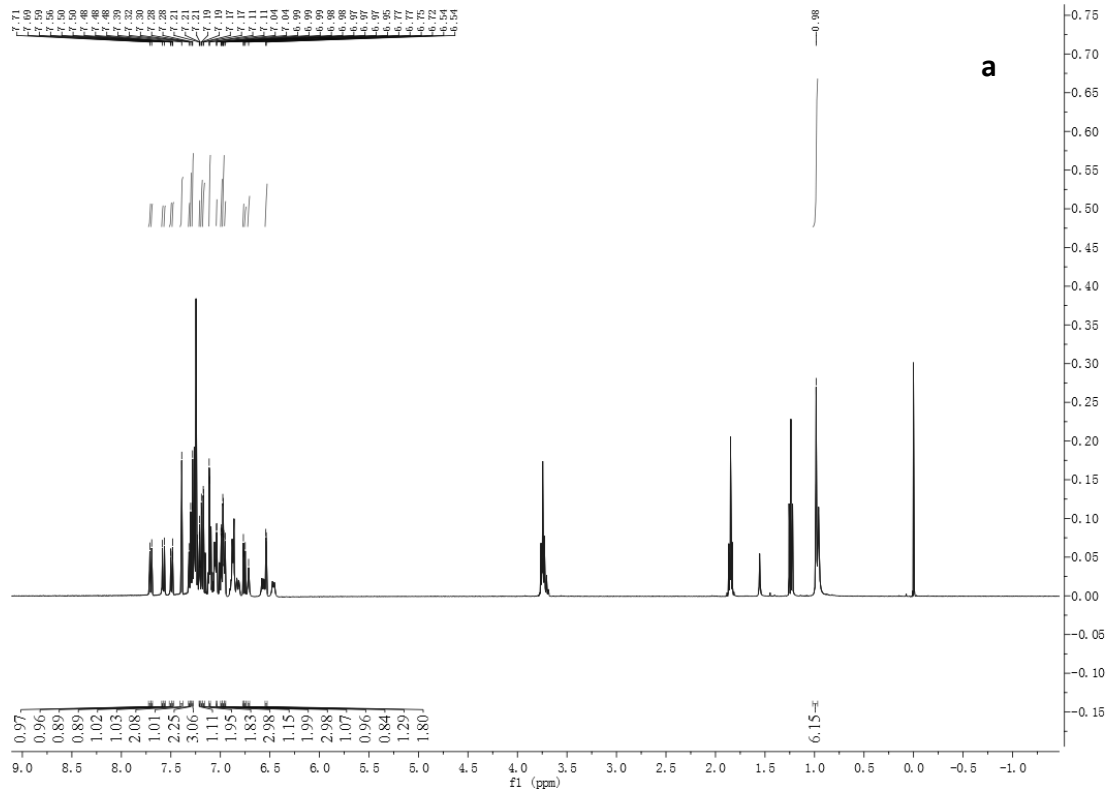
In summary, we designed and synthesized two series of spiro backbone-based electron-blocking materials (**BFS2A** and **BFS3A**, **SF2DDA** and **SF4DDA**), which have good electrochemical and thermal stability. Compared with traditional electron-blocking materials, devices with these materials showed the more excellent device performance, which was attributed to the suitable HOMO level and good hole transport performance of these electron-blocking materials. Because these electron-blocking materials all have the spiro backbone, it was inferred that the spiro backbone can improve the EL performances of the structures. These findings may assist the design of high EQE and long-lifetime EBL materials with simple structures for OLED applications, especially blue OLEDs.

Chapter 2 References

- (1) Jhulki, S. , Moorthy, J. N, *Appl. Phys. Lett.* 31, 8280-8325 (2018).
- (2) J. S. Bangsund, K. W. Hershey, R. J. Holmes, *ACS Appl. Mater. Interfaces.* 10, 5693(2018).
- (3) Y. Zhang, J. Lee, S. R. Forrest, *Nat. Commun.* 5, 5008 (2014).
- (4) S. Scholz, D. Kondakov, B. Lüssem, K. Leo, *Chem. Rev.* 115, 8449 (2015)
- (5) C. Adachi, K. Nagai, N. Tamoto, *Appl. Phys. Lett.* 66, 2679 (1995).
- (6) J.-M. Kim, C.-H. Lee, J.-J. Kim, *Appl. Phys. Lett.* 111, 203301 (2017).
- (7) D. P.-K. Tsang, T. Matsushima, C. Adachi, *Sci. Rep.* 6, 22463 (2016).
- (8) W. Song, J. Y. Lee, *Adv. Opt. Mater.* 5, 1600901 (2017).
- (9)R. Braveenth, H. W. Bae, Q. P. B. Nguyen, H. M. Ko, C. H. Lee, H. J. Kim, J. H. Kwon, K. Y. Chai, *Molecules.* 22, 464 (2017).
- (10) Y. J. Cho, J. Y. Lee, *Thin Solid Films.* 522, 415–419 (2012).
- (11) D. H. Huh; G. W. Kim; G. H. Kim; C. Kulshreshtha; J. H. Kwon, *Synth. Met.* 180, 79–84 (2013).
- (12) H. Aziz, Z. D. Popovic, *Chem. Mater.* 16, 4522 (2004).
- (13) S.-C. Dong, L. Xu, C. W. Tang, *Org. Electron.* 42, 379-386 (2017).
- (14)Y. Shirota, *Organic Electroluminescence*, ed. Z. H. Kafafi, Taylor & Francis, Washington, DC, 147 (2005).
- (15) Z. Zheng, Q. Dong, L. Gou, J.-H. Su, J. Huang, *J. Mater. Chem. C.* 2, 9858–9865 (2014).
- (16)U. Bach, K. D. Cloedt, H. Spreitzer and M. Gratzel, *Adv. Mater.* 12, 1060 (2000).
- (17)Y.-L. Liao, W.-Y. Hung, T.-H. Hou, C.-Y. Lin and K.-T. Wong, *Chem. Mater.* 19, 6350 (2007).
- (18) M. Mizusaki, M. Shibasaki, Y. Tsukamoto, T. Umeda, H. Tsuchiya, and S. Shimada, *J. Photopolym. Sci. Technol.* 33, 387-392 (2020).
- (19) S.-H. Jeong, K. H. Lee, J. Y. Lee, *Dye. Pigment.* 171, 107759 (2019).

- (20) T. Sato, T. Miyamae, H. Ohata, T. Tsutsui, *Org. Electron.* 74, 118-125 (2019).
- (21) S.-C. Dong, C.-H. Gao, X.-D. Yuan, L.-S. Cui, Z.-Q. Jiang, S.-T. Lee, L.-S. Liao, *Org. Electron.* 14, 902–908 (2013).
- (22) S.-H. Jeong, K. H. Lee, J. Y. Lee, *Dye. Pigment.* 171, 107759 (2019).
- (23) G. Haykir, M. Aydemir, S.H. Han, S. Gumus, G. Hizal, J.Y. Lee, F. Turksoy, *Org. Electron.* 59, 319-329(2018).
- (24) S. O. Jeon, J. Y. Lee, *J. Mater. Chem.* 22, 10537 (2012).
- (25) C. Adachi, T. Tsutsui, S. Saito, *Appl. Phys. Lett.* 57, 531(1990).
- (26) S. Jhulki, J. N. Moorthy, *J. Mater. Chem. C.* 6, 8280 (2018).
- (27) K. Haq, K. M A, X. Jiang, Z. Zhang, X. Zhang, L. Zhang and L. Jun, *J. Semicond.* 30, 114009 (2009).
- (28) J.-M. Kim, C.-H. Lee, J.-J. Kim, *Appl. Phys. Lett.* 111, 203301(2017).
- (29) C. Zhao, Lian Duan, *J. Mater. Chem. C.* 8, 803-820(2020).
- (30) S.-C. Dong, L. Xu b, C. W. Tang, *Org. Electron.* 42, 379-386(2017).
- (31) D. H. Huh, G. W. Kim, G. H. Kim, C. Kulshreshtha, J. Hyuk Kwon, *Synth. Met.* 180, 79–84(2013).
- (32) K. Haq, K. M A, X. Jiang, Z. Zhang, X. Zhang, L. Zhang and L. Jun, *J. Semicond.* 30, 114009(2009).

Appendix



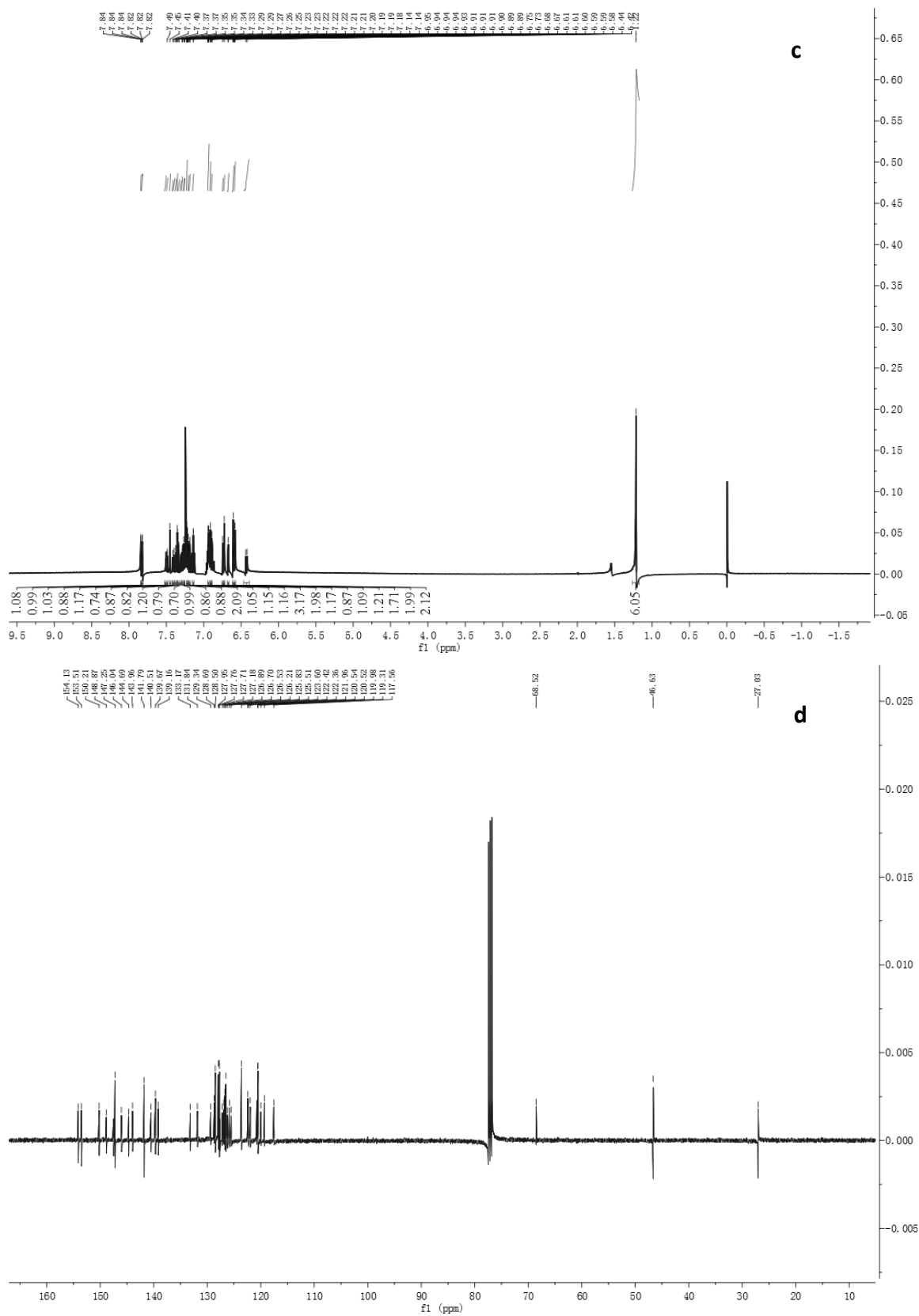


Fig.S1 ^1H spectroscopy of **BFS2A** (a), ^{13}C spectroscopy of **BFS2A** (b), ^1H spectroscopy of **BFS3A** (c) and ^{13}C spectroscopy of **BFS3A** (d).

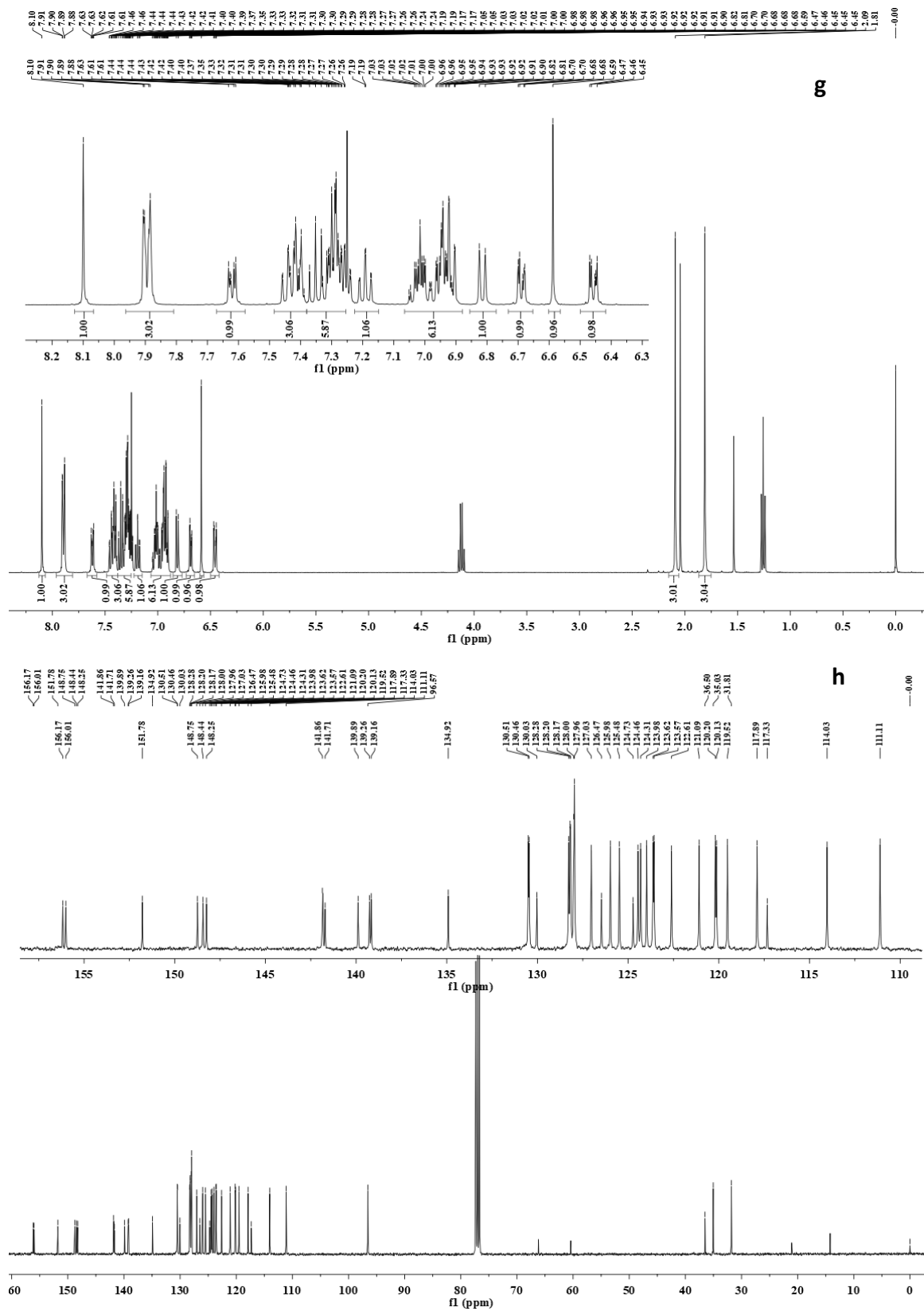
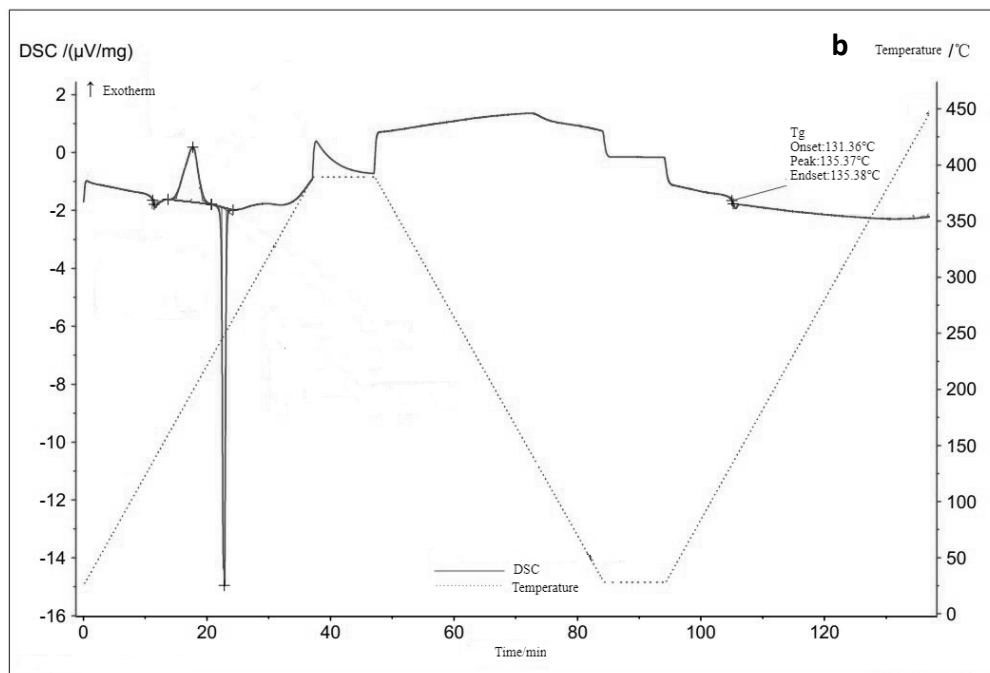
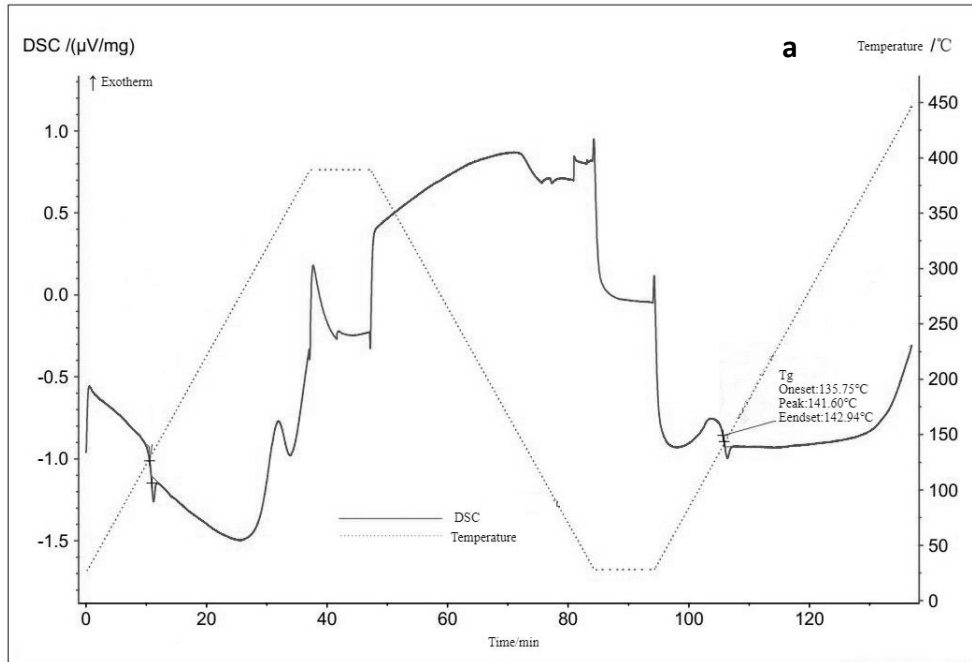


Fig.S2 ^1H spectroscopy of SF2DDA (e), ^{13}C spectroscopy of SF2DDA (f), ^1H spectroscopy of SF4DDA (g) and ^{13}C spectroscopy of SF4DDA (g).



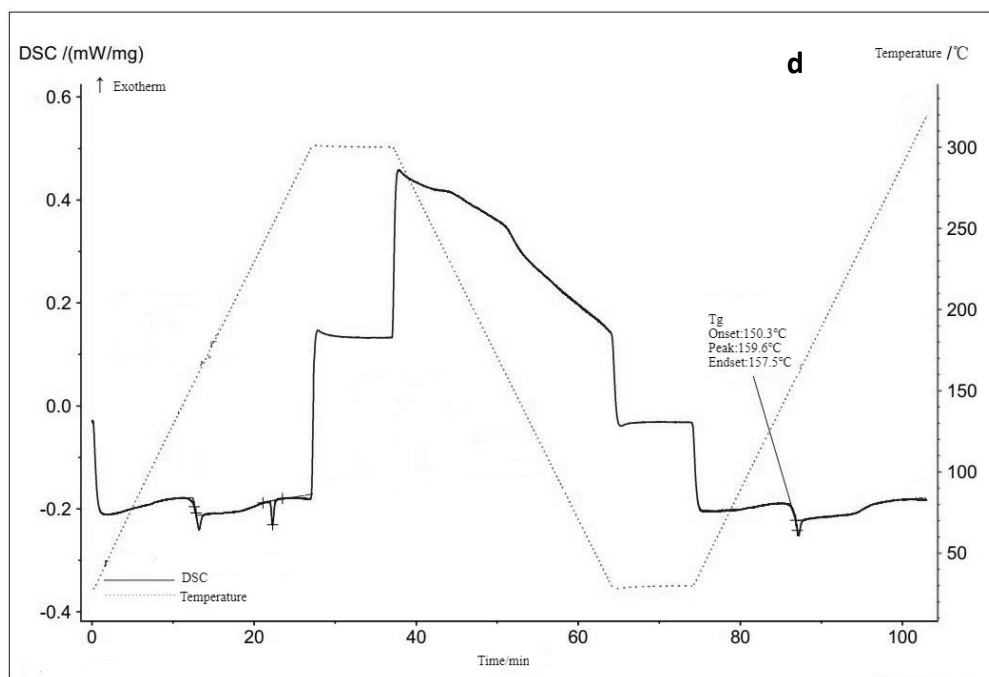
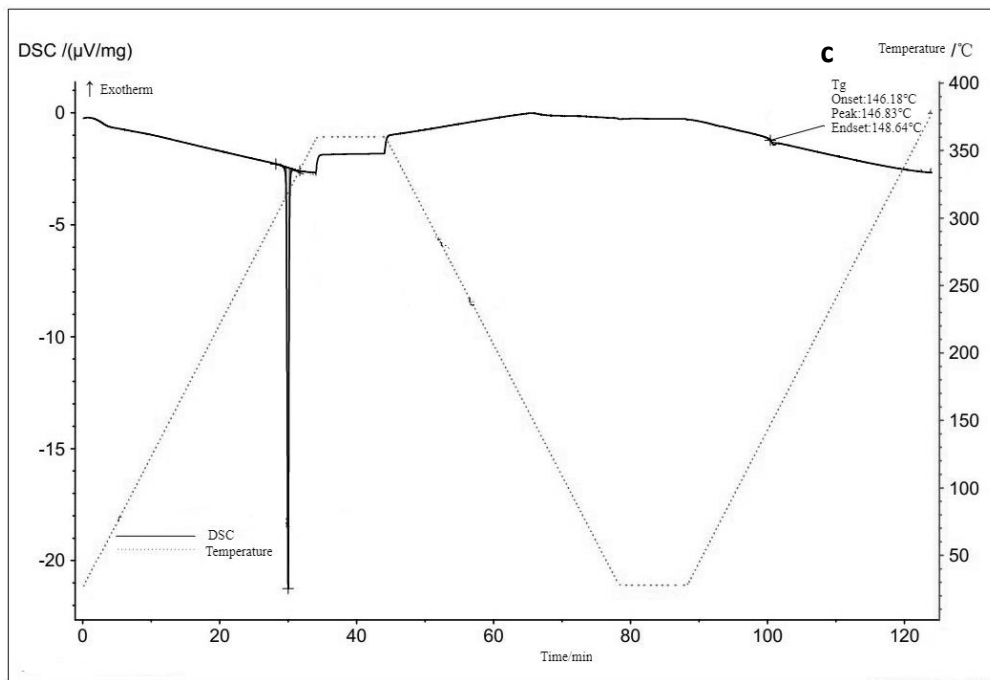


Fig.S3 DSC thermograms of **BFS2A(a)** ,**BFS3A(b)** ,**SF2DDA(c)** and **SF4DDA(d)**.

Chapter 3 Design and synthesis of new EB materials and its application in OLED devices

- I . Introduction
- II. Experiment content
 - II-1. Material structures and instrument
 - II-2. Synthesis and characterization
 - II-3. OLED fabrication and measurements
- III. Results and discussion
 - III-1. Theoretical calculations
 - III-2. Photophysical properties
 - III-3. Electrochemical properties
 - III-4. Thermal properties
 - III-5. Device application of newly designed EB materials
 - III-6. Charge transport in single carrier devices of newly designed EB materials
- IV. Chapter summary

I . Introduction

Full color organic light-emitting diodes (OLEDs) have received huge academic and industrial attention over the past thirty years because of their prospective applications in full-color, flexible displays and space illumination.⁽¹⁻⁵⁾ Among the three typical display colors, red and green emitters have been reported with high external quantum efficiencies (EQE) and long lifetimes, however the performance of blue emitters has been relatively poor.⁽⁶⁻⁸⁾ Blue phosphorescent or thermally-activated delayed fluorescent (TADF) OLEDs have therefore been studied to take the place of blue fluorescent OLEDs.⁽⁹⁾ However, the short operating lifetime of blue phosphorescent and TADF OLEDs limits their application.⁽¹⁰⁻¹¹⁾

The device lifetime of blue phosphorescent and TADF OLEDs needs to be dramatically improved. A recent report suggested that the EQE and lifetime of blue fluorescent OLEDs could be improved through clever molecular design and device fabrication.⁽¹²⁾ A major factor affecting the EQE and lifetime of OLEDs is holes and electrons leaking into the emission layer and thereby confining carriers within the emission layer. The two functions of the hole transport layer (HTL) are to transport holes and block electrons. Most HTL materials can not meet both these requirements, so an additional electron blocking layer (EBL) is incorporated to promote hole injection and limit electron leakage. The function of blocking electron flow is to transport holes while blocking misdirected electrons, which in turn improves the efficiency and luminance of the OLED device. EBL layers blocking electrons from entering the HTL were first reported by Adamovich et al. Blocked electrons cannot recombine with holes, so the luminous efficiency is improved.^(13,14) However, little effort has been paid to developing EBLs for blue fluorescent OLEDs, and design guidelines and specifications of EBLs for blue fluorescent OLEDs are lacking. Developing EBLs to increase the EQE and operating lifetime in blue fluorescent OLEDs is therefore necessary.^(15,16)

The normal amorphous EBL is 4,4',4"-tris(N-carbazolyl)-triphenylamine (**TCTA**). This compound has excellent hole transport and mobility properties and a high transition glass temperature (T_g).^(17,18) Holes are relatively difficult to inject into **TCTA** from N4,N4,N4',N4'-tetra([1,1'-biphenyl]-4-yl)

-[1,1'-biphenyl]-4,4'-diamine) (**TBPDIA**) because of the large highest occupied molecular orbital (HOMO) energy barrier (0.34 eV) between **TBPDIA** and **TCTA**.⁽¹⁹⁾

Here, three EBL materials were synthesized for use in blue fluorescent OLEDs. The molecular structures of the EBL materials were based on dimethyl-dihydroacridofuran. Specifically, 7-(5-(dibenzo [b,d] furan-4-yl)-[1,1'-biphenyl]-3-yl)-12,12-dimethyl-7,12-dihydrobenzofuro[3,2-b]acridine(**DFBDDbA**), 7-(3,5-bis(dibenzo[b,d]furan-4-yl)phenyl)-12,12-dimethyl-7,12-dihydrobenzofuro[3,2-b]acridine(**BDFPDDbA**) and 1,3-(3,5-bis(dibenzo[b,d]furan-4-yl)phenyl)-5,5-dimethyl-5,13-dihydrobenzofuro[3,2-c]acridine(**BDFPDDcA**) were synthesized. These three compounds have excellent hole transport performance, which allows more holes to be injected into the light-emitting layer. The light-emitting recombination area is far away from the interface between EBL and emitting layer, which effectively prevents the accumulation of excitons at the interface and improves the stability of the devices. Therefore, the devices exhibit long lifetime. The compounds can effectively block excitons and confine the triplet excitons in the light-emitting layer because of the high triplet energy level. Thus, the compounds improve the triplet-to-triplet up-conversion efficiency, and the devices can show higher EQE.⁽²⁰⁾ The performances of the devices were measured. Employing the EBLs based on the dimethyl-dihydroacridofuran derivatives increased the EQE of the blue fluorescent OLEDs from 6.11% to 7.12% and increased the lifetime by more than eight times the initial current density, compared to the device containing an EBL based on **TCTA**.⁽²¹⁾

II. Experiment content

II-1. Material structure and instrument

The functional materials used in the OLEDs are displayed in Fig.1, such as dipyrzino[2,3-f:20,3'-h]quinoxaline-2,3,6,7,10,11-hexacarbonitrile(**HATCN**), N₄,N₄,N₄',N₄'-tetra([1,1'-biphenyl]-4-yl)-[1,1'-biphenyl]-4,4'-diamine (**TBPDIA**), N-([1,1'-biphenyl]-4-yl)-N-(9,9-dimethyl-9H-fluoren-2-yl)-9,9'-spirobi[fluoren]-4-amine (**FSFA**), 9-(naphthalen-1-yl)-10-(naphthalen-2-yl)

anthracene (**BH**), N1,N6-bis (dibenzo[b,d]furan-4-yl) -3,8-diisopropyl-N1,N6-bis(4-isopropylphenyl)pyrene-1,6-diamine(**BD**),2-(4-(9,10-di(naphthalen-2-yl)anthracen-2-yl)phenyl)-1-phenyl-1H-benzo[d]imidazole (**NAPI**) and 8-hydroxyquinolinolato-lithium (**LiQ**) were obtained from commercial suppliers as described elsewhere.⁽²²⁾ Aluminum was used as a cathode without purification and was obtained from a commercial source. ¹H and ¹³C nuclear magnetic resonance (NMR) spectra were obtained using a 102 AVIII 400 MHz spectrometer (Bruker Scientific Technology Co., Ltd., Beijing, P. R. China). Liquid chromatography-mass spectra (LC-MS) were acquired using an Agilent 6460 LC-MS instrument. Elemental analysis for C, H and N was carried out using a Yanaco MT-5 CHN corder instrument. For photophysical characterization, 60-nm-thick films were deposited by thermal evaporation onto precleaned silica substrates. Ultraviolet-visible (UV-vis) absorption and photoluminescence (PL) spectra of the films were recorded using an HP-8453 UV-vis spectrophotometer (Agilent) and a Fluoromax-4 spectrophotometer (Horiba Scientific), respectively. Thermal analysis based on differential scanning calorimetry (DSC) was performed using a DSC-60 instrument under a nitrogen atmosphere with a heating rate of 10 °C/min. The HOMO energy was determined using a desktop ionization energy measurement system (Bunkoukeiki IPS-3). All materials produced for the OLED devices were purified by vacuum sublimation to >99.9% as determined by high performance liquid chromatography (HPLC).

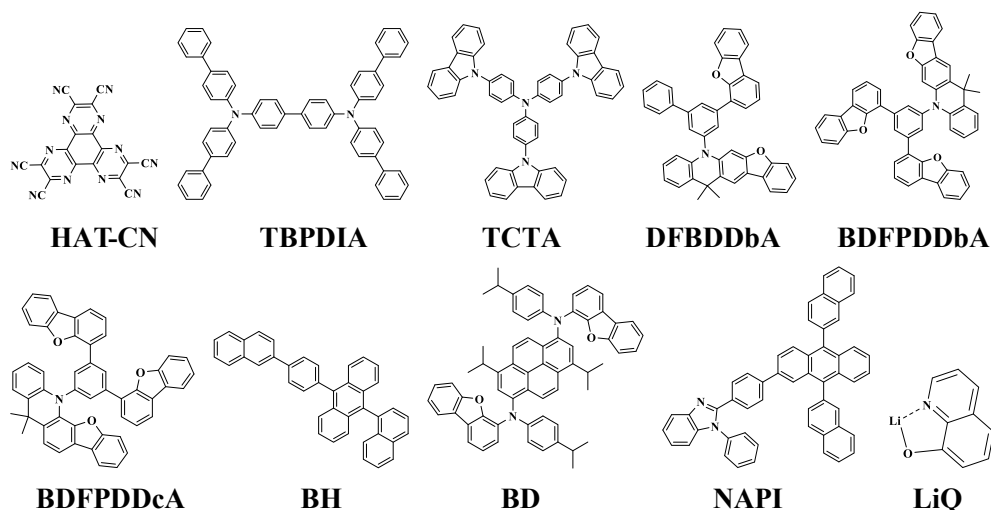
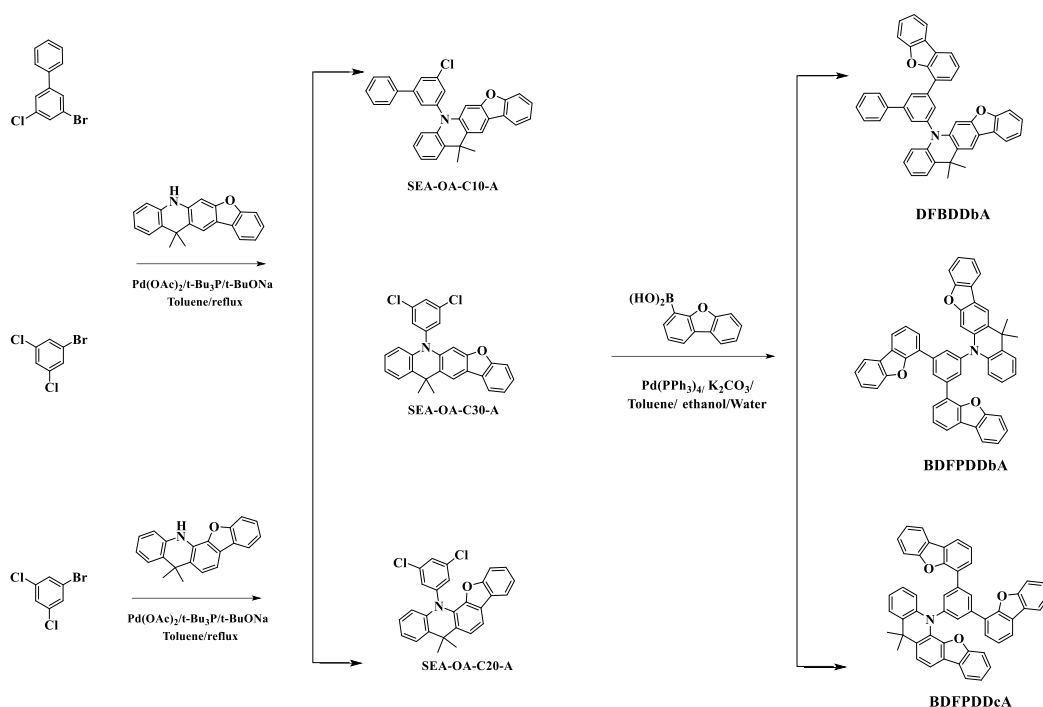


Fig.1 molecular structures of the materials used

II-2. Synthesis and characterization

The synthesis routes of **DFBDDbA**, **BDFPDDbA** and **BDFPDDcA** are shown in Scheme 1. The Suzuki-coupling reaction of the boronic ester of dibenzo [b,d]furan-4-ylboronic acid with 7-(5-chloro-[1,1'-biphenyl]-3-yl)-12,12-dimethyl-7,12-dihydrobenzofuro[3,2-b]acridine, 7-(3,5-dichlorophenyl)-12,12-dimethyl-7,12-dihydrobenzofuro[3,2-b]acridine and 13-(3,5-dichlorophenyl)-5,5-dimethyl-5,13-dihydrobenzofuro[3,2-c]acridine produced **DFBDDbA**, **BDFPDDbA** and **BDFPDDcA**, respectively. Characterization of the synthesized materials by ^1H and ^{13}C spectroscopy (Fig.S1-S3) and LC-MS confirmed their chemical structure.



Scheme 1 Synthesis of **DFBDDbA**, **BDFPDDbA** and **BDFPDDcA**

II-2-1. The synthesis of **DFBDDbA**:

12,12-dimethyl-7,12-dihydrobenzofuro[3,2-*b*]acridine (2.991 g, 0.01 mol) and 2-bromo-9,9'-spirobi[fluorene] (3.191g, 0.012mol) were dissolved in 150 ml anhydrous toluene in a round bottom flask under nitrogen atmosphere. *t*-BuONa (2.883 g, 0.03 mol), Pd(OAc)₂ (22.5 mg, 1×10⁻⁴ mol) and *t*-Bu₃P (1.0 M in toluene solution, 50 μL, 5×10⁻⁵ mol) were added to the solution. The reaction mixture was refluxed for 24 h at 105 °C. After cooling to room temperature, the mixture was filtered and the filtrate was evaporated under reduced pressure to remove solvent. The residue was purified by silica gel column chromatography to afford SEA-OA-C10-A (4.178 g, 86.1% yield).

SEA-OA-C10-A (4.851 g, 0.01 mol) and dibenzo[*b,d*]furan-4-ylboronic acid (2.545 g, 0.012 mol) were dissolved in the mixing solvent (30 ml toluene, 30 ml ethanol and 18 ml water) in a round bottom flask under nitrogen atmosphere. K₂CO₃ (2.764 g, 0.02 mol) and Pd(PPh₃)₄ (1.154 g, 0.001 mol) were added to the solution. The reaction mixture was refluxed for 24 h at 70 °C. After cooled to room temperature, water (20 mL) was added and stirred for several minutes. The organic layer was washed with water and brine, dried over anhydrous MgSO₄, filtered, and concentrated in vacuum. The residue was recrystallized in the methanol to provide off-white crude product, and subsequently it was

purified by silica gel column chromatography to afford pure white product (5.623 g, 91.1% yield). ^1H NMR (400 MHz, Chloroform-*d*) δ 8.37 (t, J = 1.6 Hz, 1H), 8.13 – 7.93 (m, 4H), 7.93 – 7.84 (m, 1H), 7.79 – 7.66 (m, 4H), 7.63 – 7.54 (m, 2H), 7.53 – 7.28 (m, 9H), 7.12 – 6.97 (m, 2H), 6.82 (s, 1H), 6.69 (dd, J = 8.1, 1.1 Hz, 1H), 1.83 (s, 6H). ^{13}C NMR (400 MHz, Chloroform-*d*) δ 156.22, 155.75, 144.74, 141.83, 140.97, 140.08, 139.83, 130.40, 130.32, 129.05, 128.98, 128.84, 127.95, 127.61, 127.37, 127.31, 126.84, 126.77, 126.56, 125.40, 124.92, 124.78, 124.77, 123.33, 122.90, 122.56, 121.12, 120.71, 120.37, 119.55, 117.21, 116.72, 114.64, 112.03, 111.16, 97.23, 36.58, 31.08. MS m/z (ESI) Calcd for $\text{C}_{45}\text{H}_{31}\text{NO}_2$: 617.24; Found: 618.32 $[\text{M}+\text{H}]^+$.

II-2-2. The synthesis of BDFPDDbA:

12,12-dimethyl-7,12-dihydrobenzofuro[3,2-*b*]acridine (2.991 g, 0.01 mol) and 1-bromo-3,5-dichlorobenzene (2.687 g, 0.012 mol) were dissolved in 150 ml anhydrous toluene in a round bottom flask under nitrogen atmosphere. *t*-BuONa (2.883 g, 0.03 mol), $\text{Pd}(\text{OAc})_2$ (22.5 mg, 1×10^{-4} mol) and *t*-Bu₃P (1.0 M in toluene solution, 50 μL , 5×10^{-5} mol) were added to the solution. The reaction mixture was refluxed for 24 h at 105 °C. After cooling to room temperature, the mixture was filtered and the filtrate was evaporated under reduced pressure to remove solvent. The residue was purified by silica gel column chromatography to afford SEA-OA-C30-A (4.143 g, 93.5% yield).

SEA-OA-C30-A (4.431 g, 0.01 mol) and dibenzo[*b,d*]furan-4-ylboronic acid (5.089 g, 0.024 mol) were dissolved in the mixing solvent (60 ml toluene, 60 ml ethanol and 36 ml water) in a round bottom flask under nitrogen atmosphere. K_2CO_3 (5.528 g, 0.04 mol) and $\text{Pd}(\text{PPh}_3)_4$ (2.309 g, 0.002 mol) were added to the solution. The reaction mixture was refluxed for 24 h at 70 °C. After cooled to room temperature, water (40 mL) was added and stirred for several minutes. The organic layer was washed with water and brine, dried over anhydrous MgSO_4 , filtered, and concentrated in vacuum. The residue was recrystallized in the methanol to provide off-white crude product, and subsequently it was purified by silica gel column chromatography to afford pure white product (6.252 g, 88.4% yield). ^1H NMR (400 MHz, Chloroform-*d*) δ 8.71 (t, J = 1.6 Hz, 1H), 8.07 – 8.03 (m, 3H), 8.02 – 7.95 (m, 4H), 7.94 – 7.86 (m, 1H), 7.78 (dd, J = 7.6, 1.2 Hz, 2H), 7.62 – 7.54 (m, 3H), 7.51 – 7.40 (m, 5H), 7.36 (td, J = 7.5, 1.0 Hz, 2H), 7.33 – 7.26 (m, 2H), 7.13 (ddd, J = 8.3, 7.2, 1.5 Hz, 1H), 7.04 (td,

$J = 7.5, 1.3$ Hz, 1H), 6.99 (s, 1H), 6.82 (dd, $J = 8.2, 1.2$ Hz, 1H), 1.85 (s, 6H). ^{13}C NMR (400 MHz, Chloroform- d) δ 156.21, 153.38, 139.74, 130.65, 129.22, 127.36, 126.89, 126.57, 125.39, 125.18, 124.82, 124.08, 122.88, 122.55, 121.17, 120.71, 120.35, 116.62, 114.87, 112.03, 111.17, 97.43, 36.62, 30.87. MS m/z (ESI) Calcd for $\text{C}_{51}\text{H}_{33}\text{NO}_3$: 707.25; Found: 708.19 $[\text{M}+\text{H}]^+$.

II-2-3. The synthesis of BDFPDDcA:

5,5-dimethyl-5,13-dihydrobenzofuro[3,2- c]acridine (2.991 g, 0.01 mol) and 1-bromo-3,5-dichlorobenzene (2.687 g, 0.012 mol) were dissolved in 150 ml anhydrous toluene in a round bottom flask under nitrogen atmosphere. t -BuONa (2.883 g, 0.03 mol), $\text{Pd}(\text{OAc})_2$ (22.5 mg, 1×10^{-4} mol) and t -Bu $_3\text{P}$ (1.0 M in toluene solution, 50 μL , 5×10^{-5} mol) were added to the solution. The reaction mixture was refluxed for 24 h at 105 $^\circ\text{C}$. After cooling to room temperature, the mixture was filtered and the filtrate was evaporated under reduced pressure to remove solvent. The residue was purified by silica gel column chromatography to afford SEA-OA-C20-A (4.059 g, 91.6% yield).

SEA-OA-C20-A (4.431 g, 0.01 mol) and dibenzo[b,d]furan-4-ylboronic acid (5.089 g, 0.024 mol) were dissolved in the mixing solvent (60 ml toluene, 60 ml ethanol and 36 ml water) in a round bottom flask under nitrogen atmosphere. K_2CO_3 (5.528 g, 0.04 mol) and $\text{Pd}(\text{PPh}_3)_4$ (2.309 g, 0.002 mol) were added to the solution. The reaction mixture was refluxed for 24 h at 70 $^\circ\text{C}$. After cooled to room temperature, water (40 mL) was added and stirred for several minutes. The organic layer was washed with water and brine, dried over anhydrous MgSO_4 , filtered, and concentrated in vacuum. The residue was recrystallized in the methanol to provide off-white crude product, and subsequently it was purified by silica gel column chromatography to afford pure white product (6.012 g, 85.0% yield). ^1H NMR (400 MHz, Chloroform- d) δ 8.56 (t, $J = 1.6$ Hz, 1H), 8.15 (d, $J = 1.6$ Hz, 2H), 8.01 – 7.92 (m, 4H), 7.92 – 7.84 (m, 1H), 7.75 (dd, $J = 7.6, 1.2$ Hz, 2H), 7.63 (d, $J = 8.1$ Hz, 1H), 7.57 – 7.50 (m, 2H), 7.45 – 7.30 (m, 9H), 7.24 – 7.21 (m, 3H), 7.19 (dd, $J = 8.2, 1.5$ Hz, 1H), 7.08 (td, $J = 7.7, 1.2$ Hz, 1H), 1.82 (s, 6H). ^{13}C NMR (400 MHz, Chloroform- d) δ 156.29, 153.60, 144.40, 141.46, 137.79, 128.56, 127.44, 127.32, 127.05, 126.63, 125.64, 125.15, 125.01, 124.24, 124.16, 123.34, 122.84, 122.44, 122.20, 120.76, 120.34, 120.04, 119.86, 117.28, 113.60, 111.97, 111.83, 37.17, 31.00. MS m/z (ESI) Calcd for $\text{C}_{51}\text{H}_{33}\text{NO}_3$: 707.25; Found: 708.04 $[\text{M}+\text{H}]^+$.

II-3. OLED fabrication and measurements

OLED devices were fabricated with the general architecture of indium tin oxide (ITO) (150 nm)/HATCN (10 nm)/TBPDI A (60 nm)/EBL(10 nm)/BH:BD (5wt.%) (25 nm)/NAPI:LiQ = 1:1 (35 nm)/Al (80 nm). The ionization potential of each functional layer was shown in Fig.2.

ITO-coated glass substrates (50 mm × 50 mm) were ultrasonically cleaned with detergent, deionized water and isopropyl alcohol in that order for 20 min each, and then dried in a vacuum oven at 250 °C for 30 min. The organic layers and metal cathode were deposited on the pre-cleaned ITO glass under a high vacuum atmosphere (1.0×10^{-6} torr). After thin film deposition, the devices were encapsulated in a nitrogen-purged glove box. Current density-voltage-current efficiency measurements were recorded using a Keithley 2400 source meter, and electroluminescence (EL) spectra were recorded using a Minolta CS-2000 spectroradiometer. The OLED lifetime was measured using an EAS-62C device (Japan SYSTEM Technology Co., Ltd.) with an ELaging lifetime measurement system. The operating lifetime (LT_{90}), which is defined as the time for the luminance to decrease to 90% of the initial luminance (L_0), of the OLEDs was measured by operating the devices under a constant current ($10 \text{ mA} \cdot \text{cm}^{-2}$) and constant temperature (25°C), while varying the initial luminance.

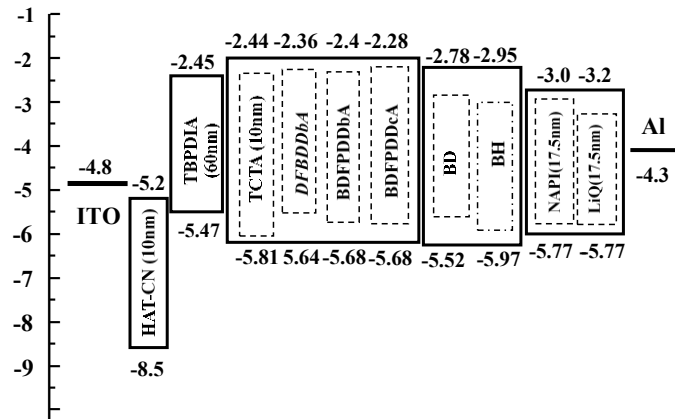


Fig.2 Energy level diagram of the OLEDs

III. Results and discussion

III-1. Theoretical calculation

Molecular calculations of **DFBDDbA**, **BDFPDDbA** and **BDFPDDcA** were carried out to determine the large HOMO and lowest unoccupied molecular orbital (LUMO), by density functional theory (DFT) with the B3LYP/6-31G (d) level of theory using the Gaussian 09 software package. Fig.3 shows that the HOMOs of these molecules are mainly distributed on the dimethyl-dihydroacridofuran unit, while the LUMOs are mainly located on the dibenzofuran and benzene groups. The HOMO mainly extends from the strong electron accepting character of the dimethyl dihydroacridine unit to the dibenzofuran unit, while the LUMO is observed only in the aromatic unit of the dibenzofuran. The distributions of the HOMOs and LUMOs in **DFBDDbA**, **BDFPDDbA** and **BDFPDDcA** are similar.⁽²³⁾

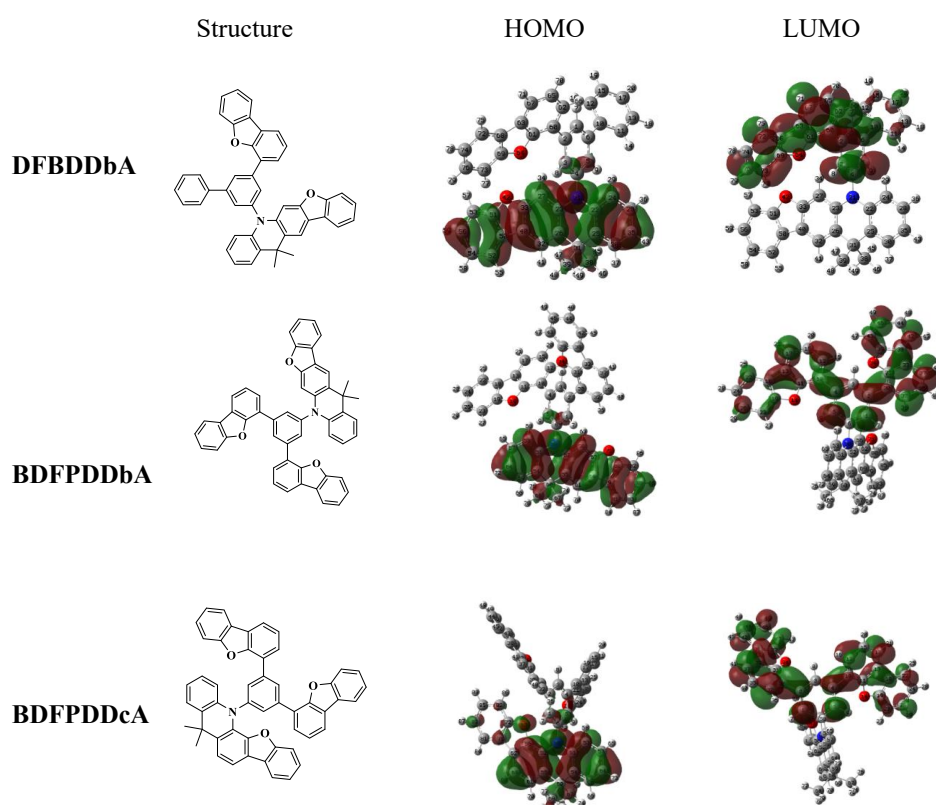


Fig.3 HOMO and LUMO of **DFBDDbA**, **BDFPDDbA** and **BDFPDDcA**

III-2. Photophysical properties

UV-vis and PL emission spectra of **DFBDDbA**, **BDFPDDbA** and

BDFPDDcA in the thin film state are shown in Fig.4. The optical band gaps (E_g) were estimated from the intersections of the absorption spectra according to $E_g^{\text{opt}} = 1240/\lambda_{\text{onset}}$. The E_g values of **DFBDDbA**, **BDFPDDbA** and **BDFPDDcA** were 3.28 eV, 3.28 eV and 3.40 eV, respectively. The triplet (T_1) energy level was calculated from the first triplet emission peak of the low temperature PL spectrum measured in liquid nitrogen (77 K). The T_1 energy levels of **DFBDDbA**, **BDFPDDbA** and **BDFPDDcA** were determined to be 2.78 eV, 2.79 eV and 2.89 eV, respectively, which were suitable for confining excitons in the emitting layer.⁽¹⁵⁾

The HOMO energy levels of **DFBDDbA**, **BDFPDDbA** and **BDFPDDcA** were measured using an ionization energy measurement system (Bunkoukeiki IPS-3), and were -5.64 eV, -5.68 eV and -5.69 eV, respectively (Table 1). According to $E_{\text{LUMO}} = E_{\text{HOMO}} + E_g$, the LUMO energy levels of **DFBDDbA**, **BDFPDDbA** and **BDFPDDcA** were -2.36 eV, -2.40 eV and -2.28 eV, respectively.

The HOMO levels of **BDFPDDbA** and **BDFPDDcA** were relatively deep compared to that of **DFBDDbA** because of the conjugated dibenzofuran group. The HOMO levels of **DFBDDbA**, **BDFPDDbA** and **BDFPDDcA** were between those of the **TBPDIAA** hole transport material (-5.48 eV) and the blue host (-5.97 eV) which was used for hole injection from **TBPDIAA** to **BD**. The LUMO level was relatively shallow compared to that of **BD** (-2.95 eV) which was necessary to prevent electron leakage. As a result, **DFBDDbA**, **BDFPDDbA** and **BDFPDDcA** had appropriate HOMO and LUMO energy levels for achieving hole injection and electron blocking.

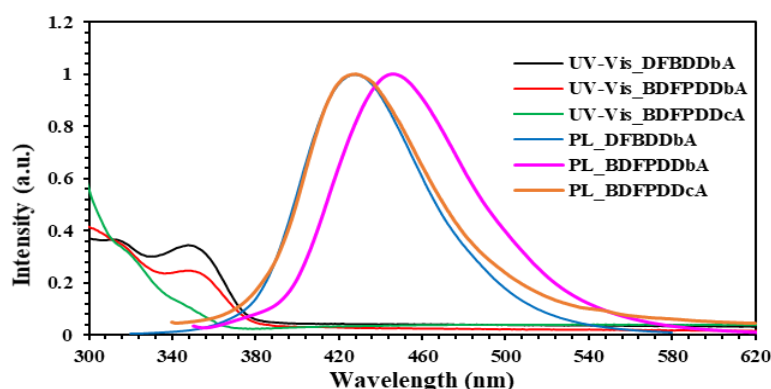


Fig.4 UV–visible absorption and photoluminescence emission spectra of **DFBDDbA**, **BDFPDDbA** and **BDFPDDcA**

III-3. Electrochemical properties

Cyclic voltammetry (CV) was used to evaluate the electrochemical properties of **DFBDDbA**, **BDFPDDbA**, **BDFPDDcA** and **TCTA** at room temperature. CV curves over 50 cycles for **DFBDDbA** and **BDFPDDbA** (Fig.5a–b) showed almost the same profiles, oxidation potentials and current values. In contrast, CV curves for **BDFPDDcA** and **TCTA** (Fig.5c–d) showed irreversible reduction and oxidation. The oxidation potential gradually moved to higher potential and the current increased with increasing scan number. These results demonstrated that **DFBDDbA** and **BDFPDDbA** had good structural stability for repetitive redox activity without decomposition. **DFBDDbA** and **BDFPDDbA** were stable in solution which is important for device performance.^(24,25)

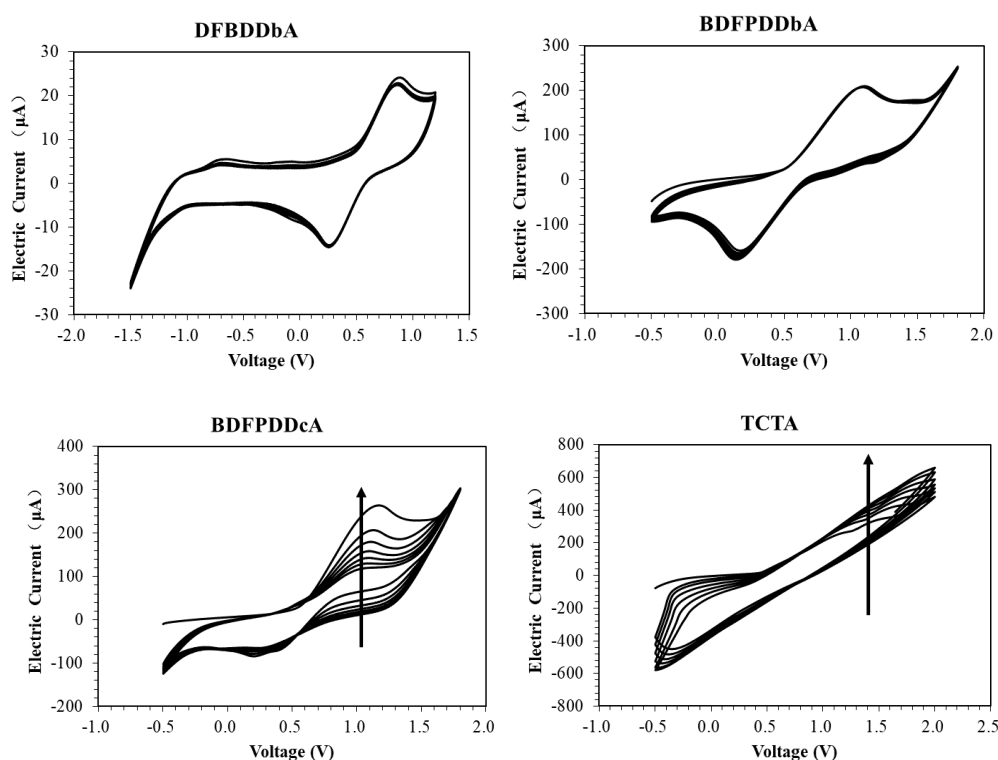


Fig.5 CV curves for (a) **DFBDDbA**, (b) **BDFPDDbA**, (c) **BDFPDDcA** and (d) **TCTA**

III-4. Thermal properties

Thermal stability is important for the stable operation of OLEDs. The T_g values of **DFBDDbA**, **BDFPDDbA** and **BDFPDDcA** were characterized by DSC. T_g values determined from the second heating scan were 124°C, 144°C

and 125°C for **DFBDDbA**, **BDFPDDbA** and **BDFPDDcA**, respectively. Film crystallization heat resistance experiments also suggested that **DFBDDbA**, **BDFPDDbA** and **BDFPDDcA** had good thermal stability (Fig.6). The high T_g indicated that common thermally-associated problems such as morphological stability and crystallization were unlikely to affect device operation. A material with a high T_g is less inclined to phase transition or deteriorate during device operation. These results showed that **DFBDDbA**, **BDFPDDbA** and **BDFPDDcA** possessed good thermal stability. In summary, **DFBDDbA**, **BDFPDDbA** and **BDFPDDcA** had high T_1 levels, good thermal stability and stability under vacuum evaporation, all of which are important for application in OLEDs. Physical data for **DFBDDbA**, **BDFPDDbA**, **BDFPDDcA** and **TCTA** are summarized in Table 1.

Table 1 Physical data for **DFBDDbA**, **BDFPDDbA**, and **BDFPDDcA**

Compound	$\lambda_{\max}^{\text{abs}}/n$ ^a	$\lambda_{\max}^{\text{em}}/n$ ^b	HOMO/eV	LUMO/eV	E_g /eV	ET	$T_g/^\circ\text{C}$
	m	m					
DFBDDbA	348	378	-5.64	-2.36	3.28	2.71	124
BDFPDDbA	347	378	-5.68	-2.40	3.28	2.71	144
BDFPDDcA	288	365	-5.69	-2.29	3.40	2.76	125
TCTA	330	367	-5.81	-2.44	3.37	/	/

a: Film UV

b: Excited at the absorption maxima.

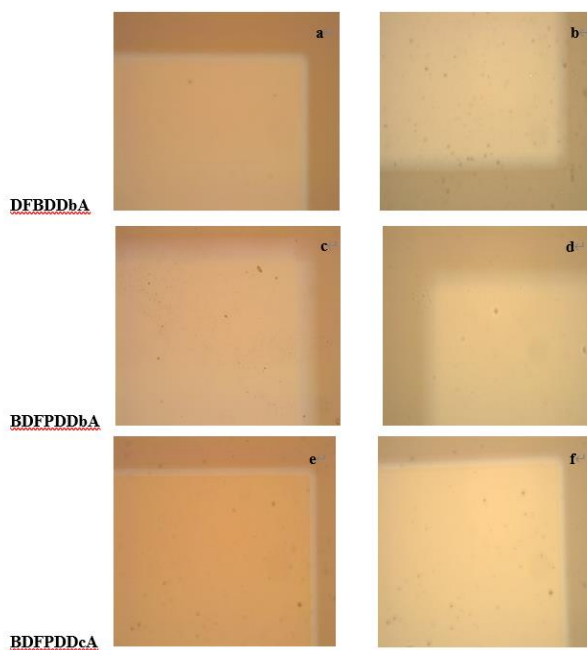


Fig.6 Surface morphology films of **DFBDDbA** as-deposited (a), annealed at 80°C after 11 days (b), Surface morphology films of **BDFPDDbA** as-deposited (c), annealed at 80°C after 11 days (d); Surface morphology films of **BDFPDDcA** as-deposited (e), annealed at 85°C (f) after 11 days

III-5. Device application of newly designed EB compounds

To investigate the EL performances of **DFBDDbA**, **BDFPDDbA** and **BDFPDDcA**, devices were prepared with the structure **ITO** (150 nm)/**HATCN** (10 nm)/**TBPDIAA** (60 nm)/electron-blocking material (10 nm)/**BD:BH** (5wt.%) (25 nm)/**NAPI:LiQ** (35 nm)/**Al** (80 nm), which utilized **HATCN** as a hole-injecting material, **TBPDIAA** as a hole-transporting material, **TCTA**, **DFBDDbA**, **BDFPDDbA** and **BDFPDDcA** as the electron-blocking materials, **BH** as the host material, **BD** as a dopant, **NAPI** as an electron-transporting material and **LiQ** as an electron-injecting material. Fig.2 shows the energy level diagram and chemical structures of the various device materials. Devices prepared using **TCTA**, **DFBDDbA**, **BDFPDDbA** and **BDFPDDcA** as the electron-blocking materials are referred to as device A, B, C and D, respectively. Current density-voltage-luminance (*J-V-L*) characteristics of devices A–D are shown in Fig.7 and EL data are summarized in Table 2.

Table 2 Electroluminescence properties of the devices

Device	EBL	Voltage ^a	CE ^a /CE _{max} ^b (Cd·A ⁻¹)	EQE ^c	CIE _x ^d	CIE _y ^d	EL _{peak} (nm)	LT ₉₀ ^a (h)
A	TCTA	4.42	9.33	6.11 %	0.1257	0.2262	469	34
B	DFBDDbA	4.28	8.52	7.15 %	0.1288	0.1581	466	277
C	BDFPDDbA	4.38	8.21	6.81 %	0.1330	0.1568	465	45
D	BDFPDDcA	4.62	8.62	6.85 %	0.1321	0.1604	465	8

^aRecorded at 10 mA·cm⁻²

^bMaximum current efficiency.

^cMaximum EQE

^dCommission Internationale de l'Eclairage (CIE) coordinates measured at 10 mA·cm⁻².

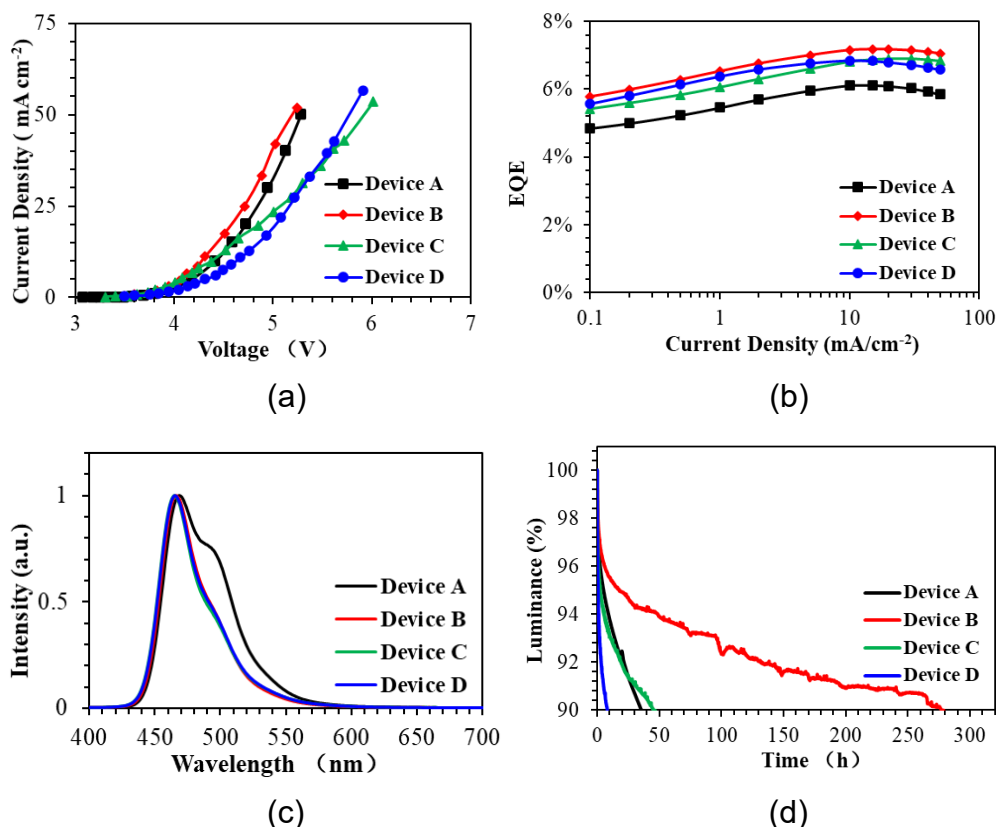


Fig.7 (a) *J-V* characteristics, (b) EQE, (c) normalized EL spectra and (d) lifetimes of devices A–D

Fig.7a shows that the minimum turn-on voltage of device B (based on **DFBDDbA**) at 10 mA·cm⁻² is 4.28 V among these devices, which may be due to the shallowest HOMO level of **DFBDDbA** among the four materials. The relatively shallow HOMO level may facilitate hole injection, which makes it easier for hole carriers to transfer into the emission layer. EQE – *J* curve of device A–D is shown in Fig.7b. The EQEs of device A–D at a current density of 10 mA·cm⁻² were 6.11%, 7.15%, 6.81% and 6.85%, respectively. The main role of the EBL was to improve hole injection through reasonable HOMO level matching, thus reducing hole accumulation at the interface and improving the carrier balance. The high stability and performance of the devices suggested that **DFBDDbA**, **BDFPDDbA** and **BDFPDDcA** are promising electron-blocking materials for OLEDs.^(26, 27) Fig.7c. shows EL spectra for devices A–D at 10 mA·cm⁻². The spectra for the **DFBDDbA**, **BDFPDDbA** and **BDFPDDcA**-based devices showed peaks at 466 nm (Commission Internationale de l’Eclairage (CIE) coordinates, 0.1288, 0.1581) with a full width at half maxima (FWHM) of

39 nm, 465 nm (CIE coordinates, 0.1330, 0.1568) with a FWHM of 37 nm and 466 nm (CIE coordinates, 0.1321, 0.1604) with a FWHM of 39 nm, respectively. These peaks were similar to those in the corresponding film PL spectra, which indicated that all emissions which originated from the emitting layer. The spectra for the **TCTA**-based device showed a peak at 469 nm (CIE coordinates, 0.1257, 0.2262) with a FWHM of 54 nm and another peak beyond 500 nm which originated from **BD** (Fig.S8).^(28, 29) Fig.S10. shows EL spectra for devices B–D at various driving voltages from 3.5 V to 7 V. The EL spectra don't change as the voltage increases. These results indicated that the **DFBDDbA**, **BDFPDDbA** and **BDFPDDcA**-based devices had excellent blue color purity and good spectral stability compared to the **TCTA**-based device (device A). Then, the stability of the electron-blocking materials was evaluated. The normalized luminance of devices A–D as a function of operating time at 10 mA·cm⁻² is shown in Fig.7d. The operating lifetimes (LT₉₀) of the **TCTA**, **DFBDDbA**, **BDFPDDbA** and **BDFPDDcA** devices were 34 h, 277 h, 45 h and 8 h, respectively. LT₉₀ for the **DFBDDbA**-based device was more than eight times that for the **TCTA**-based device, which was attributed to the high electrochemical stability of **DFBDDbA** and the well-matched HOMO level. Therefore, the high electrochemical stability of the electron-blocking materials significantly improved the device stability.⁽³⁰⁾

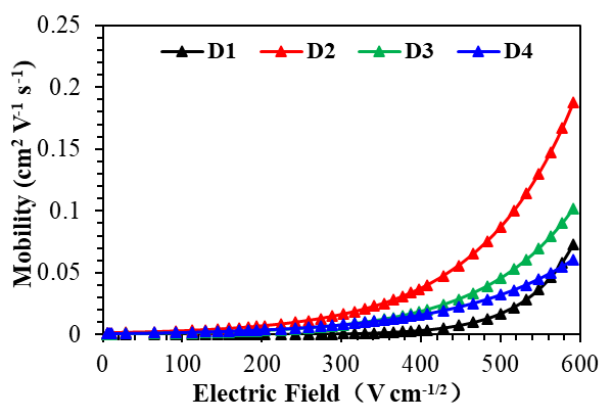


Fig.8 Mobility-square root of electric field for devices D1, D2, D3 and D4

Table 3 Calculated value of μ_0 and β

Devices	$\mu_0/\text{cm}^2 \cdot \text{V}^{-1} \cdot \text{s}^{-1}$	$\beta/(\text{cm} \cdot \text{V}^{-1})^{1/2}$
D1	0.0178	0.000006

D2	0.0084	0.001307
D3	0.0088	0.000560
D4	0.0069	0.001023

To explore the reasons for the difference in charge balance of these devices, we fabricated the hole only devices (HODs) of **TCTA**, **DFBDDbA**, **BDFPDDbA** and **BDFPDDcA** to compare their charge transport properties using the corresponding HODs of ITO/BPBPA:3%HATCN(10 nm)/EBL(120 nm)/Liq(1 nm)/Ag(80 nm) for devices D1, D2, D3 and D4, respectively. The carrier mobility of electric field dependence, μ (E), was obtained from the following semi-empirical SCLC equation of the mobility field dependence : $\ln(J/E^2) = \ln[9/8 (\epsilon_r \epsilon_0 \mu_0)/L] + \beta E^{1/2}$, where J is the density of current, L is the thickness of the film, and E is the electric field, the slope and the y-intercept give the Poole Frenkel factor β and the zero-field mobility μ_0 , respectively.⁽³¹⁾ The relative dielectric constant ϵ_r is assumed to be 3 and the permittivity of the free space ϵ_0 is $8.85 \times 10^{-12} \text{ F} \cdot \text{m}^{-1}$. Carrier mobility depending on electric field of devices was plotted as shown in Fig.8, based on Poole Frenkel equation, μ (E) = $\mu_0 \exp (\beta E^{1/2})$. All performances of various hole transport materials are summarized in the Table 3. For an electric field at 0.3 MV/cm, the estimated electron mobilities of devices D1, D2, D3 and D4 were ~ 0.00074 , ~ 0.01662 , ~ 0.00804 and $\sim 0.00828 \text{ cm}^2 \cdot \text{V}^{-1} \cdot \text{s}^{-1}$, respectively. Considering that only the electron-blocking materials are different, the difference in mobility of the devices can be attributed to the difference in hole mobilities of the electron-blocking materials. It can be inferred that the hole mobility order of EBLs is **DFBDDbA** > **BDFPDDcA** > **BDFPDDbA** > **TCTA**, and the higher hole mobility of electron-blocking materials will result in less accumulation of holes between the EBL/EML contributing to a broaden recombination zone in the EML.^(32, 33) The above results demonstrate that the high hole mobility can both improve the carrier balance of the devices and reduce the accumulation of excitons at the interface between EBL and EML, thus prolonging the operating

lifetime of the devices.

IV. Chapter summary

Three dimethyl-dihydroacridofuran derivatives were synthesized and applied as EBL materials for blue fluorescent OLEDs. The suitable HOMO level and high thermal stability of these EBL materials promoted hole injection, thereby improving the device performance. DFBDDbA was efficient as an EBL material, showing a high EQE of 7.15% and operating lifetime of 277 h at 10 mA·cm⁻², which was eight times that of the TCTA-based device. These findings may assist the design of high EQE and long-lifetime EBL materials with simple structures for OLED applications, especially blue OLEDs.

Chapter 3 References

- (1) C.W. Tang, S.A. Vanslyke, *Appl. Phys. Lett.* 51, 913-915 (1987).
- (2) M.A. Baldo, D.F.O. Brian, Y. You, A. Shoustikov, S. Sibley, M.E. Thompson, S.R. Forrest, *Nature*. 395, 151-154 (1998).
- (3) B.W. D'Andrade, W. Brian, M.A. Baldo, C. Adachi, J. Brooks, M.E. Thompson, S.R. Forrest, *Appl. Phys. Lett.* 79, 1045-1047 (2001).
- (4) S. Lamansky, P. Djurovich, J. Murphy, *J. Am. Chem. Soc.* 123, 4304-4312 (2001).
- (5) S. Tokito, T. Iijima, Y. Suzuri, H. Kita, T. Tsuzuki, F. Sato, *Appl. Phys. Lett.* 83, 569-571 (2003).
- (6) G.S. Samal, K.N.N. Unni, S. Bharat, S. Gupta, Deepak, *Org. Electron.* 10, 1201-1208 (2009).
- (7) H. Fukagawa, T. Shimizu, N. Ohbe, S. Tokito, K. Tokumaru, H. Fujikake, *Org. Electron.* 13, 1197-1203 (2012).
- (8) Q. Zhang, J. Li, K. Shizu, S. Huang, S. Hirata, H. Miyazaki, *J. Am. Chem. Soc.* 134, 14706-14709 (2012).
- (9) M. Kim, S.K. Jeon, S.H. Hwang, J.Y. Lee, *Adv. Mater.* 27, 2515-2520 (2015).
- (10) H. Uoyama, K. Goushi, K. Shizu, H. Nomura, C. Adachi, *Nature*. 492, 234-238 (2012).
- (11) T. Kim, K.H. Lee, J.Y. Lee, *J. Mater. Chem. C.* 6, 8472-8478 (2018).
- (12) D.Y. Kondakov, *Philos. Trans.: Math., Phys. Eng. Sci.* 373, 20140321 (2015).
- (13) V. Adamovich, J. Brooks, A. Tamayo, A. Alexander, P. Djurovich, B. D'Andrade, C. Adachi, S. Forrest, and M. Thompson, *New J. Chem.* 26, 1171 (2002).
- (14) V. Adamovich, S. Cordero, P. Djurovich, A. Tamayo, M. Thompson, B. D'Andrade, and S. Forrest, *Org. Electron.* 4, 77-87 (2003).
- (15) S.H. Jeong, K.H. Lee, J.Y. Lee, *J. Ind. and Eng.* 74, 71-78 (2019).
- (16) T. Kamata, H. Sasabe, M. Igarashi, J. Kido, *Chem. Eur. J.* 24, 4470-4470 (2018).
- (17) M. Hu, Y. Liu, Y. Chen, W. Song, L. Gao, H. Mu, *RSC Adv.* 7, 7287-7292 (2017).

- (18) F.R.P. Limberg, A. Miasojedovas, P. Pingel, F. Reisbeck, S. Janietz, A.P. Monkman, H. Kruger, *Rsc. Adv.* 5, 83122-83128 (2015).
- (19) S. Wu, M. Aonuma, Q. Zhang, S. Huang, T. Nakagawa, K. Kuwabara, *J. Mater. Chem. C.* 2, 421–424 (2013).
- (20) M. Mizusaki, M. Shibasaki, Y. Tsukamoto, T. Umeda, H. Tsuchiya, and S. Shimada, *J. Photopolym. Sci. Technol.* 33, 387-392 (2020).
- (21) D.H. Lee, Y.P. Liu, K.H. Lee, H. Chae, S.M. Cho, *Org. Electron.* 11, 427-433 (2010).
- (22) S.C. Dong, L. Xu, C.W. Tang, *Org. Electron.* 42, 379-386 (2017).
- (23) R. Braveenth, H.W. Bae, I.J. Ko, W. Qiong, Q.P. Nguyen, P. Jayashantha, J.H. Kwon, K.Y. Chai, *Org. Electron.* 51, 463-470 (2017).
- (24) N. Lin, J. Qiao, L. Duan, H. Li, L. Wang, Y. Qiu, *J. Phys. Chem. C.* 116, 19451-19457 (2012).
- (25) Q. Li, H. Liu, W. Sun, S. Wang, X. Dong, L. Wang, X. Li, *J. Mater. Ence.* 30, 11440-11450 (2019).
- (26) Y. Denis, Kondakov. *Philosophical Transactions of the Royal Society of London A: Mathematical, Physical and Engineering Sciences* .373, 1364 (2015).
- (27) S. Liu, X. Zhang, H. Feng, J. Zhang, L. Zhang, W. Xie, *Org. Electron.* 47, 181-188 (2017).
- (28) L. Li, B. Jiao, S. Li, L. Ma, Y. Yu, Z. Wu, *Opt. Mater.* 53, 19–23 (2016).
- (29) J. Huang, B. Xu, M. K. Lam, K.W. Cheah, C.H. Chen, J.H. Su, *Dyes Pigm.* 89, 155-161 (2011).
- (30) Y. Lv, P. Zhou, N. Wei, K. Peng, J. Yu, B. Wei, *Org. Electron.* 14, 124-130 (2013).
- (31) K. Haq, K. M A, X. Jiang, Z. Zhang, X. Zhang, L. Zhang and L. Jun, *J. Semicond.* 30, 114009 (2009).
- (32) J.M. Kim, C.H. Lee, J.J. Kim, *Appl. Phys. Lett.* 111, 203301 (2017).
- (33) T. Matsushima, F. Bencheikh, T. Komino, M.R. Leyden, A.S.D. Sandanayaka, C. Qin, C. Adachi, *Nature.* 572, 502-506 (2019).

Appendix

DFBDDbA

¹H-NMR

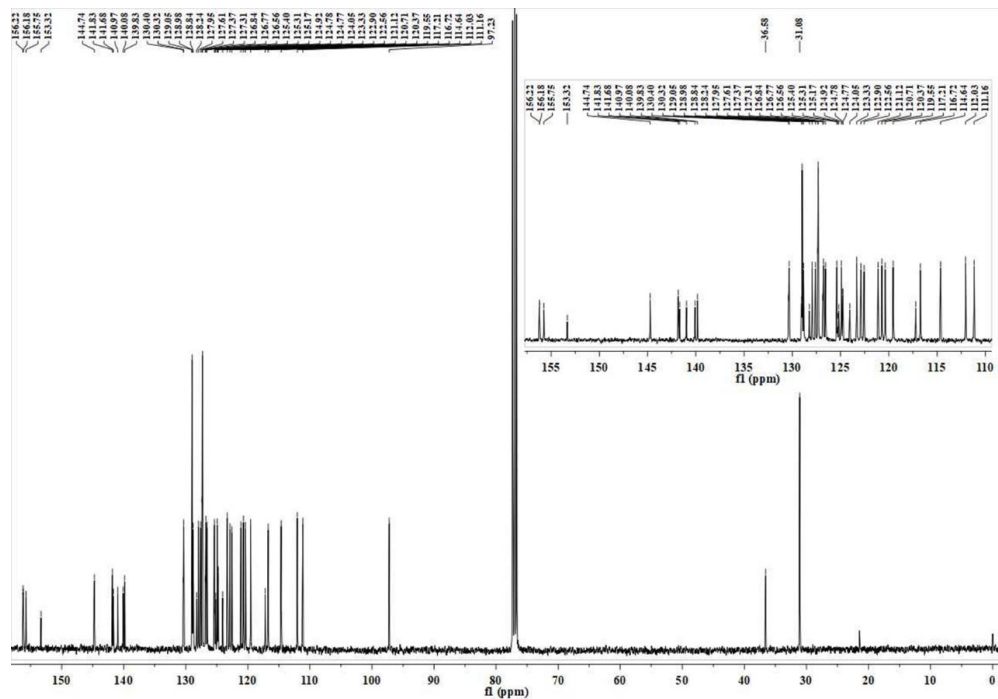
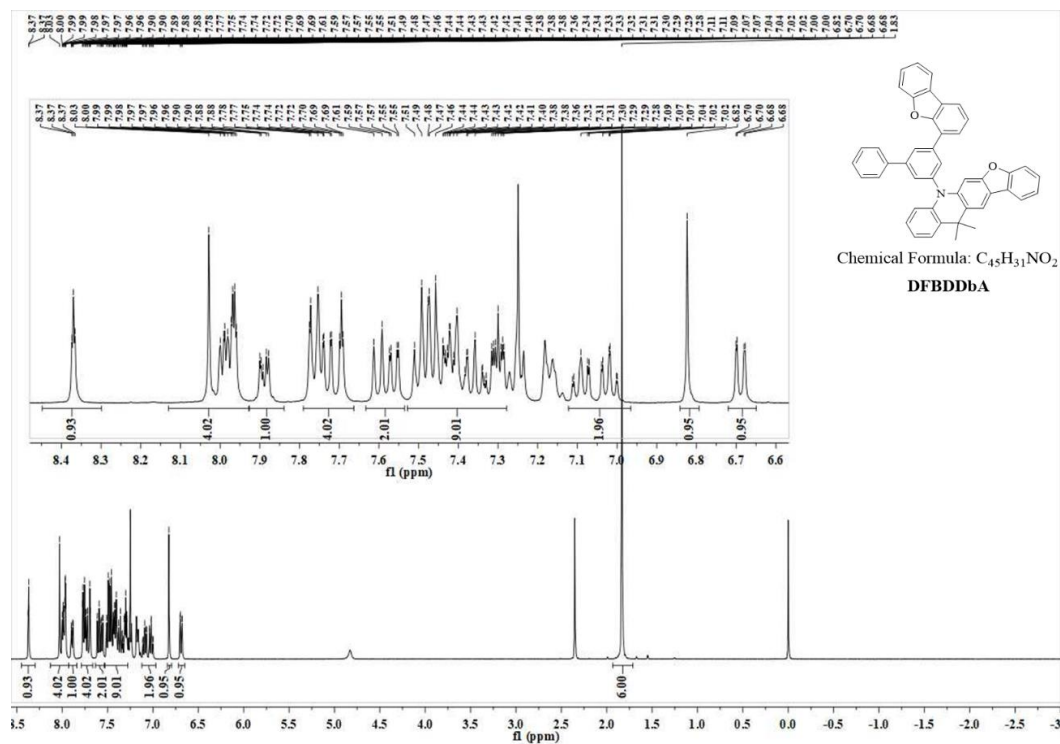
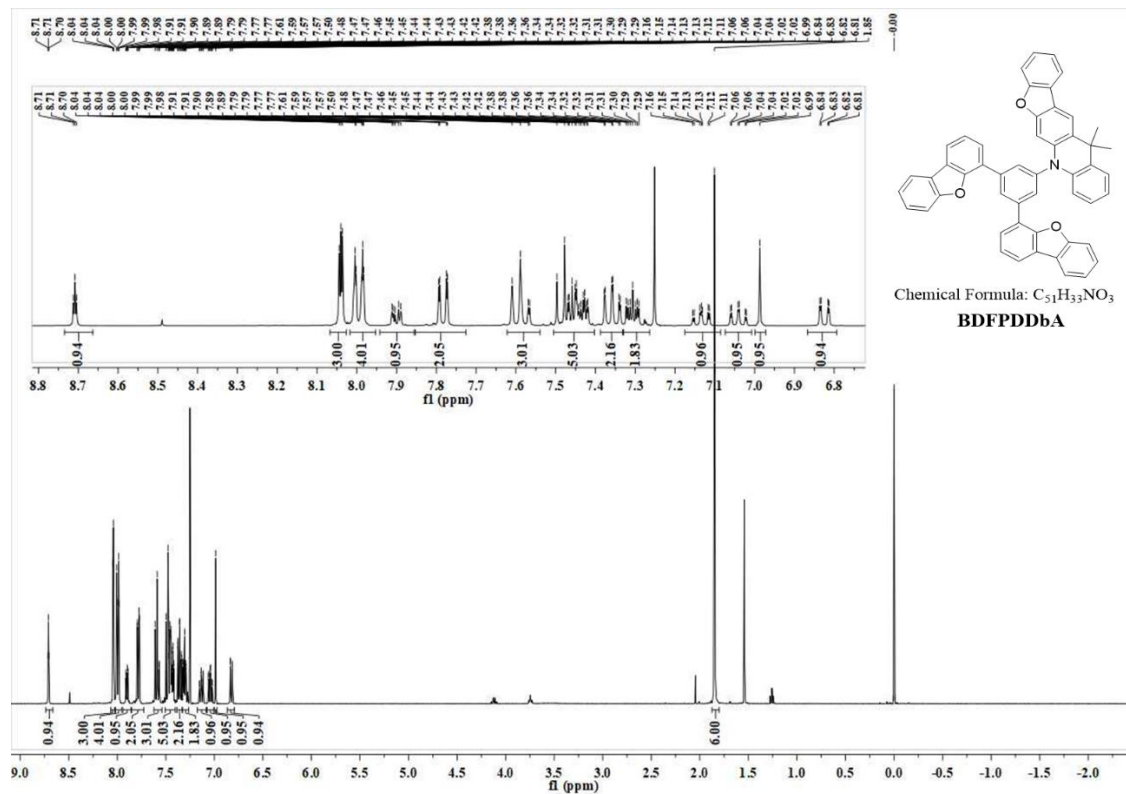


Fig.S1 ¹H NMR and ¹³C NMR spectrum of DFBDDbA

BDFPDDbA

¹H-NMR



¹³C-NMR

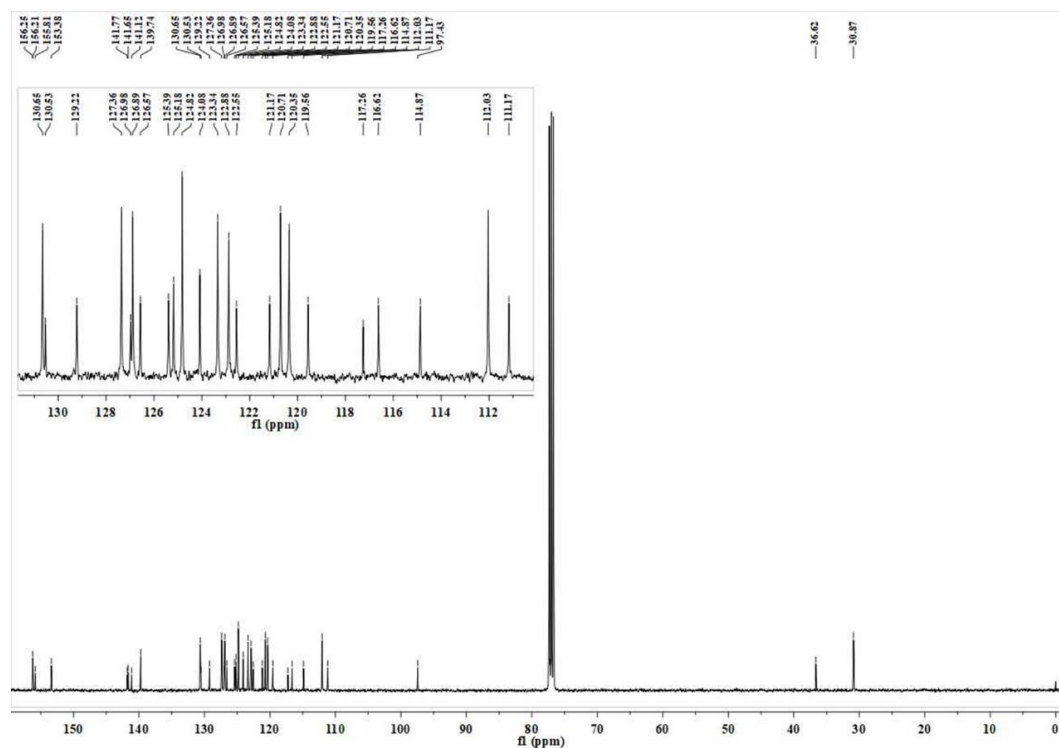
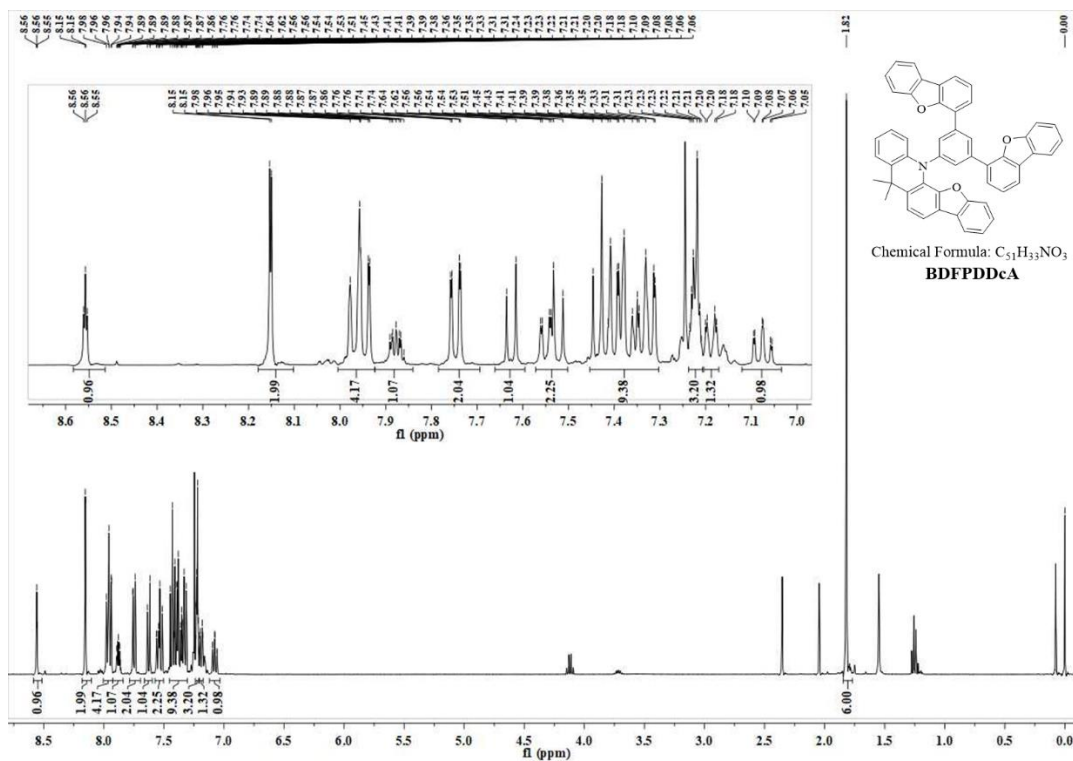


Fig.S2 ¹H NMR and ¹³C NMR spectrum of BDFPDDbA

BDFPDDcA

¹H-NMR



¹³C-NMR

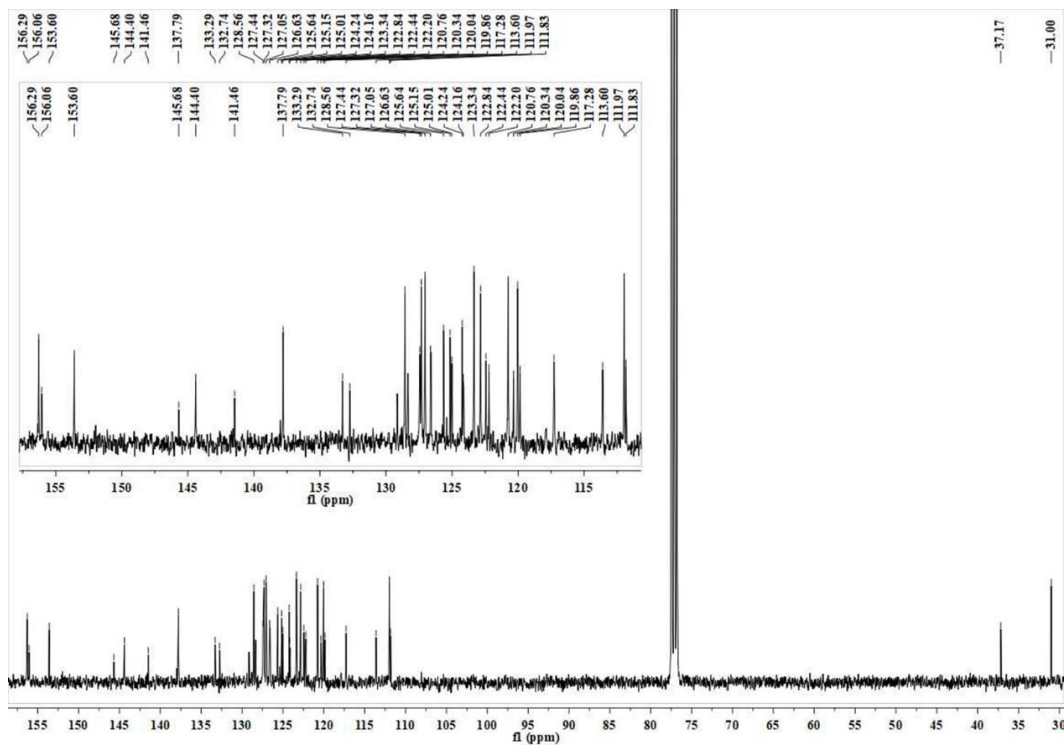
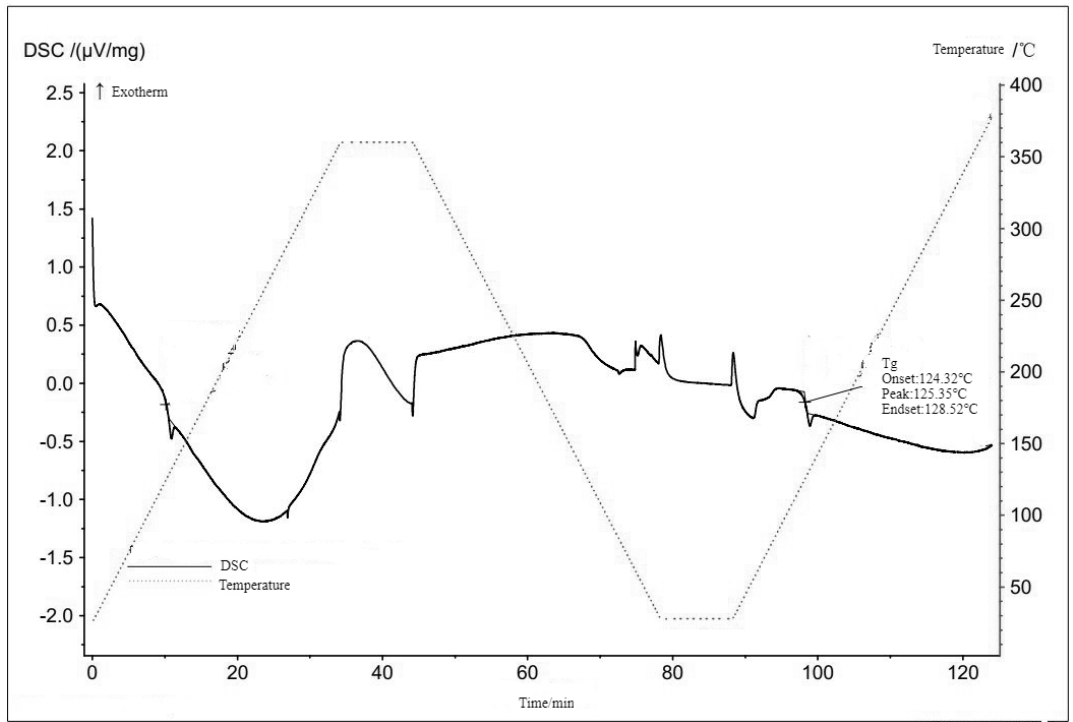
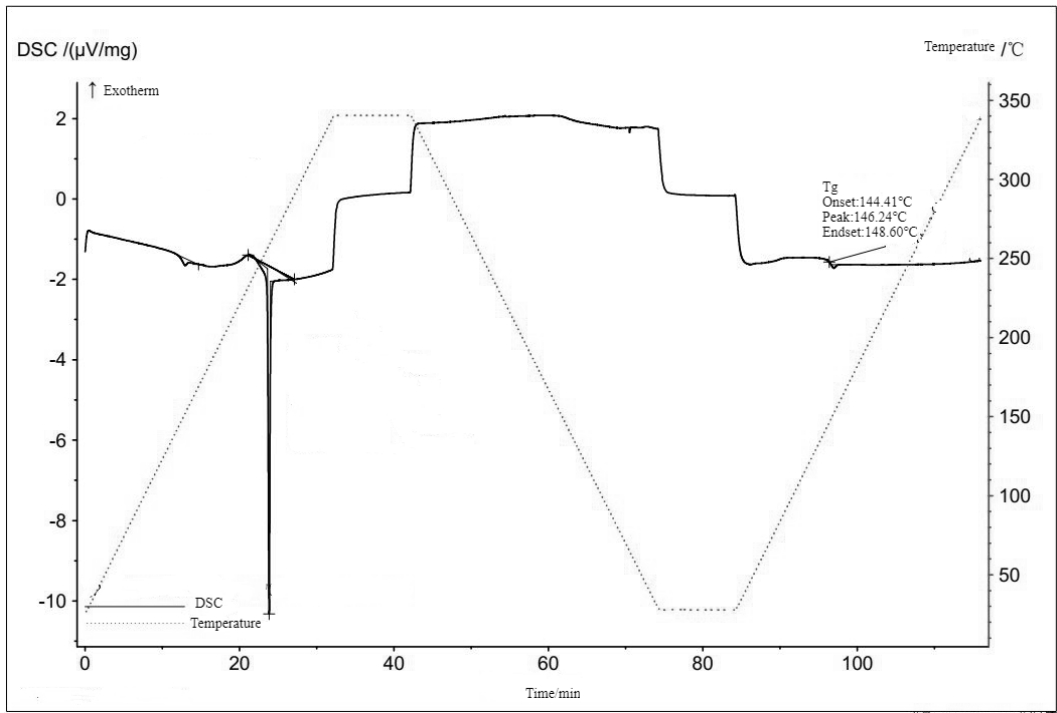


Fig.S3 ¹H NMR and ¹³C NMR spectrum of BDFPDDcA



(a)

)



(b)

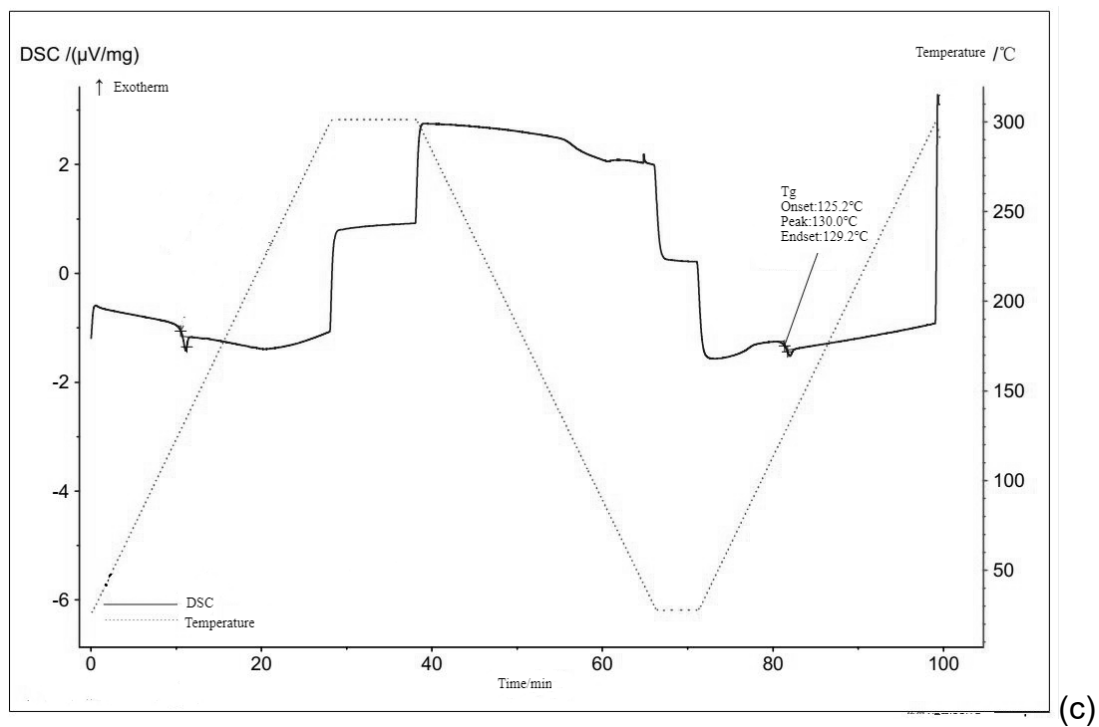


Fig.S4 DSC thermograms of **DFBDDbA(a)**, **BDFPDDbA(b)** and **BDFPDDcA(c)** under a nitrogen atmosphere at a heating rate of $10^{\circ}\text{C}/\text{min}$

Chapter 4 Synthesis and Properties of Diphenylamine/ Xanthone Hybrid Organic Light Emitting Materials

- I . Introduction
- II. Experiment content
 - II-1. General information
 - II-2. Synthesis and characterization
 - II-3. Fabrication of PHOLEDs
- III. Results and discussion
 - III-1. Theoretical calculation
 - III-2. Photophysical properties
 - III-3. Thermal analysis
 - III-4. Electroluminescent (EL) properties
 - III-5. Device optimization
- IV. Conclusion

I . Introduction

In recent years, a great progress has been made in the performance of organic light emitting diodes (OLEDs), making them practical applications in televisions, smart phone displays, and solid-state lighting.(1-6) The phosphorescent OLEDs, they can have excellent performance both in high efficiency and long lifetime, therefore, the red and green PHOLEDs have been commercialized.(7-12) Generally, the primary consideration for constructing high-performance PHOLEDs is the choice of host and guest materials.(13-22) Phosphorescent materials are typically doped into the host matrix at low concentrations in the emitting layer (EML) of the PHOLED because of triplet-triplet annihilation (TTA), triplet-polaron annihilation (TPA) and triplet-singlet annihilation (TSA) at high currents. In order to get further performance improvement of PHOLEDs, it is still a huge challenge to explore excellent host materials.(23-26) To achieve PHOLED devices with satisfactory performance, the host material's singlet and triplet excited state should be higher than that of the guest material, which is beneficial for the energy transfer process. In addition, the appropriate highest occupied/lowest unoccupied molecular orbital (HOMO/LUMO) energy levels are required to match adjacent layers, improving carrier injection balance and reducing device voltage.(27-31) In most instances, the HOMO/LUMO level of a single host is difficult to match with the adjacent layers on both sides to ensure carrier injection balance and achieve low voltage and high efficiency. In fact, PHOLEDs typically require double-host mixed evaporation approach to obtain much lower voltages and higher luminous efficiency. Therefore, the mutual cooperation of the hole-transport type or the electron-transport type host material can significantly improve the performance of the device.(32-34)

Xanthone is well known for its relatively short-lived (25 ms) phosphorescence lifetime and high triplet level(35-36), and its derivatives should be suitable for the host materials. However, the application of Xanthone as the host materials in OLED is extremely rare and mainly reported by the Adachi's research group. In 2014, Adachi et al. initially reported the 3-(9,9-dimethylacridin -10(9H)-yl)-9H-xanthen-9-one (ACRXTN) as the assistant dopant and 1,3-Bis(N-carbazolyl)benzene (mCP) as the host in the

fabrication of OLEDs, and a maximum EQE of 15.8% and a current efficiency of 45 cd·A⁻¹ were obtained respectively.(37) In 2017, the same group reported the three materials (o-CzXTN, m-CzXTN, and p-CzXTN), they are composed of xanthone (XTN) as an acceptor, 3,6-dimethylcarbazole (Cz) moieties as donors, and phenyl as a bridge unit.(38) OLEDs based on 10wt% o-CzXTN doped in bis(2-(diphenylphosphino)phenyl)ether oxide (DPEPO) as a host in the emitting layer (EML) provided a maximum EQE as high as 10.6%. In addition to the above reports, the xanthenes are rarely found in the field of organic light-emitting diodes (OLEDs). To further improve the performance of OLEDs, it is worth studying the use of xanthone derivatives as host materials.

In this chapter, we design and synthesize three new xanthone derivatives as host materials, 3-(4-(diphenylamino)-9H-carbazol-9-yl)-9H-xanthen-9-one(XanCarDipha), 2-(4-(4-(diphenylamino)-9H-carbazol-9-yl)phenyl)-9H-xanthen-9-one(p-XanCarDipha), and 2-(3-(4-(diphenylamino)-9H-carbazol-9-yl)phenyl)-9H-xanthen-9-one (m-XanCarDipha), and fabricate corresponding single- and double-host materials systems for use as the EML in PHOLEDs. Among these host materials, the carbazole and diphenylamino groups were selected as electron-donating (D) substituents, the xanthone moiety was selected as electron-accepting (A) substituents. Due to the introduction of carbazole and diphenylamino groups, it can improve the hole transport performance in the light-emitting layer, and improve the carrier balance. Thus, the efficiency roll-off of device was reduced.(39) Otherwise, the phenylene is introduced to extend the π -conjugation, and build the D- π -A architectures in p-XanCarDipha, and m-XanCarDipha. Their properties of PHOLEDs were systematically investigated in order to understand the structure-energy level -device performance correlations for developing efficient PHOLED materials. In addition, 1:1 p-XanCarDipha: CarTria of two hosts was used to make the carrier concentration in the EML becoming rich in electrons, which is beneficial for carrier balance.(40) Therefore, the combination of two hosts could be a promising method to regulate carrier balance and improve luminous efficiency in OLEDs.

II. Experiment content

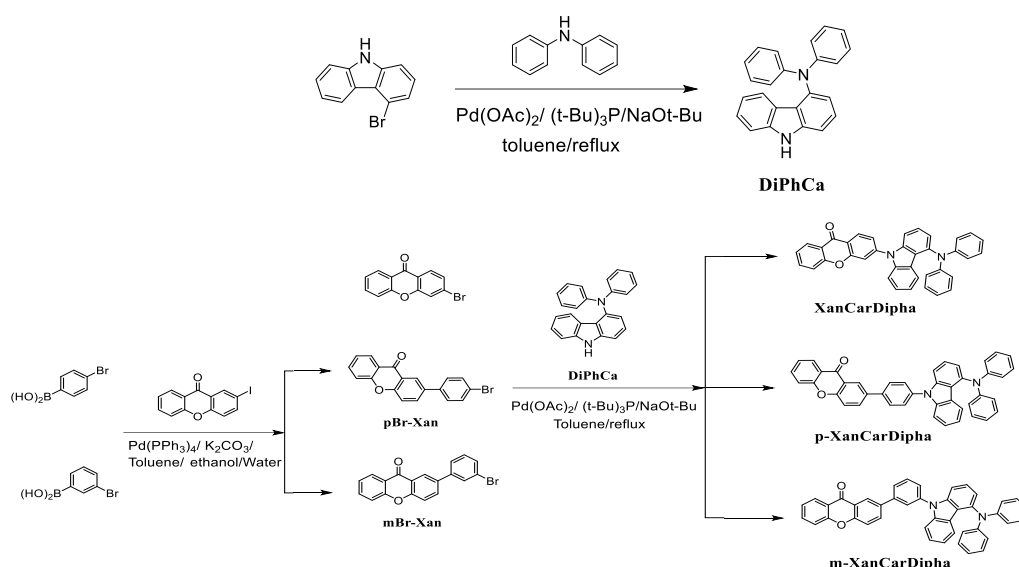
II-1. General information

Functional materials used in the above PhOLEDs, such as dipyrzino (2,3-f:20,3'-h) quinoxaline - 2,3,6,7,10,11-hexacarbonitrile (**HATCN**)⁽⁴¹⁾, N₄, N₄,N₄',N₄'-tetra((1,1'-biphenyl)-4-yl)-(1,1'- biphenyl)-4,4'-diamine (**TBPDIA**)⁽⁴²⁾, N-((1,10-biphenyl) -2-yl)-N-(9,9-dimethyl-9H-fluoren-2-yl)-9,90-spirobi(fluor en) -2-amine (**FSFA**)⁽⁴³⁾, 9-((1,1'-biphenyl)-3-yl)-9'- ((1,1'-biphenyl)-4-yl)- 9H, 9'H-3,3'- bicarbazole (**BiCar**)⁽⁴⁴⁾, 11-(4,6-diphenyl-1,3,5-triazin-2-yl)-12-phen yl-11,12- dihydroindolo(2,3-a)carbazole (**CarTria**)⁽⁴⁵⁾, 2-(4-(9,10-di(naphthale n-2-yl) anthracen-2-yl) phenyl)-1-phenyl- 1H-benzo(d)imidazole (**NAPI**)⁽⁴⁶⁾, 8-hydroxyquinolinolato-lithium (**LiQ**)⁽⁴⁷⁾ and tris(2-phenyl- pyridine)iridium (**Ir (ppy)₃**)⁽⁴⁸⁾, are commercially available. Al as cathode was purchased from commercial corporations and was used without purification.

Nuclear magnetic resonance (NMR) were collected on a Bruker (Beijing) Scientific Technology Co., Ltd AVIII 400-MHz spectrometer, Beijing, China. Liquid chromatography–mass spectrometry (LC-MS) was acquired using an Agilent 6460 LC-MS instrument. For photophysical characterization, 60 nm-thick films were deposited by thermal evaporation onto pre-cleaned silica substrates. Ultraviolet–visible (UV-vis) absorption and photoluminescence (PL) spectra of the films were measured by using an HP-8453 UV-vis Spectrophotometer (Agilent) and Fluoromax-4 spectrophotometer (Horiba Scientific), respectively. Thermal analysis was performed by differential scanning calorimetry (DSC) on a DSC-200 F3 Netzsch analyzer (Selb, Germany) with a heating rate of 10 °C·min⁻¹ under a nitrogen atmosphere. HOMO energy levels were measured by an ionization potential spectrometer (IPS-3, Bunkoukeiki Co., Ltd, Tokyo, Japan). All the materials for OLED devices were further purified by sublimation under vacuum conditions and obtained purities were exceeded 99.9%. The current density–voltage–luminance (J-V-L) and the efficiency (EQE, CE, PE) of devices were measured with a source measure unit (FS-1000GA4 FSTAR, Suzhou, China) and spectrometer (CS-2000AFSTAR, Suzhou, China)

II-2. Synthesis and characterization

The synthetic routines of XanCarDipha, *p*-XanCarDipha, and *m*-XanCarDipha are shown in Scheme 1. Firstly, by using Suzuki coupling reaction, intermediates of *p*Br-Xan and *m*Br-Xan were synthesized, and then reacted with prepared DiphCa by Buchwald-Hartwig coupling. Three compounds of **XanCarDipha**, ***p*-XanCarDipha**, and ***m*-XanCarDipha** were characterized by ¹H NMR, ¹³C NMR and LC-MS. In to obtain more pure materials, the products were further purified by sublimation under vacuum conditions. More details about characterization information can be found in attachments. **XanCarDipha**, ***p*-XanCarDipha**, and ***m*-XanCarDipha** were obtained according to Scheme 1, as explained in detail below.



Scheme 1 Synthesis of **XanCarDipha**, ***p*-XanCarDipha** and ***m*-XanCarDipha**

II-2-1. Synthesis of N,N-diphenyl-9H-carbazol-4-amine (DiPhCa)

A mixture of 4-bromo-9H-carbazole (5.0 g, 20.32 mmol), diphenylamine (4.13 g, 24.38 mmol), Pd(OAc)₂ (0.23 g, 1.02 mmol), 10wt% t-Bu₃P in toluene (5.0 mL, 2.03 mmol), NaOt-Bu (3.91g, 40.64 mmol), and 150 ml of anhydrous toluene were added in a two-neck round-bottom flask equipped with a condenser. The reaction mixture was stirred for 16 h refluxed at 110°C in a nitrogen atmosphere. After cooling to room temperature, the mixture was quenched with water (100 ml), organic phase was separated and aqueous phase was extracted with CH₂Cl₂. The organic layers combined and dried over Na₂SO₄ and evaporated under reduced pressure. The crude product was

purified by a silica column with n-hexane:dichloromethane (1:1) solvent system to obtain the target molecule **DiPhCa** as a yellow solid (4.78 g, yield:58.4%). ¹H NMR (400 MHz, CDCl₃) δ=8.08 (s, 1H), 7.69 (ddd, *J* = 8.0, 1.2, 0.6 Hz, 1H), 7.41 – 7.29 (m, 4H), 7.22 – 7.16 (m, 4H), 7.13 – 7.08 (m, 4H), 6.99 – 6.90 (m, 4H). ¹³C NMR (100 MHz, CDCl₃) δ= 147.68, 141.51, 141.32, 139.41, 129.24, 126.93, 125.78, 123.17, 121.97, 121.86, 121.78, 120.63, 119.69, 110.08, 108.07. MS m/z (ESI) Calcd for C₂₄H₁₈N₂: 334.15; Found: 335.30 (M+H)⁺.

II-2-2. Synthesis of 3-(4-(diphenylamino)-9H-carbazol-9-yl)-9H-xanthen-9-one (XanCarDipha)

Under nitrogen protection, 3-bromo-9H-xanthen-9-one (3.0 g, 10.91 mmol), **DiPhCa** (4.35 g, 13.01 mmol), Pd(OAc)₂ (0.12 g, 0.55 mmol), 10wt% t-Bu₃P in toluene (2.57 mL, 1.1 mmol), NaOt-Bu (2.10 g, 21.82 mmol) and toluene (120 mL) were added at room temperature. The reaction mixture was stirred at 110 °C for 16 h. After cooling to room temperature, the mixture was quenched with water (100 mL), organic phase was separated and aqueous phase was extracted with CH₂Cl₂. The organic layers combined and dried over Na₂SO₄, vaporated under reduced pressure. Then the crude product was purified by column chromatography over silica using n-hexane:dichloromethane(1:2) as eluent to afford **XanCarDipha** as light yellow solid (3.70 g, 64.2%); ¹H NMR (400 MHz, CDCl₃) δ= 8.59 (d, *J* = 8.5 Hz, 1H), 8.41 (dd, *J* = 8.0, 1.7 Hz, 1H), 7.83 (dt, *J* = 7.9, 1.0 Hz, 1H), 7.80 – 7.75 (m, 2H), 7.68 (dd, *J* = 8.5, 1.9 Hz, 1H), 7.53 (ddd, *J* = 9.2, 8.4, 1.0 Hz, 2H), 7.48 – 7.42 (m, 3H), 7.35 (ddd, *J* = 8.4, 7.2, 1.2 Hz, 1H), 7.24 – 7.20 (m, 4H), 7.16 – 7.14 (m, 4H), 7.07 (tt, *J* = 7.3, 1.1 Hz, 2H), 6.98 – 6.93 (m, 2H). ¹³C NMR (100 MHz, CDCl₃): δ = 176.54, 157.23, 156.41, 147.62, 143.71, 141.93, 141.80, 140.09, 135.20, 129.33, 128.78, 127.39, 126.96, 126.26, 124.48, 123.42, 122.67, 122.41, 122.26, 122.10, 122.02, 121.30, 121.17, 120.66, 118.13, 115.72, 109.34, 107.32. MS m/z (ESI) Calcd for C₃₇H₂₄N₂O₂: 528.18; Found: 529.27 (M+H)⁺.

II-2-3. Synthesis of 2-(4-bromophenyl)-9H-xanthen-9-one (pBr-Xan)

A mixture of 2-iodo-9H-xanthen-9-one (3.0 g, 9.31 mmol), (4-bromophenyl)boronic acid (2.24 g, 11.17 mmol), Pd(PPh₃)₄ (0.54 g, 0.47 mmol), toluene (150 mL), and K₂CO₃ (1 M, 50 mL) were placed under vacuum and then backfilled with nitrogen three times before being heated in an oil bath at 110°C for 16 h. After cooling to room temperature, the organic layer was

separated. The aqueous phase was extracted with CH₂Cl₂ (3×50 mL), and the combined organic phases were dried over Na₂SO₄, filtered, and then the solvent was evaporated under reduced pressure. The crude product was purified by column chromatography over silica using dichloromethane : EtOAc (5:1) as eluent to afford the product as a white solid (2.50 g, 76.5%); ¹H NMR (400 MHz, CDCl₃) δ = 8.49 (dd, *J* = 2.5, 0.5 Hz, 1H), 8.34 (ddd, *J* = 8.0, 1.7, 0.5 Hz, 1H), 7.90 (dd, *J* = 8.7, 2.4 Hz, 1H), 7.73 (ddd, *J* = 8.4, 7.1, 1.8 Hz, 1H), 7.59 – 7.48 (m, 6H), 7.39 (ddd, *J* = 8.1, 7.1, 1.1 Hz, 1H). ¹³C NMR (100 MHz, CDCl₃) δ = 177.20, 156.22, 155.79, 138.39, 135.87, 135.07, 133.42, 132.20, 128.75, 126.91, 124.55, 124.19, 122.16, 122.06, 121.86, 118.82, 118.15. MS *m/z* (ESI) Calcd for C₁₉H₁₁BrO₂: 349.99; Found: 351.38 (M+H)⁺.

II-2-4. Synthesis of 2-(4-(4-(diphenylamino)-9H-carbazol-9-yl)phenyl)-9H-xanthen-9-one (p-XanCarDipha)

Under nitrogen protection, **pBr-Xan** (2.50 g, 7.12 mmol), **DiPhCa** (2.86 g, 8.54 mmol), Pd(OAc)₂ (0.081 g, 0.36 mmol), 10wt% t-Bu₃P in toluene (1.66 mL, 0.71 mmol), NaOt-Bu (1.37 g, 14.24 mmol) and toluene (100 mL) were added at room temperature. The reaction mixture was stirred at 110°C for 16 h. After cooling to room temperature, the mixture was quenched with water (100 mL), organic phase was separated and aqueous phase was extracted with CH₂Cl₂. The organic layers combined and dried over Na₂SO₄, evaporated under reduced pressure. Then the crude product was purified by column chromatography over silica using n-hexane:dichloromethane (1:2) as eluent to afford **p-XanCarDipha** as light yellow solid (3.16 g, 73.5%); ¹H NMR (400 MHz, CDCl₃) δ = 8.68 (d, *J* = 2.4 Hz, 1H), 8.40 (dd, *J* = 8.0, 1.7 Hz, 1H), 8.07 (dd, *J* = 8.7, 2.4 Hz, 1H), 7.93 (d, *J* = 8.4 Hz, 2H), 7.83 (d, *J* = 7.9 Hz, 1H), 7.78 – 7.69 (m, 3H), 7.63 (d, *J* = 8.7 Hz, 1H), 7.54 (dd, *J* = 8.5, 1.0 Hz, 1H), 7.45 – 7.38 (m, 3H), 7.37 – 7.31 (m, 2H), 7.25 – 7.20 (m, 4H), 7.18 – 7.14 (m, 4H), 7.04 (tt, *J* = 7.4, 1.1 Hz, 2H), 6.95 (tt, *J* = 7.1, 1.4 Hz, 2H). ¹³C NMR (100 MHz, CDCl₃) δ = 177.29, 156.30, 155.89, 147.71, 142.73, 141.57, 140.87, 138.79, 137.28, 136.14, 135.12, 133.64, 129.29, 128.66, 127.97, 127.04, 126.96, 125.95, 124.84, 124.25, 123.23, 122.20, 121.98, 121.93, 121.86, 121.40, 120.77, 120.32, 118.93, 118.20, 109.34, 107.36. Calcd for C₄₃H₂₈BN₂O₂: 604.22; Found: 605.53 (M+H)⁺.

II-2-5. Synthesis of 2-(3-bromophenyl)-9H-xanthen-9-one (mBr-Xan)

A mixture of 2-iodo-9*H*-xanthen-9-one (3.0 g, 9.31 mmol), (3-bromophenyl)boronic acid(2.24 g, 11.17 mmol), Pd(PPh₃)₄ (0.54 g, 0.47 mmol), toluene (150 mL), and K₂CO₃ (1 M, 50 mL) was placed under vacuum and then backfilled with nitrogen three times before being heated in an oil bath at 110 °C for 16 h. After cooling to room temperature, the layers were separated. The aqueous phase was extracted with CH₂Cl₂ (3×50 mL), and the combined organic phases were dried over Na₂SO₄, filtered, and then the solvent was evaporated under reduced pressure. The crude product was purified by column chromatography over silica using dichloromethane:EtOAc (5:1) as eluent to afford the product as a white solid (2.32 g, 71.1%); ¹H NMR (400 MHz, CDCl₃) δ= 8.51 (dd, *J* = 2.4, 0.5 Hz, 1H), 8.36 (ddd, *J* = 7.9, 1.8, 0.5 Hz, 1H), 7.92 (dd, *J* = 8.7, 2.4 Hz, 1H), 7.82 (t, *J* = 1.8 Hz, 1H), 7.74 (ddd, *J* = 8.7, 7.1, 1.8 Hz, 1H), 7.63 – 7.55 (m, 2H), 7.54 – 7.48 (m, 2H), 7.40 (ddd, *J* = 8.1, 7.1, 1.1 Hz, 1H), 7.34 (t, *J* = 7.9 Hz, 1H). ¹³C NMR (100 MHz, CDCl₃) δ= 177.20, 156.25, 155.95, 141.59, 135.61, 135.10, 133.57, 130.75, 130.59, 130.26, 126.94, 125.82, 124.88, 124.23, 123.23, 122.09, 121.89, 118.86, 118.16. MS *m/z* (ESI) Calcd for C₁₉H₁₁BrO₂: 349.99; Found: 351.05 (M+H)⁺.

II-2-6. Synthesis of 2-(3-(4-(diphenylamino)-9*H*-carbazol-9-yl)phenyl)-9*H*-xanthen-9-one (*m*-XanCarDipha)

Under nitrogen protection, *m*Br-Xan (2.30 g, 6.55 mmol), DiPhCa (2.63 g, 7.86 mmol), Pd(OAc)₂ (0.074 g, 0.33 mmol), 10 wt% t-Bu₃P in toluene(1.54 mL, 0.66 mmol),NaOt-Bu(1.26 g, 13.1 mmol) and toluene (100ml)were added at room temperature. The reaction mixture was stirred at 110°C for 16 h. After cooling to room temperature, the mixture was quenched with water (100 ml), organic phase was seperated and aqueous phase was extracted with CH₂Cl₂. The organic layers combined and dried over Na₂SO₄, evaporated under reduced pressure. Then the crude product was purified by column chromatography over silica using n-hexane:dichloromethane(1:2) as eluent to afford *m*-XanCarDipha as light yellow solid (2.59 g, 65.3%); ¹H NMR (500 MHz, CDCl₃) δ = 8.63 (d, *J* = 2.3 Hz, 1H), 8.37 (dd, *J* = 8.0, 1.7 Hz, 1H), 8.01 (dd, *J* = 8.7, 2.4 Hz, 1H), 7.91 (t, *J* = 1.9 Hz, 1H), 7.84 – 7.79 (m, 2H), 7.77 – 7.70 (m, 2H), 7.64 – 7.57 (m, 2H), 7.52 (dd, *J* = 8.6, 1.0 Hz, 1H), 7.42 – 7.37 (m, 3H), 7.34 (dt, *J* = 8.3, 1.1 Hz, 2H), 7.24 – 7.20 (m, 4H), 7.18 – 7.15 (m, 4H), 7.03 (ddd, *J* = 8.4, 7.2, 1.1 Hz, 2H), 6.97 – 6.91 (m, 2H). ¹³C NMR (100 MHz,

CDCl₃) δ = 177.20, 156.26, 155.98, 147.69, 142.82, 141.58, 141.51, 140.95, 138.47, 135.97, 135.11, 133.65, 130.71, 129.29, 127.07, 126.96, 126.77, 126.47, 126.18, 125.96, 124.91, 124.24, 123.24, 122.16, 121.98, 121.91, 121.37, 120.72, 120.29, 118.94, 118.17, 109.27, 107.30. Calcd for C₄₃H₂₈BN₂O₂: 604.22; Found: 605.45 (M+H)⁺.

II-3. Fabrication of PHOLEDs

The structures of the devices and chemicals are shown in Fig.1. The ITO-coated glass substrates (50×50 mm) were cleaned by detergent and deionized water. Sequentially, the above substrates were treated by isopropyl alcohol in an ultrasonic cleaner for 20 min and then were put in a vacuum oven at 250°C for 30 min. All organic materials and Al (cathode) were deposited on the pre-cleaned ITO-coated glass substrate under $<1.33 \times 10^{-4}$ Pa. Ultimately, all devices were encapsulated using a glass cover. All the processes of encapsulation were conducted inside a nitrogen-filled glove box.

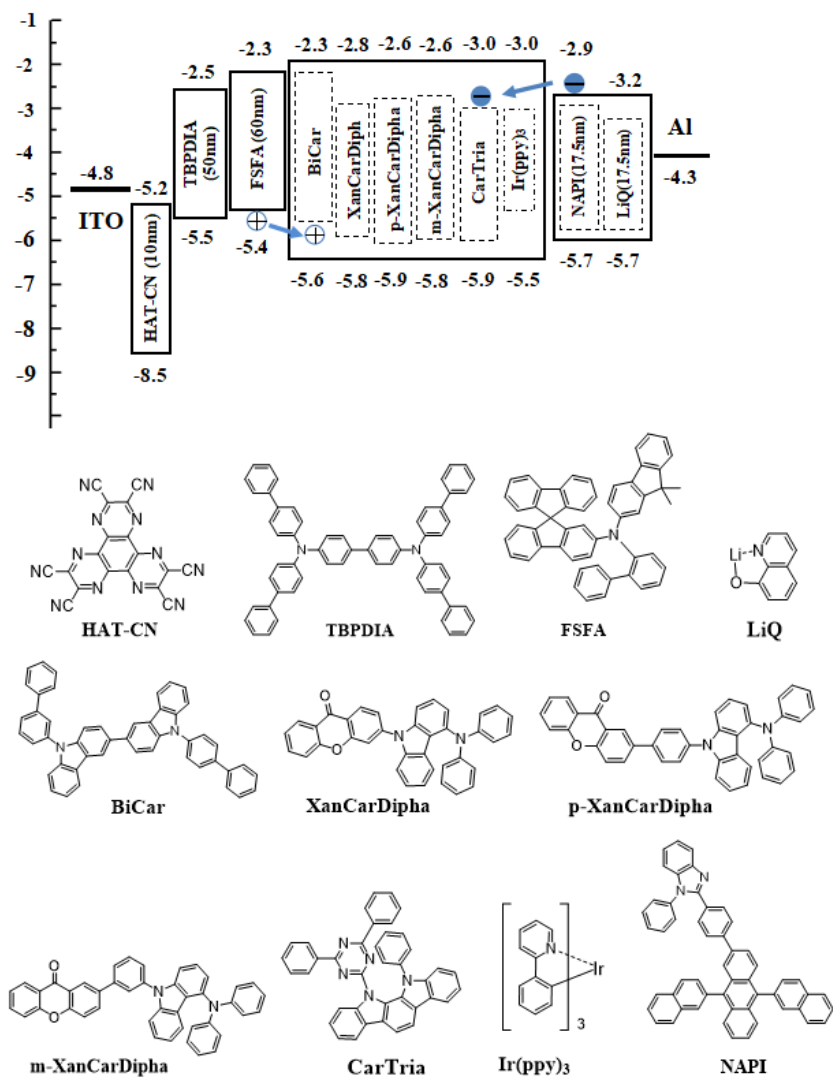


Fig.1 Energy level diagram of the OLEDs for investigated materials and the molecular structures of materials used in OLEDs

III. Results and discussion

III-1. Theoretical calculation

In order to better understanding the properties of these matrix materials, the density functional theory (DFT) with B3LYP/6-31G (d) method in the Gaussian 09 software package was used to obtain the highest occupied molecular orbital (HOMO) and the lowest unoccupied molecular orbital (LUMO) of **XanCarDipha**, **p-XanCarDipha**, and **m-XanCarDipha**. The spatial distribution of HOMO and LUMO is shown in Fig.2. The HOMOs of these molecules are

mainly located on carbazole and diphenyl amino groups, while LUMOs are mainly distributed on xanthone moiety, and there is almost no overlap between HOMO and LUMO among these molecules. It shows that when they are used in the luminescent layer, the holes and electrons can migrate simultaneously from the carbazole and diphenyl amino parts and the xanthone unit, respectively, without interfering with each other. Therefore, all three host materials may exhibit bipolar properties.⁽⁴⁹⁾ The calculated T_1 values of **XanCarDipha**, ***p*-XanCarDipha**, and ***m*-XanCarDipha** were 2.67, 2.77 and 2.72 eV (Table 1), respectively, which were higher than 2.42 eV of Ir(ppy)₃. The results show that the calculated T_1 values are suitable for the application as host materials for Ir(ppy)₃-based OLEDs.

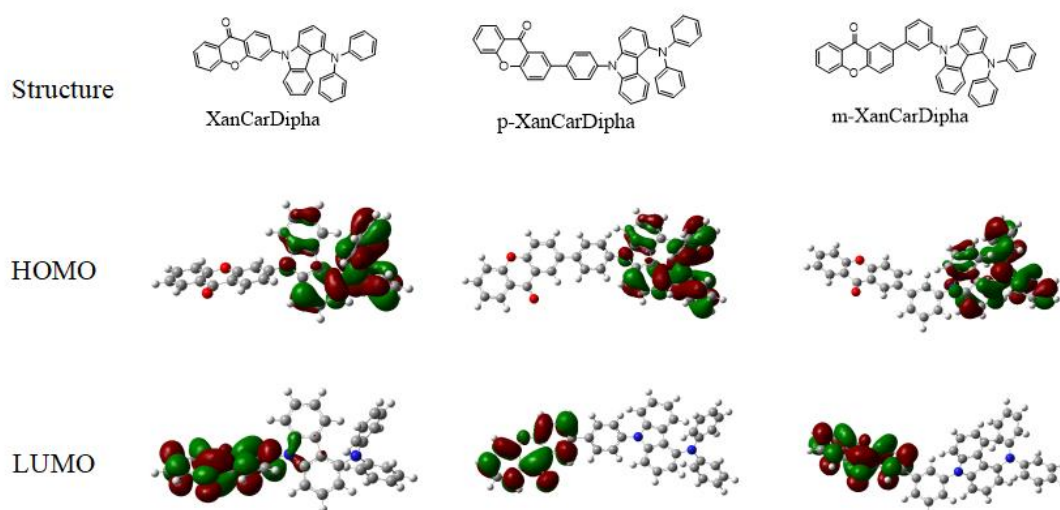


Fig.2 Molecular structures and spatial distributions of HOMOs and LUMOs of **XanCarDipha**, ***p*-XanCarDipha**, and ***m*-XanCarDipha**

Table 1 Calculated HOMO, LUMO, Eg, S₁, T₁, values from TD-DFT at B3LYP/6-31g(d) level

Compounds	HOMO/eV	LUMO/eV	Eg/eV	S ₁ /eV	T ₁ /eV	ΔE _{st}
XanCarDipha	5.03	1.94	3.09	2.75	2.67	0.08
<i>p</i>-XanCarDipha	4.91	1.91	3.00	2.78	2.77	0.01
<i>m</i>-XanCarDipha	4.93	1.91	3.02	2.78	2.72	0.06

III-2. Photophysical properties

The film absorption spectra of **XanCarDipha**, **p-XanCarDipha**, and **m-XanCarDipha** is shown in Fig.3.

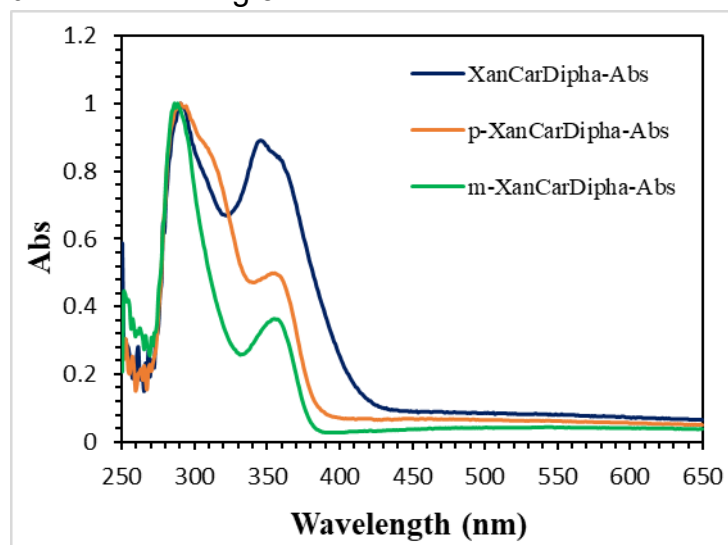


Fig.3 Normalized absorption spectra of **XanCarDipha**, **p-XanCarDipha** and **m-XanCarDipha** in thin film

Table 2 Energy level and photophysical data for PHOLED materials

Compounds	^a HOM O/eV	^b LUM O/eV	^c E _g /e V	^d S ₁ /e V	^d T ₁ /e V	ΔE _{ST}	T _g /°C	T _m /°C
XanCarDipha	-5.83	-2.77	3.06	2.90	2.84	0.06	123.8	205.0
p-XanCarDipha	-5.85	-2.61	3.24	3.21	2.84	0.37	124.9	267.6
m-XanCarDipha	-5.84	-2.58	3.26	3.40	2.88	0.52	122.3	194.0
CarTria	-5.90	-3.00	2.90	2.82	2.79	0.03	-	-
BiCar	-5.64	-2.27	3.37	3.28	2.85	0.43	-	-
Ir(ppy)₃ ^(48,57)	-5.50	-3.00	2.50	2.80	2.42	-	-	-

^a HOMO energy levels were determined by using an ionization energy measurement system

^bLUMO=HOMO+E_g.

^cE_g was calculated from the absorption onset of the film ($E_g^{opt}=1240/\lambda_{onset}$)⁽⁵⁸⁾

^dT₁ and S₁ were calculated from the tangent lines of PL spectra of films⁽⁵⁹⁾

The absorption signals around 350-360 nm were found as ICT (intramolecular charge transfer) absorption bands which were recognized as

charge transfer from the donor (carbazole and diphenylamine groups) to the receptor (xanthone moiety).⁽⁵⁰⁾ It is worth noting that **XanCarDipha** exhibits a significantly stronger and wider absorption band near 350 nm, which proves that it has a stronger ICT state than the other two materials. This suggests that the separation of donor and acceptor by an additional phenyl bridge could weaken ICT absorption of ***p*-XanCarDipha**, and ***m*-XanCarDipha** which resulted in blue-shifted spectrum.^(51,52) Therefore, for **XanCarDipha**, ***p*-XanCarDipha**, and ***m*-XanCarDipha** with similar HOMO (Table 2), a deeper LUMO level was obtained in **XanCarDipha** with narrower E_g . The optical band gaps (E_g) of **XanCarDipha**, ***p*-XanCarDipha**, and ***m*-XanCarDipha** calculated by tangent method from absorption spectra are 3.06 eV, 3.24 eV and 3.26 eV, respectively (Table 3). The singlet and triplet energy levels calculated by tangent method from the fluorescence and phosphorescence spectra of **XanCarDipha** are 2.90 and 2.84 eV, ***p*-XanCarDipha** are 3.21 and 2.84 eV, and ***m*-XanCarDipha** are 3.40 and 2.88 eV (Table 4 and Fig.4). Note that significant differences are observed between the theoretical calculations and the experimental values in ΔE_{st} (Table 2). The possible reason for this phenomenon is that, in practice, the ΔE_{st} values of materials are often a mixture of charge transfer (CT) and local excitation (LE) adiabatic states, and the amount of mixing is caused by vibration coupling.⁽⁵³⁻⁵⁵⁾

Table 3 Tangent line value of UV-visible absorption spectra and calculated E_g

Materials	λ tangent line of UV-visible absorption spectra (nm)	E_g (eV)
XanCarDipha	405	3.06
<i>p</i>-XanCarDipha	383	3.24
<i>m</i>-XanCarDipha	380	3.26

$$E_g = 1240/\lambda_{\text{tangent line}}$$

Table 4 Tangent line value of fluorescence phosphorescence spectra and calculated

Materials	λ tangent line of fluorescence (nm)	S_1 (eV)	λ tangent line of phosphorescence (nm)	T_1 (eV)
XanCarDipha	428	2.90	436	2.84
<i>p</i>-XanCarDipha	386	3.21	436	2.84
<i>m</i>-XanCarDipha	386	3.21	430	2.88

T_1 or $S_1 = 1240/\lambda_{\text{tangent line}}$

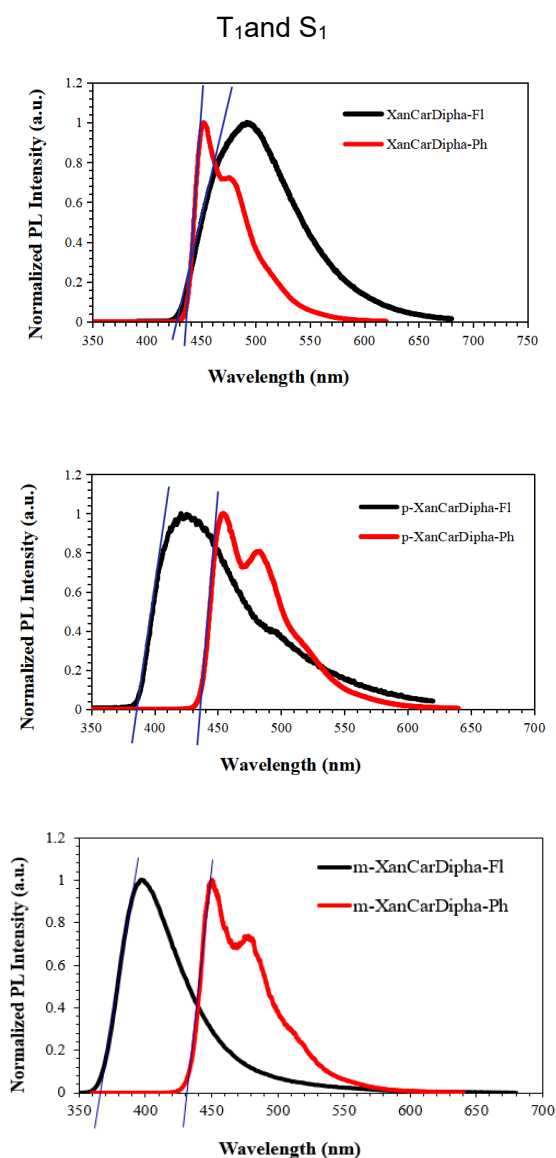


Fig.4 Normalized photoluminescence (293K) and phosphorescence (77 K) spectra of **XanCarDipha**, ***p*-XanCarDipha** and ***m*-XanCarDipha** with tangent lines

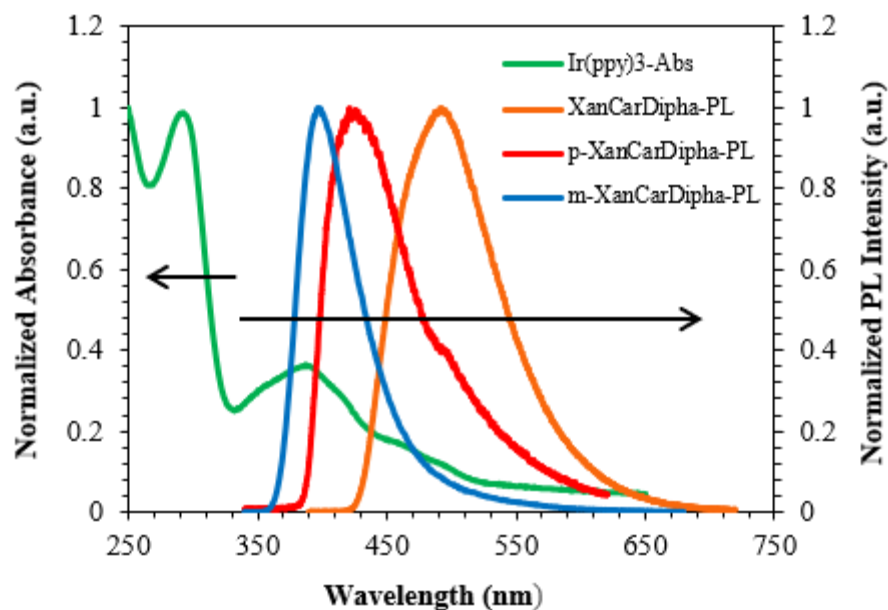


Fig.5 Normalized absorption spectrum of Ir(ppy)_3 and photoluminescence spectra of **XanCarDipha**, ***p*-XanCarDipha**, and ***m*-XanCarDipha** in thin films (excitation wavelength: 370, 320, and 300 nm, respectively)

Fig.5 shows the emission spectra of the main materials **XanCarDipha**, ***p*-XanCarDipha** and ***m*-XanCarDipha**, and the UV-Vis absorption spectrum of Ir(PPy)_3 . The emission spectra of these three materials have obvious overlap with the absorption spectra of Ir(PPy)_3 . Therefore, the singlet (S_1) exciton energy of all host materials can be transferred to the S_1 level of Ir(PPy)_3 through Förster resonance energy transfer (FET).⁽⁵⁶⁾ Finally, the energy of S_1 state of Ir(PPy)_3 can be transferred to the triplet (T_1) state, and then decayed to ground state by emitting phosphorescence.

III-3. Thermal analysis

Differential scanning calorimetry (DSC) was carried out to study melting point (T_m) and glass transition temperature (T_g) of **XanCarDipha**, ***p*-XanCarDipha** and ***m*-XanCarDipha**. The results are shown in Table 2. The T_m values of these materials are 205.0, 267.6 and 194.0°C, respectively. After cooling, T_g s of **XanCarDipha**, ***p*-XanCarDipha** and ***m*-XanCarDipha** were obtained by a second heating scan. The T_g of these materials is 123.8°C, 124.9°C and 122.3°C, respectively. The T_g of the above host compounds was higher than that of 1,3-bis (9-carbazolyl) benzene (mCP, $T_g = 60^\circ\text{C}$) and

4,40-bis (9-carbazolyl) 2,20-biphenyl (CBP, $T_g = 62^\circ\text{C}$). This indicates that the amorphous glass stability of target compounds is better than that of CBP and mCP.⁽⁶⁰⁾

III-4. Electroluminescent (EL) properties

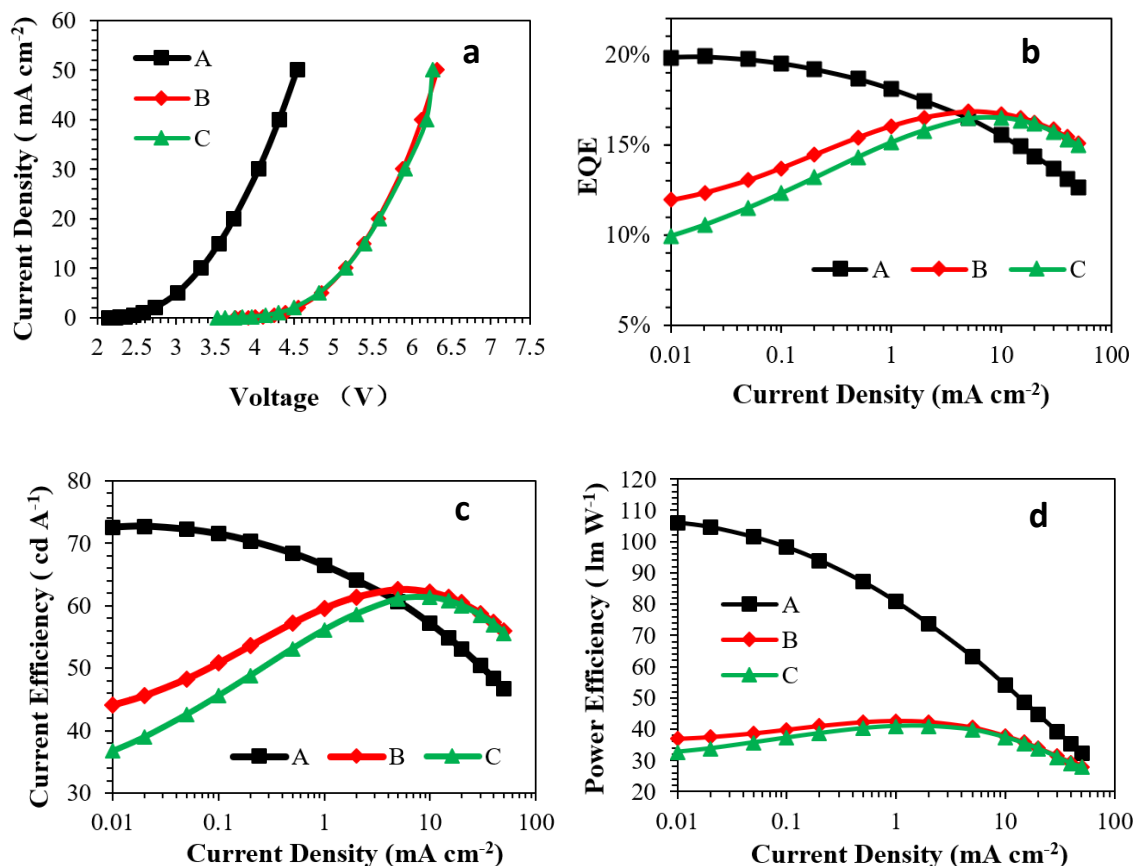


Fig.6 (a) Current density–voltage–luminance (J - V - L) characteristics and (b) External quantum efficiency (EQE), (c) current efficiency, and (d) power efficiency versus J of device A–C

The structure of PHOLED is ITO (150 nm)/HATCN (10 nm)/DBTPBDIA (50 nm)/FSFA (60 nm)/Host doped with 12 wt% Ir(ppy)₃ (40 nm)/NAPI:LiQ = 1:1 (35 nm)/Al (80 nm). HATCN, DBTPBDIA and FSFA are used as hole injection material (HIM), hole transport material (HTM) and electron barrier material (EBM), respectively. In addition, **XanCarDipha**, ***p*-XanCarDipha** and ***m*-XanCarDipha** are used as host material in Device A, B and C, respectively and Ir(PPy)₃ was functionalized as emissive dopant. Moreover, NAPI works as electron transport material (ETM) and LiQ as electron injection material (EIM). The chemical structure and corresponding energy level diagram of the

materials used in each functional layer of the device are shown in Fig.1. The current density and voltage (J-V) characteristics of device A-C are shown in Fig.6 and EL data in Table 5.

Table 5 Electroluminescence properties of devices A-C

Devices	Host	Voltage ^a	CE ^a /CE _{max} ^b (Cd A ⁻¹)	EQE ^a /EQE _{max} ^c	PE ^a /PE _{max} ^c (lm W ⁻¹)	CIE _x ^e	CIE _y ^e
A	XanCarDipha	3.32	57.15/72.7 2	15.52%/19.89 %	54.06/106.1 0	0.357 4	0.610 5
B	p-XanCarDipha	5.15	62.12/62.5 5	16.74%/16.86 %	37.84/42.60	0.339 4	0.622 1
C	m-XanCarDipha	5.15	61.29/61.2 9	16.51%/16.51 %	37.34/40.94	0.353 9	0.611 2

^aRecorded at 10 mA cm⁻².

^bMaximum current efficiency.

^cMaximum EQE.

^dMaximum power efficiency.

^eCommission Internationale de L'Eclairage (CIE) coordinates measured at 10 mA cm⁻².

Among devices, A showed a minimum of turn-on voltage of 3.32 V at 10 mA/cm². The relatively deep LUMO level of **XanCarDipha** may facilitate electron injection into EML. EQE – J curve of equipment A-C is shown in Fig.6(b). Tab.5 summarizes the device performance which is related with devices using only conventional single host (**XanCarDipha**, **p-XanCarDipha**, or **m-XanCarDipha**). Fig.6 shows that the carrier balance of device A is not ideal. When J increases from 0.01 to 100 mA/cm², the electron/hole mobility also increase gradually, but EQE of device A decreases. This indicates that device A will contain excess electrons with increasing current density because the electron mobility of device A increases more rapidly than the hole mobility (Fig.7 (c)). On the contrary, when J increases from 0.1 mA/cm² to 10 mA/cm², EQE of devices B and C increases gradually. Over 10 mA/cm², EQE of devices B and C will roll down due to TTA, TPA and/or TSA [61,62]. These results indicate that there are too many holes in the EML of devices B and C with low J (less than 10 mA/cm²) due to shallower LUMO levels of **p-XanCarDipha** and **m-XanCarDipha**. With increasement of J, the electron mobility increased and the carrier gradually reached equilibrium. When J continued to rise (higher than 10 mA/cm²), the triplet exciton concentration gradually increases causing more serious TTA, which lead to the roll-off of EQE.

The HOMO energy levels of **XanCarDipha**, **p-XanCarDipha** and

m-XanCarDipha are almost at same level. The main reason for the difference among efficiency curves of Device A-C is that the deeper LUMO energy level of **XanCarDipha**. Because of too deep LUMO (2.77 eV) of **XanCarDipha**, it makes electron easily inject into EML of Device A causing excessive electron. Therefore, the EML of device A has an excess of electrons at the low J . In contrast, the LUMO level of **p-XanCarDipha** and **m-XanCarDipha** is shallower than that of **XanCarDipha**, which makes it more difficult to inject electron. Therefore, the electron concentration in the EML of Device B and C is comparably lower, which results in excessive holes in the EML at low J .

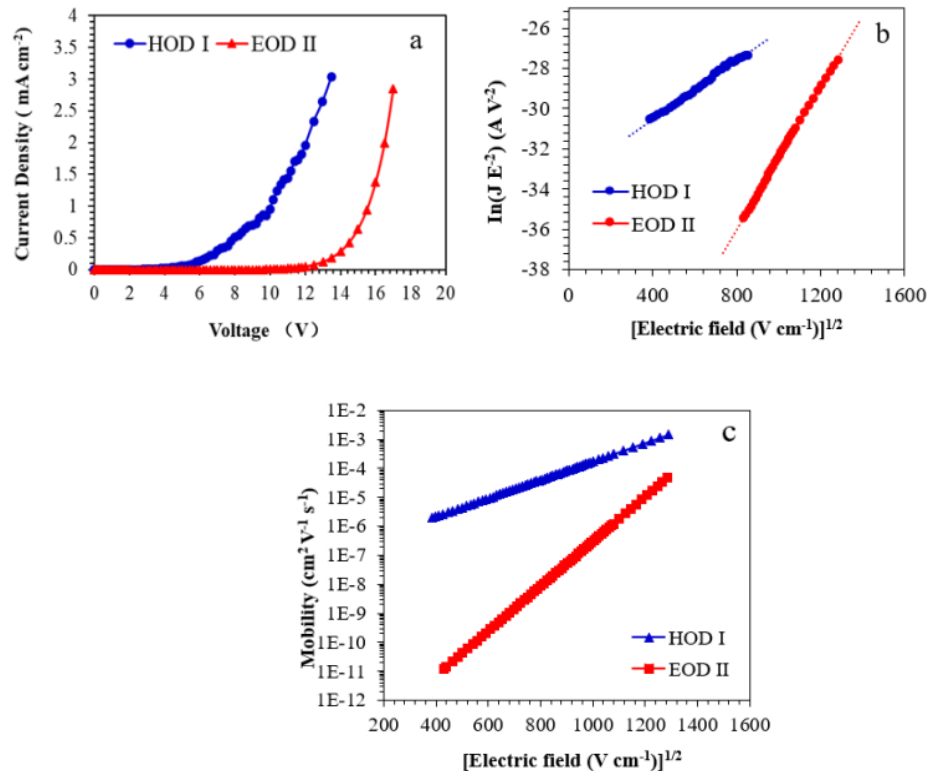


Fig.7 (a) The J–V characteristics of ho HOD I and EOD II . (b) $\ln(J E^{-2})$ -[Electric field]^{1/2} characteristics of HOD I and EOD II . (c) Mobility-square root of electric field for HOD I and EOD II

III-5. Device optimization

In order to understand the carrier equilibrium ability and its influence on the performance of the devices, the hole-only devices (HODs) and electron-only devices (EODs) were prepared to evaluate their carrier transmission characteristics. The structure of HOD and EOD is as follows [63,64].

HOD 1: ITO/HATCN (10 nm)/**p-XanCarDipha** (100 nm)/HATCN (10 nm)/Al (80

nm).

HOD 2: ITO/HATCN (10 nm)/CarTria (100 nm)/HATCN (10 nm)/Al (80 nm).

HOD 3: ITO/HATCN (10 nm)/**p-XanCarDipha**:CarTria = 1:1 (100 nm)/HATCN (10 nm)/Al (80 nm).

EOD 1: ITO/LiQ (1.5 nm)/**p-XanCarDipha** (100 nm)/LiQ (1.5 nm)/Al (80 nm).

EOD 2: ITO/LiQ (1.5 nm)/CarTria (100 nm)/LiQ (1.5 nm)/Al (80 nm).

EOD 3: ITO/LiQ (1.5 nm)/**p-XanCarDipha**:**CarTria** (100 nm)/LiQ (1.5 nm)/Al (80 nm).

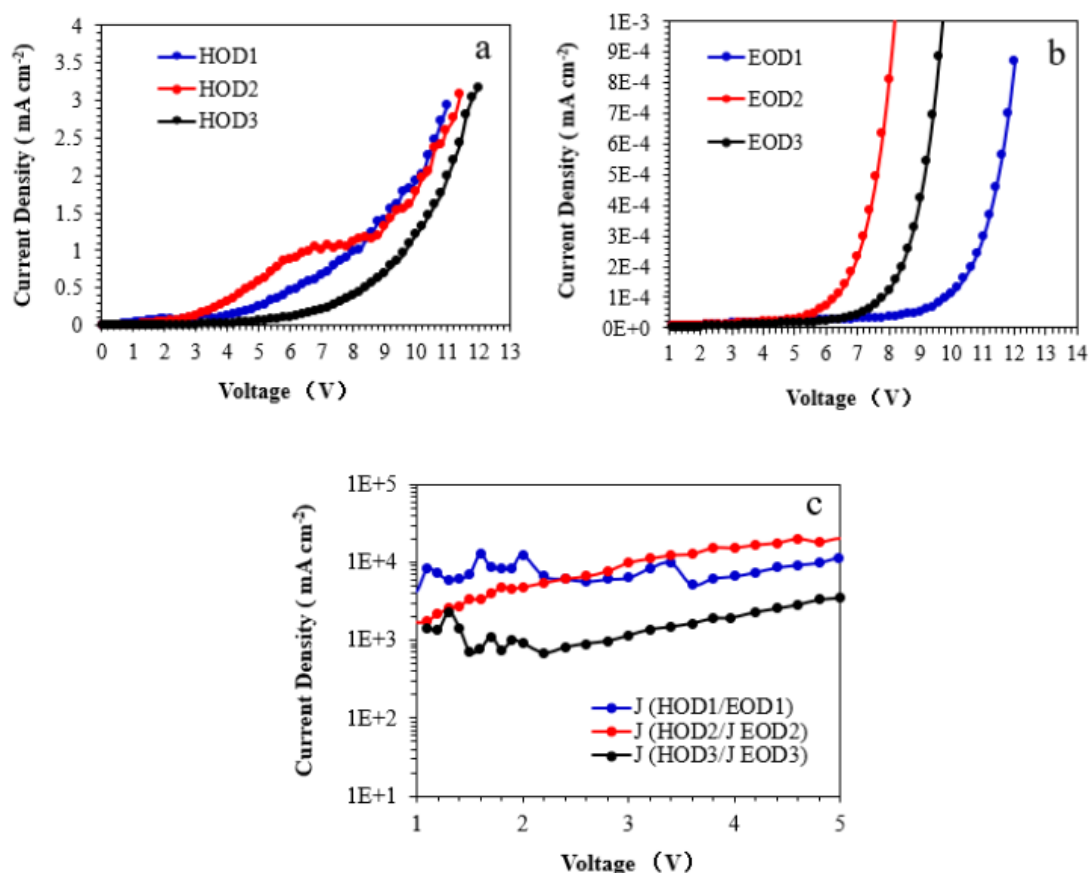


Fig.8 Current density versus voltage (J - V) characteristics of the (a) hole- and (b) electron-only devices. (c) Relative current density in host materials. (J (HOD)/ J (EOD))

The HODs/EODs' current density voltage curves are shown in Fig.8. In order to estimate the charge balance when the compounds were used as hosts in EML, the relative current density of these devices is obtained by dividing the hole current density of HODs and electron current density of EODs [J (hole)/ J (electron)] which are presented in Fig.8 (c).⁽⁶³⁾ It can be seen from the figure that the relative current density in the two host materials [**p-XanCarDipha**:**CarTria** = 1:1, J (HOD3)/ J (EOD3)] can provide the most

ideal carrier balance, as the relative current density value was the closest to unity.

To optimize the configuration of EML to further improve the performance of the device, OLED devices were manufactured via the combination of two hosts. Devices with the construction of ITO (150 nm)/HATCN (10 nm)/DBTPBDIA (50 nm)/FSFA (60 nm)/Host 1:Host 2:Ir(ppy)₃ = 44:44:12 wt% (40 nm)/NAPI:LiQ 1:1 (35 nm)/Al (80 nm) were fabricated. A standard device for comparison was fabricated using commercial host **CarTria** and BiCar which were selected as the second matrix materials because of the excellent performance of PHOLED in the reported works (65-68).

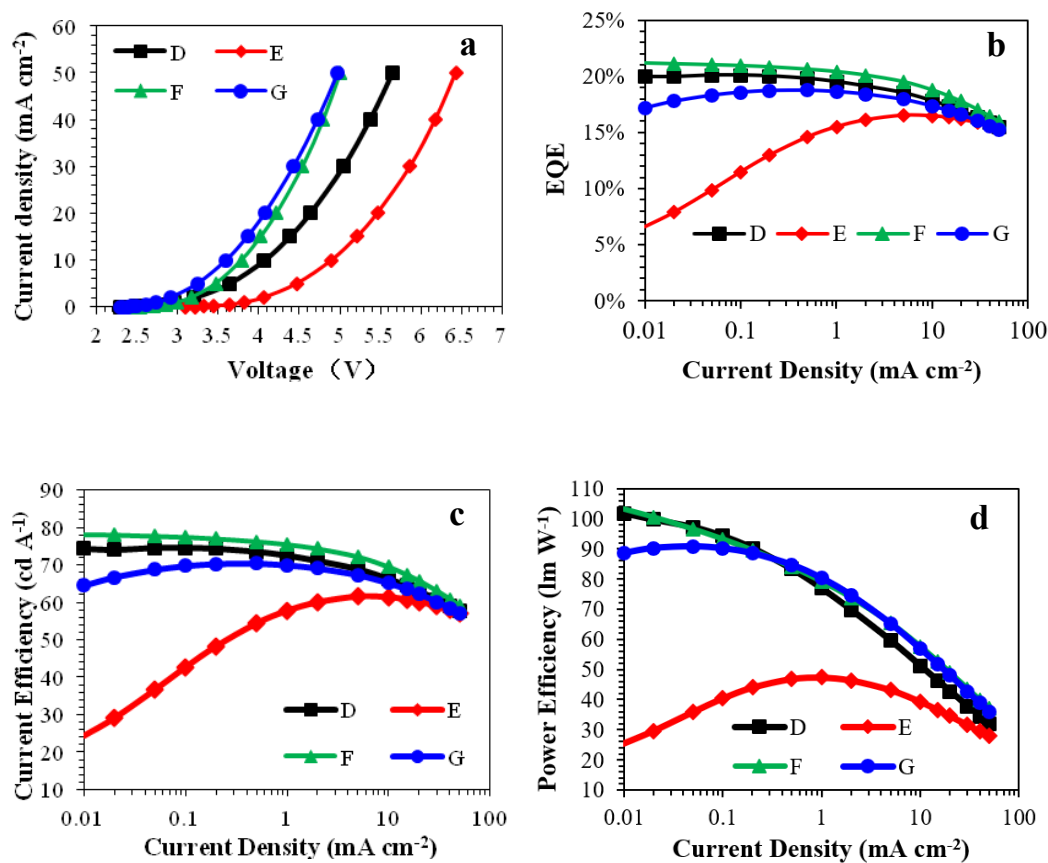


Fig. 9. (a) Current density–voltage–luminance (J – V – L) characteristics and (b) external quantum efficiency (EQE) versus current density (J) of the devices and (c) external quantum efficiency (EQE), (d) current efficiency, and (e) power efficiency versus J of device D–G.

Table 6 Electroluminescence properties of devices D-G

Devices	Host1:Host2	Voltage ^a	CE ^a /CE _{max} ^b (Cd/A)	EQE ^a /EQE _{max} ^b	PE ^a /PE _{max} ^c (lm/W)	CIE _x ^e	CIE _y ^e
D	XanCarDipha :BiCar	4.07	66.29/74.59	17.82%/20.09 %	51.16/101.8 3	0.3498	0.615 0
E	p-XanCarDiph a:BiCar	4.90	61.32/61.5	16.48%/16.52 %	39.29/47.35	0.3234	0.632 0
F	p-XanCarDiph a:CarTria	3.79	69.44/77.40	19.00%/20.93 %	57.59/93.15	0.3250	0.631 0
G	CarTria:BiCar	3.60	65.14/70.41	17.35%/18.75 %	56.86/90.81	0.3321	0.627 4

^aRecorded at 10 mA/cm².^bMaximum current efficiency.^cMaximum EQE.^dMaximum power efficiency.^eCommission Internationale de L'Eclairage (CIE) coordinates measured at 10 mA/cm².

In Fig.9 and Fig.6, higher efficiency at 10 mA/cm² were achieved in device D and F than those of the one-host corresponding devices (device A and B). All device data was concluded in Tab.6 which showed that highest efficiency of device F among all devices, indicating the combination of **p-XanCarDipha** and **CarTria** brought the better carrier balance than that of reference device G.

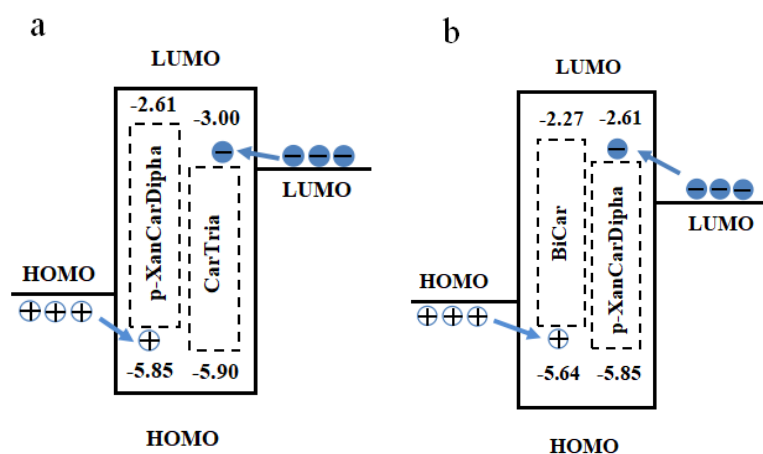


Fig.10 Schematic diagrams of the proposed charge injection into the host materials in (a) device F and (b) device E

When **p-XanCarDipha** was paired with **BiCar** (device E), the efficiency was lower than that of device B (with **p-XanCarDipha** as a single host) at 10 mA/cm. The reason of poor device performance is that the introduction of

BiCar increased the hole concentration in EML, resulting in unbalanced carriers. Therefore, the electron-type host CarTria is more suitable to be a second host combined with **p-XanCarDipha**. As a result, when **p-XanCarDipha** and **CarTria** were used as cohost in EML (device F), the electron concentration in EML increased, the carrier balance of EML was improved, and then the efficiency was increased compared with device B.

In principle, the LUMO of **p-XanCarDipha** is 2.61 eV, which is shallower than 3.0 eV of **CarTria**. When **p-XanCarDipha** was used as a single host in EML, electrons were not easily injected into EML compared with **CarTria**, causing much higher hole concentration than electron concentration in EML. However, as shown in Fig.10 (a), when **CarTria** was added to the EML, electrons were preferentially injected into the EML from **CarTria**'s LUMO level. Therefore, the electron concentration of EML increased, which improved the carrier balance and made the efficiency of device F higher than that of device B. In contrast, as shown in Fig.10(b), when **p-XanCarDipha** and **BiCar** were co-evaporated during device fabrication, holes were injected more easily than in case of device B, because of a shallower HOMO of **BiCar** (5.64 eV) than that of **p-XanCarDipha**. So that the hole concentration in the EML is much higher than that for device B which could make efficiency of device E inferior to that of device B, arising from worse carrier balance. In addition, in order to explain that the double-host system improves the carrier balance for high-efficiency green-emissive PHOLED, the normalized luminance vs operation time at a constant current density of 10 mA/cm² with double- and single-host PHOLEDs was presented in Fig.11. Obviously, the double-host PHOLEDs (device D and F) exhibit improved luminance decay characteristics compared with the single-host PHOLEDs (device A and B).

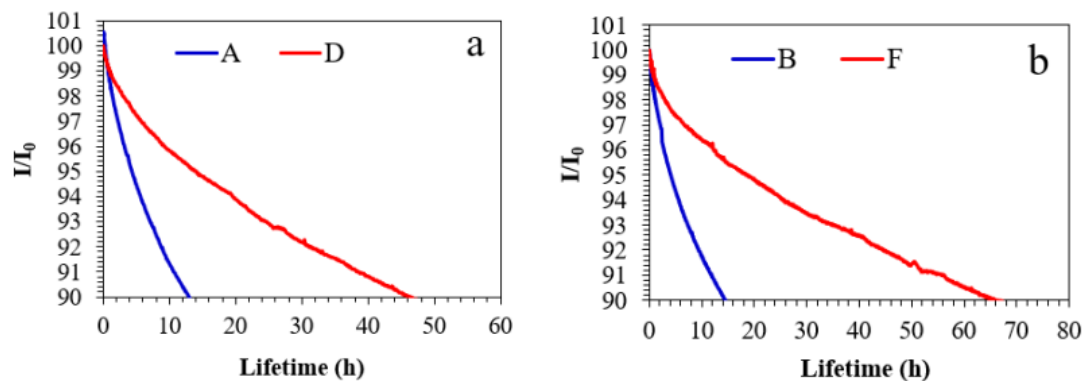


Fig.11 (a) The operational lifetimes of device A and D. (b) The operational lifetimes of device B and F. Where “I” refer to measured luminance and “ I_0 ” refer to initial luminance. All operational lifetimes of PHOLEDs were measured the luminance intensity drops to 90% of the initial value under current density at 10 mA/cm².

IV. Conclusion

Three novel green-emission hosts, **XanCarDipha**, ***p*-XanCarDipha** and ***m*-XanCarDipha**, were designed and synthesized. Furthermore, OLED devices were designed, fabricated, and measured. The efficiency curves of **XanCarDipha** and ***p*-XanCarDipha** show significant differences via combining carbazole and xanthone units with different connecting ways. In addition, ***p*-XanCarDipha: CarTria: Ir(ppy)₃ = 44:44:12 wt%** was optimized as the emitting layer to obtain a maximum EQE of 20.93%. Compared with single-host EQE (16.86%) of ***p*-XanCarDipha** (device B), the efficiency of device F has been significantly improved. The main reason is that the combination of ***p*-XanCarDipha** and **CarTria** can improve the carrier balance in EML via a dual-host strategy. Therefore, this type of dual hosts provides a certain reference for achieving efficient green OLEDs or other organic electronic devices.

Chapter 4 References

- (1) S. K. Jeon, H. L. Lee, K. S. Yook, and J.Y. Lee, *Adv. Mater.* 31, 1803524-20 (2019).
- (2) Y. Wada, S. Kubo, and H. Kaji, *Adv. Mater.* 22, 1705641-8 (2018).
- (3) A. Salehi, X. Fu, D. H. Shin, and F. So, *Adv. Funct. Mater.* 29, 1808803-21 (2018).
- (4) T. Matsushima, F. Bencheikh, T. Komino, M. R. Leyden, A. S. D Sandanayaka, and C. Qin, *Nature*. 572, 205-6 (2019).
- (5) M. Inoue, T. Serevicius, H. Nakanotani, K. Yoshida, T. Matsushima, and S. Juršenas, *Chem. Phys. Lett.* 644, 62-67 (2016).
- (6) D. H. Kim, K. Inada, L. Zhao, T. Komino, N. Matsumoto, and J. C. Ribierre, *J. Mater. Chem. C* 5, 1216-1223 (2017).
- (7) A. Salehi, X. Fu, D. H. Shin, and F. So, *Adv. Funct. Mater.* 29, 1808803-21 (2019).
- (8) Y. Im, S. Y. Byun, J. H. Kim, D. R. Lee, C. S. Oh, and K. S. Yook, *Adv. Funct. Mater.* 27, 1603007-24 (2017).
- (9) Y. Tao, C. Yang, and J. Qin, *Chem. Soc. Rev.* 40, 2943-70 (2011).
- (10) C. Murawski, K. Leo, and M. C. Gather, *Adv. Mater.* 25, 6801-27 (2013).
- (11) Z. Yin, R. Liu, C. Li, T. Masayuki, C. Liu, and X. Jin, *Dyes. Pigments*. 122, 59-65 (2015).
- (12) B. W. D'Andrade, and S. R. Forrest, *Adv. Mater.* 16, 1585-95 (2004).
- (13) Z. Yu, H. Feng, J. Zhang, S. Liu, Y. Zhao, and L. Zhang, *J. Mater. Chem. C* 7, 9301-7 (2019).
- (14) M. Idris, C. Coburn, T. Fleetham, G. J. Milam, P. I. Djurovich, S. R. Forrest, and M. Thompson, *Mater. Horiz.* 6, 1179-86 (2019).
- (15) B. Jia, H. Lian, T. Sun, J. Wei, J. Yang, and H. Zhou, *Dyes. Pigments*. 168, 212-218 (2019).
- (16) A. Ligthart, X. D. Vries, L. Zhang, M. C. W. M. Pols, P. A. Bobbert, and H. V. Eersel, *Adv. Funct. Mater.* 28, 1804618-10 (2018).
- (17) S. Hu, J. Zeng, X. Zhu, J. Guo, S. Chen, and Z. Zhao, *ACS. Appl. Mater. Inter.* 11, 27134-44 (2019).

- (18) B. Jia, H. Lian, T. Sun, J. Wei, J. Yang, and H. Zhou, *Dyes. Pigments*. 168, 212-8 (2019).
- (19) Q. Ran, Y. L. Zhang, X. Hua, M. K. Fung, L. S. Liao, and J. Fan, *Dyes. Pigments*. 162, 632-9 (2019).
- (20) Z. Zhang, J. Xie, Z. Wang, B. Shen, H. Wang, and M. Li, *J. Mater. Chem. C*. 4, 4226–35 (2016).
- (21) F. Dumur, L. Beouch, S. Peralta, G. Wantz, F. Goubard, and D. Gigmes, *Org. Electron*. 25, 21-30 (2015).
- (22) J. S. Swensen, E. Polikarpov, A. V. Ruden, L. Wang, S. Linda, and A. B. Padmaperuma, *Adv. Funct. Mater.* 21, 3250-8 (2011).
- (23) C. Y. Yang, H. J. Jang, K. H. Lee, S. Y. Byeon, J. Y. Lee, and H. Jeong, *SID. Symp. Dig. Tech. Pap.* 50, 141–44 (2019).
- (24) S. Wang, C. W. Lee, J. Y. Lee, and S. H. Hwang, *New. J. Chem.* 42, 5059-65 (2018).
- (25) X. L. Yang, G. J. Zhou, and W. Y. Wong, *Chem. Soc. Rev.* 44, 8484-575 (2015).
- (26) D. Zhang, L. Duan, D. Zhang, and Y. Qiu, *J. Mater. Chem. C*. 2, 8983-9 (2014).
- (27) D. Zhang, L. Duan, D. Zhang, J. Qiao, G. Dong, and L. Wang, *Org. Electron*. 14, 260–6 (2013).
- (28) H. Sasabe, N. Toyota, H. Nakanishi, T. Ishizaka, Y. J. Pu, J. Kido. *Adv. Mater.* 24, 3212–17 (2012).
- (29) T. Tsuzuki, and S. Tokito, *Adv. Mater.* 19, 276-280 (2007).
- (30) D. Zhang, L. Duan, Y. Li, H. Li, Z. Bin, and D. Zhang, *Adv. Funct. Mater.* 24, 3551–61 (2014).
- (31) D. Zhang, M. Cai, Z. Bin, Y. Zhang, D. Zhang, and L. Duan, *Chem. Sci.* 7, 3355–63 (2016).
- (32) T. Xu, Y. X. Zhang, C. C. Huang, J. G. Zhou, and M. K. Fung, *J. Lumin.* 206, 554-9 (2018).
- (33) X. Cai, R. Liu, H. Shi, C. Li, and H. Zhu, *Dyes. Pigments*. 143, 196-202 (2017).
- (34) Y. Chen, J. Chen, Y. Zhao, and D. Ma, *Appl. Phys. Lett.* 100, 213301-4 (2012).
- (35) M. M. Christel, *J. Phys. Chem. C*. 120, 3715-21, (2016).

- (36) H. J. Pownall, and J. R. Huber, *J. Am. Chem. Soc.* 93, 6429–36, (1971).
- (37) Nakanotani, T. Higuchi, T. Furukawa, K. Masui, K. Morimoto, and M. Numata, *Nat. Commun.* 5, 4016-7 (2014).
- (38) Y. Geng, L. S. Cui, J. U. Kim, H. Nakanotani, and C. Adachi, *Chem. Lett.* 46, 1490-1492 (2017).
- (39) C. H Chang, M. C Kuo, W. C Lin, Y. T. Chen, K. T. Wong, S.H Chou, E. Monda. R. C. Kwong, S. Xia, T. Nakagawad and C. Adachid, *J. Mater. Chem.*, 22, 3832–3838 (2012).
- (40) W. Y. Hung, P. Y. Chiang, S. W. Lin, W. C. Tang, Y. T. Chen, and S. H. Liu, *ACS. appl. Mater. Inter.* 8, 4811–18 (2016).
- (41) K. Kanakarajan, A. W. Czarnik, *J. Org. Chem.* 51, 5241–43 (1986).
- (42) G. W. Kim, W. S. Jeon, Y. H. Son, J. H. Kwon, and S. H. Jung, *Mol. Cryst. Liq. Cryst.* 565, 14–21 (2012).
- (43) L. M. Jae, M. S. Yun, K. J. Taek, K. D. Sung, P. M. Jin; and J. J. Bae, *WO2018034517*. (2018).
- (44) K. Hyungsun, K. Byungku, K. Youngkwon, K. Changwoo, S. Changju, and L. Seungjae, *EP2894157*. (2018).
- (45) D. Zhang, L. Duan, C. Li, Y. Li, H. Li, and D. Zhang, *Adv. Mater.* 26, 5050–55 (2014).
- (46) S. B. Lee, S. N. Park, C. Kim, H. W. Lee, H. W. Lee, and Y. K. Kim, *Synthetic. Met.* 203, 174–179 (2015).
- (47) W. Liu, T. Liang, Q. Chen, Z. Yu, Y. Zhang, and Y. Liu, *ACS. appl. Mater. Inter.* 8, 9254–61 (2016).
- (48) T. Hofbeck, and H. Yersin, *Inorg. Chem.* 49, 9290-9 (2010).
- (49) D. Liu, M. Du, D. Chen, K. Ye, Z. Zhang, and Y. Liu, *J. Mater. Chem. C.* 3, 4394-401 (2015).
- (50) K. H. Lee, S. O. Jeon, Y. S. Chung, M. Numata, H. Lee, and E. K. Lee, *J. Mater. Chem. C.* 8, 1736-45 (2020).
- (51) W. Yuan, M. Zhang, X. Zhang, X. Cao, N. Sun, and S. Wan, *Dyes. Pigments.* 159, 151–157 (2018).
- (52) X. Cao, X. Zhang, C. Duan, H. Xu, W. Yuan, and Y. Tao, *Org. Electron.* 57, 247–25 (2018).

- (53) Y. Olivier, J. C. Sancho-García, L. Muccioli, G. D'Avino, and D. Beljonne, *J. Phys. Chem. Lett.* 9, 6149-63 (2018).
- (54) Y. Olivier, B. Yurash, L. Muccioli, G. D'Avino, O. Mikhnenko, and J. C. Sancho-García, *Phys. Rev. Mater.* 1, 75602 (2017).
- (55) R. Gómez-Bombarelli, J. Aguilera-Iparraguirre, T. D. Hirzel, D. Duvenaud, D. Maclaurin, and M. A. Blood-Forsythe, *Nat. Mater.* 15, 1120-27 (2016).
- (56) X. Liu, Z. Chen, C. Zheng, C. Liu, C. Lee, and F. Li, *Adv. Mater.* 27, 2378-83 (2015).
- (57) K. Brunner, A. Dijken, H. Borner, J. Bastiaansen, N. Kiggen, B. Langeveld, *J. Am. Chem. Soc.* 126, :6035-42 (2004).
- (58) W. Jiang, L. Duan, J. Qiao, G. Dong, D. Zhang, and L. Wang, *J. Mater. Chem.* 21, 4918-26 (2011).
- (59) K. Wu, T. Zhang, L. Zhan, C. Zhong, S. Gong, and Z. H. Lu, *Adv. Opt. Mater.* 4, 1558-66 (2016).
- (60) M. H. Tsai, Y. H. Hong, C. H. Chang, H. C. Su, C. C. Wu, and A. Matoliukstyte, *Adv. Mater.* 19, 862-6 (2007).
- (61) Y. Tao, K. Yuan, T. Chen, P. Xu, H. Li, and R. Chen, *Adv. Mater.* 26, 7931-58 (2014).
- (62) Y. Luo, and H. Aziz, *Adv. Funct. Mater.* 20, 1285-1293 (2010).
- (63) J. H. Jeon, N. J. Lee, J. H. Lee, and M. C. Suh, *Dyes. Pigments.* 111, 116-23 (2014).
- (64) L. S. Cui, J. U. Kim, H. Nomura, H. Nakanotani, and C. Adachi, *Angew. Chem. Int. Ed.* 128, 6978-82 (2016).
- (65) P. S. Cho, G. W. Kang, E. S. Kang, Y. H. Kim, H. Kim, and Y. T. Yang, *US10050212* (2018).
- (66) E. S. Kang, S. H. Mim, Y. K. Kim, Y. H. Kim, Y. T. Yang, and E. S. Yu, *EP3032606* (2016).
- (67) D. Zhang, J. Qiao, D. Zhang, and L. Duan, *Adv. Mater.* 29, 1702847-8 (2017).
- (68) D. Zhang, L. Duan, D. Zhang, and Y. Qiu, *J. Mater. Chem. C.* 2, 8983-9 (2014).

Appendix

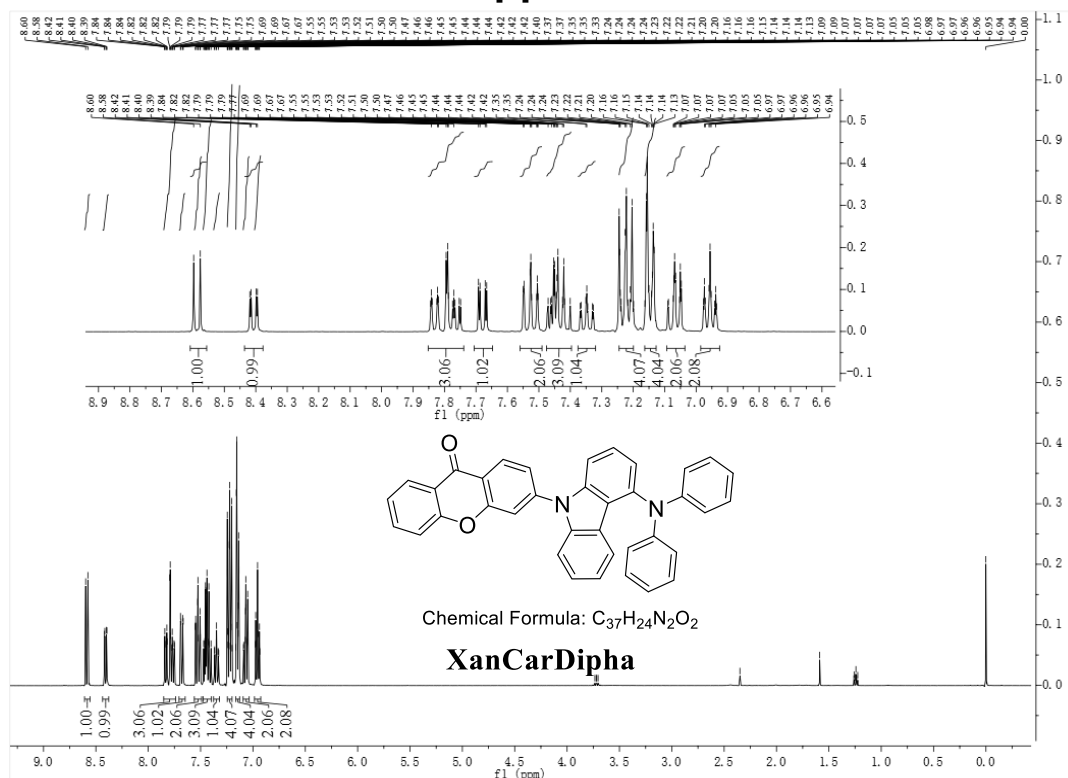


Fig.S1 1H NMR spectrum of XanCarDipha

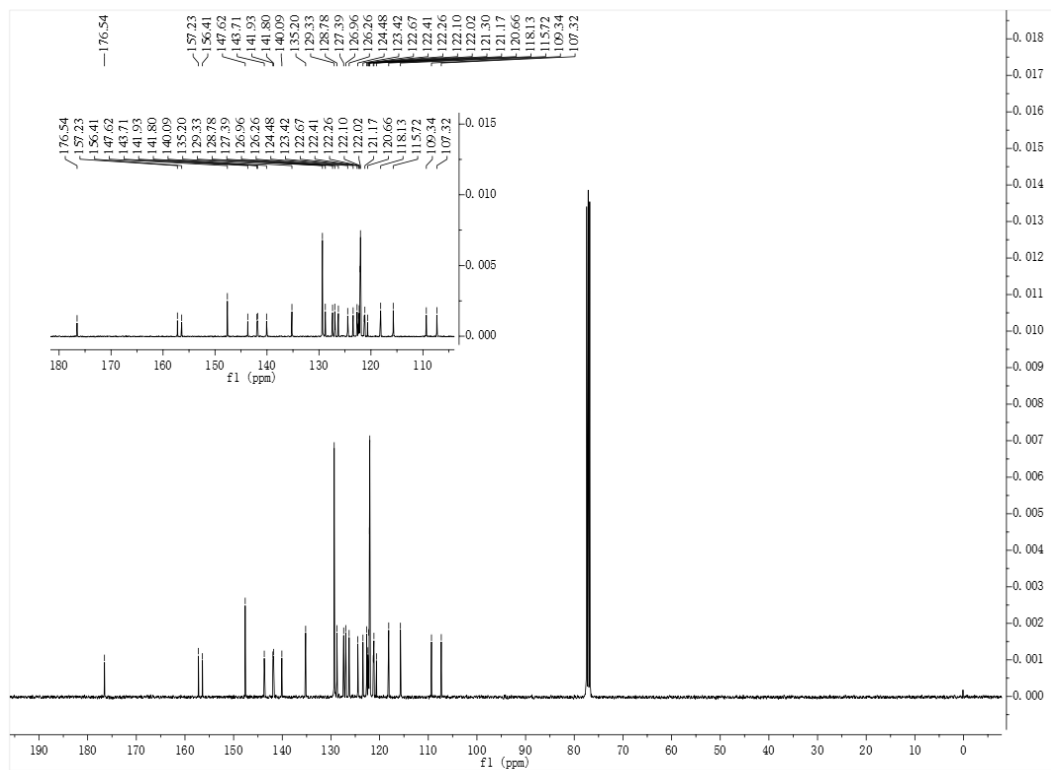


Fig.S2 ^{13}C NMR spectrum of XanCarDipha

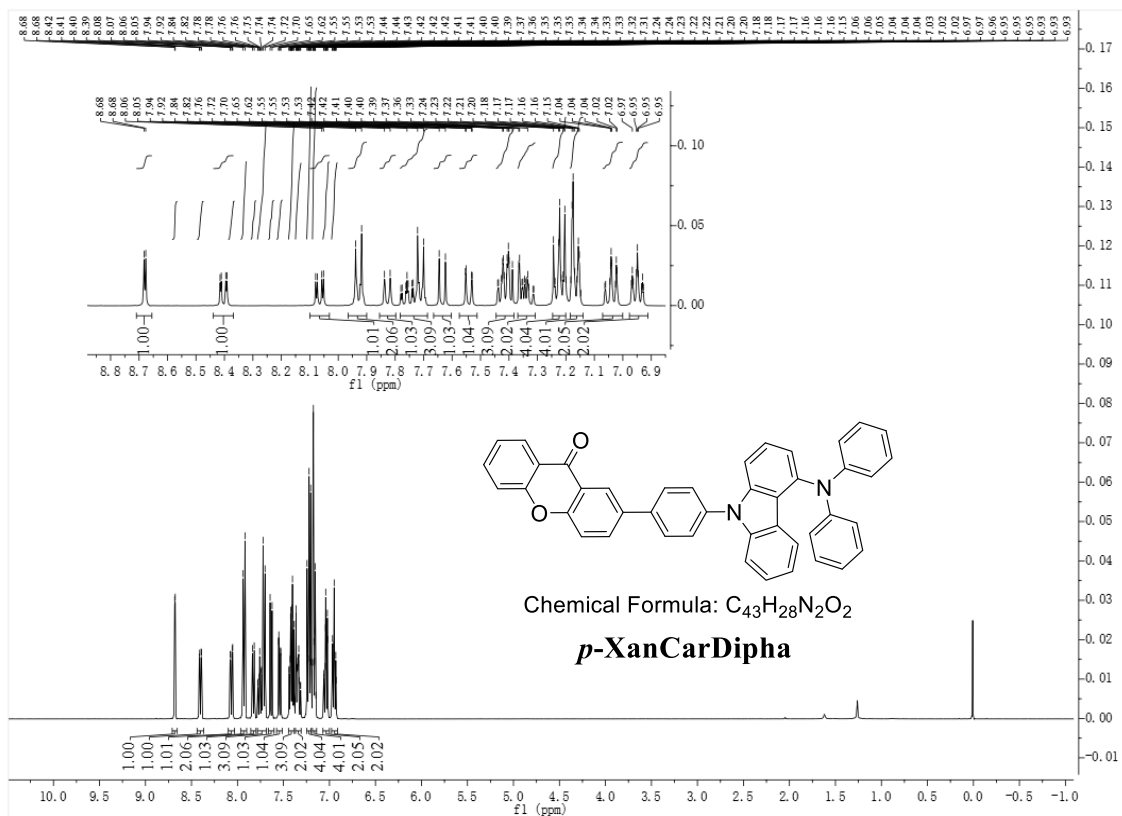


Fig.S3 1H NMR spectrum of *p*-XanCarDipa

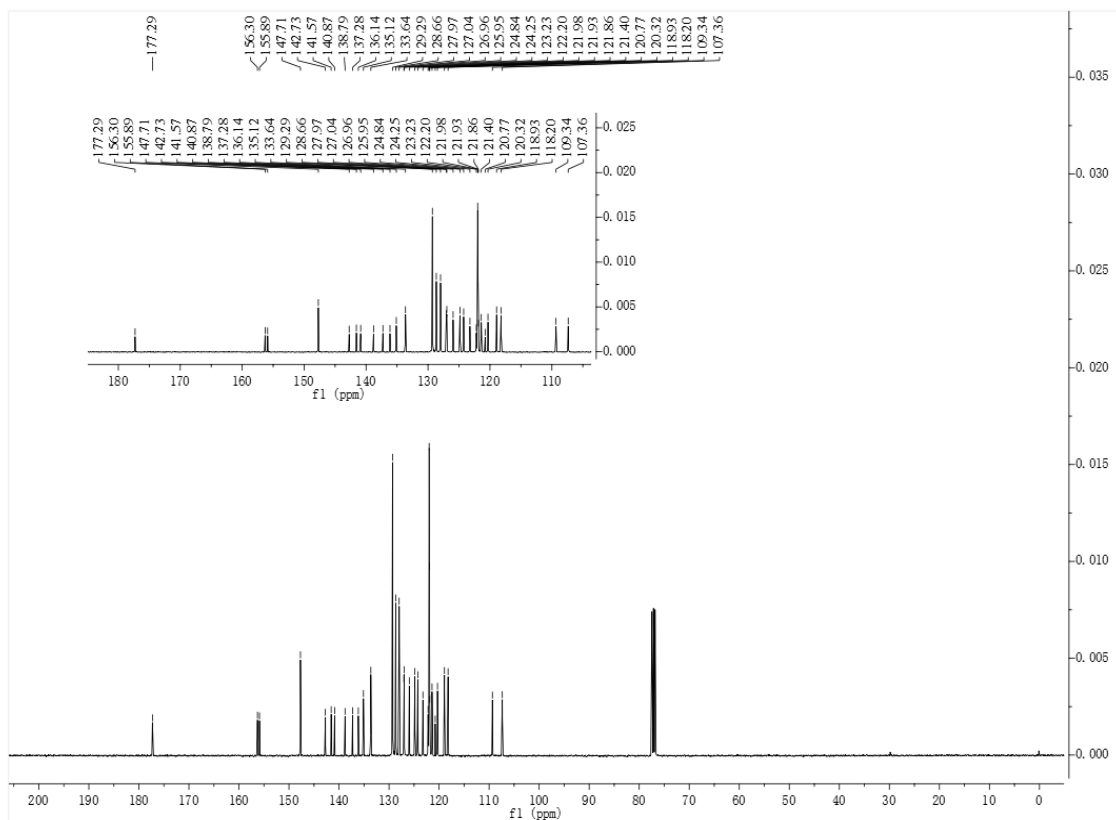


Fig.S4 ^{13}C NMR spectrum of *p*-XanCarDipa

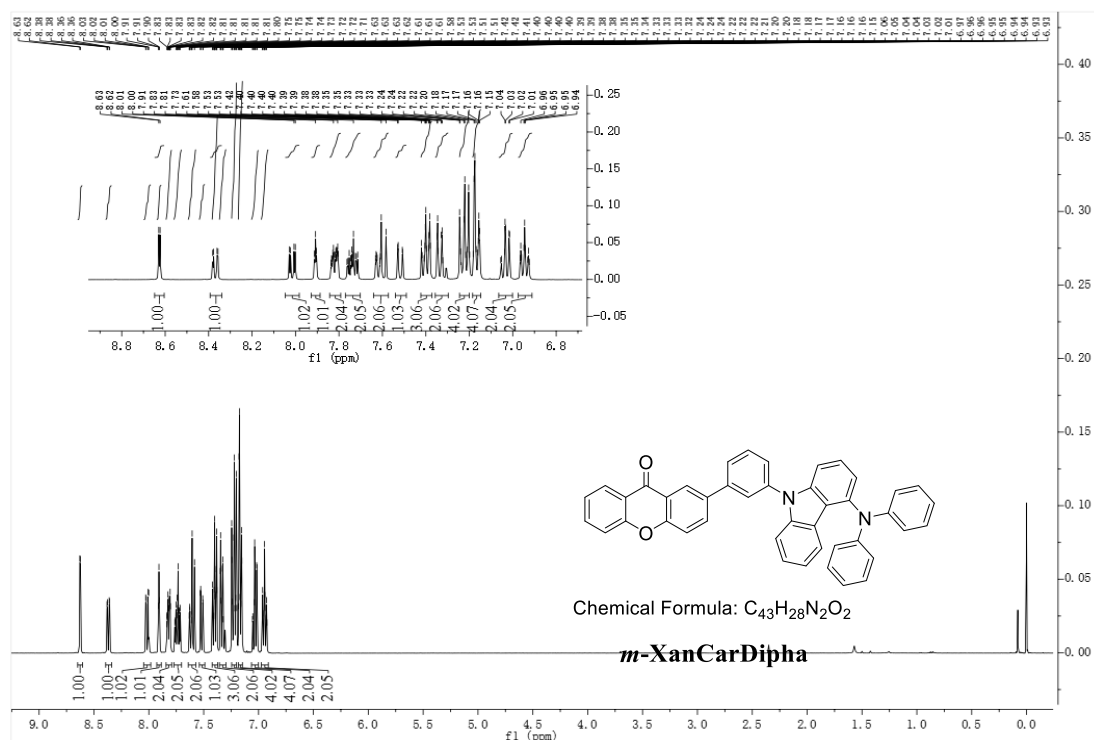


Fig.S5 1H NMR spectrum of *m*-XanCarDipa

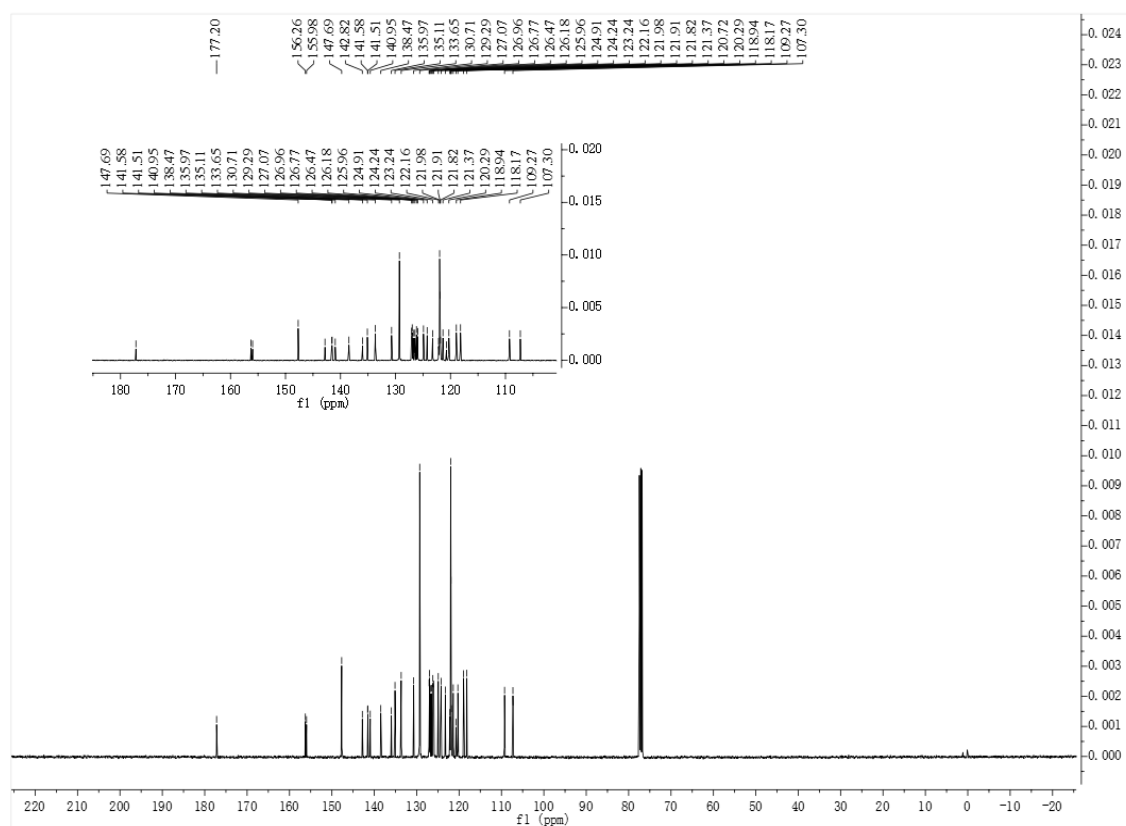
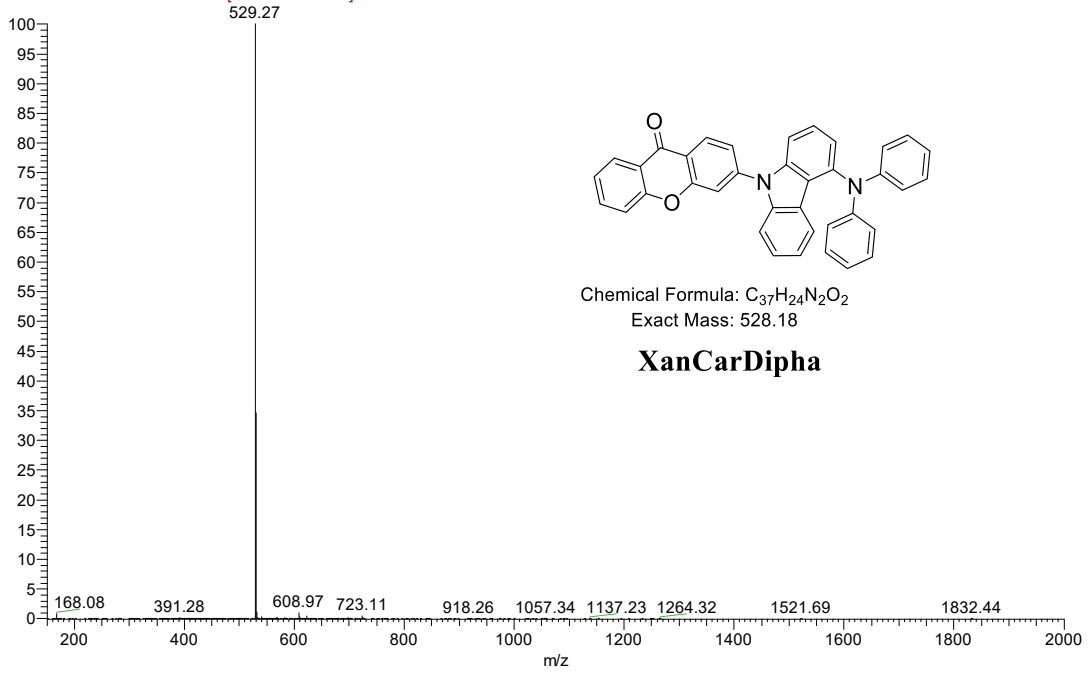


Fig.S6 ^{13}C NMR spectrum of *m*-XanCarDipa

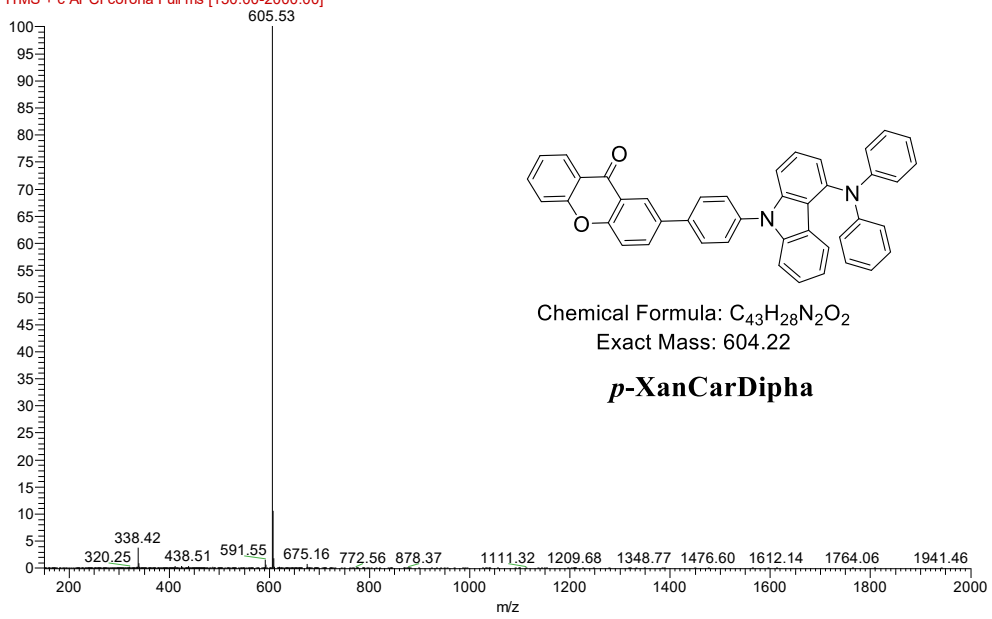
[261-KZHJ180-9H- #1896-1914 RT: 18.96-19.12 AV: 9 SB: 165 4.25-7.55 NL: 2.20E6
F: ITMS + c APCI corona Full ms [150.00-2000.00]

Relative Abundance



[253-1804271132 #18-34 RT: 0.19-0.33 AV: 8 SB: 8 0.00-0.15 NL: 2.25E5
F: ITMS + c APCI corona Full ms [150.00-2000.00]

Relative Abundance



I255-20180411 #16-30 RT: 0.17-0.29 AV: 7 SB: 7 0.00-0.13 NL: 4.11E4
F: ITMS + c APCI corona Full ms [150.00-2000.00]

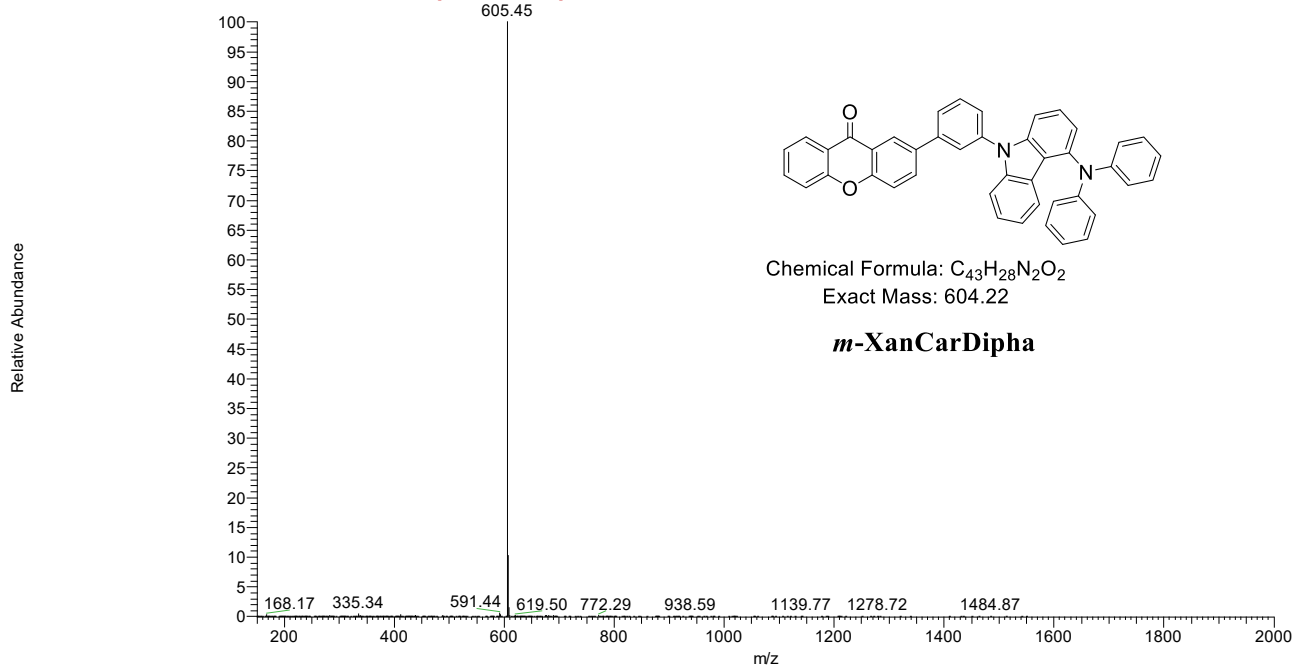


Fig.S7 MS spectrum [M+H]⁺ of XanCarDipha, *p*-XanCarDipha and *m*-XanCarDipha

Chapter 5 High-refractive-index capping layer improves top-light-emitting device performance

- I . Research background of capping layer materials
- II. Experiment content
 - II-1. Materials and measurements
 - II-2. Synthesis and characterizations
 - II-3. Fabrication and electroluminescence measurement of TEOLEDs
- III. Results and discussion
 - III-1. Photophysical properties
 - III-2. Thermal performances
 - III-3. Electroluminescence characteristics
- IV. Conclusion

I . Research background of capping layer materials

After more than 30 years of research and development, OLEDs (organic light emitting diode) have been applied in display and lighting ⁽¹⁻⁸⁾. However, due to the huge gap between external quantum efficiency (EQE) and internal quantum efficiency (IQE), the development of OLED has been greatly restricted. Therefore, it has become the research objective to study the methods to improve the light extraction efficiency ^(9,10). OLEDs can be divided into bottom emitting device (BEOLED) and top emitting device (TEOLED). The opening rate of BEOLED is as low as 30% to 50%. In TEOLED, the light emitted from the top cathode is not affected by the bottom drive panel. Therefore, TEOLED can theoretically have 100% opening ratio. Therefore, it is beneficial to obtain organic light emitting devices with high brightness and high resolution and integrate them with the bottom drive circuit. TEOLED can be manufactured on opaque substrate, which has advantages for optoelectronic integrated devices, and can realize all-transparent high-end OLED display technology.^(11,12)

The research of TEOLED mainly focus on three fields. The first, is the research on the cathode performance of TEOLED.⁽¹³⁻¹⁹⁾ As far as the structure of TEOLED is concerned, the structure of its organic functional layer is the same as BEOLED except that the electrodes are different from that of BEOLED. Therefore, it is an important direction for researchers to improve the performance of TEOLED by improving the cathode. In 2019, the Kwon group produced a multilayer translucent cathode structure by sandwiching a thin silver (Ag) layer between the new organic wetting inducer and the capping layer 1,4-bis (2-phenyl-1,10-phenanthroline-4-yl) benzene (p-bPPhenB). They obtained an electro-optically efficient and stable semitransparent pristine thin Ag cathode, and achieve a high performance TEOLED, because of the cathode weak absorption capacity and good electron injection ⁽¹⁹⁾. The second, to use some metals with low absorptivity and high reflectivity as bottom anodes for TEOLEDs.^(20,21) Use high reflectivity metal anode and study its influence on the device performance are also the research hotspots. Reflectivity and work function are two factors that TEOLED anodes should be considered. Ag and Al are widely used as metal anodes. Their reflectivity are 90% in the visible band.

However, the work functions of Ag and Al are very low, that they are not suitable for hole injection. ITO has a high work function, so double anode structures such as Al / ITO, Ag / ITO, or hole injection layer such as MoO₃ can be used to improve the hole injection ability and reduce the device driving voltage.^(20,21) The third, improve the device performance based on the microcavity theory. In order to improve the photoelectric efficiency and color purity, TEOLED with two metallic electrodes utilizing strong micro-cavity resonance has been widely used.⁽²²⁻²⁹⁾ Although the microcavity effect can improve the photoelectric efficiency and color purity, it causes color shift at large viewing angle. Due to Fabry Perot resonance, there are inevitable trade-offs between photoelectric efficiency, color purity and angular color shift.⁽²²⁾ Wu group proved the relationship among optical efficiency, color purity and angle color deviation by experiments, and obtained Pareto front by simulation. Each point on Pareto Front provides the solution. It describes the weakest color shift $\Delta\mu'v'max$ that they can obtain without sacrificing EQE and color gamut. The geometry of the Pareto Front surface reveals the inherent balance between photoelectric efficiency, color purity and angular color shift. The best solution can be selected according to different application requirements.⁽²²⁾

Optical energy losses in TEOLED includes surface plasmon polaron, waveguide mode and absorption.^(9,30-34) It has been reported that there are many ways to adjust the optical properties of TEOLEDs.⁽³⁵⁻³⁸⁾ particularly, by affecting the microcavity effect of TEOLED, an index matching capping layer (CPL) on the cathode is an effective way to improve the optical properties.⁽²⁴⁻²⁷⁾ In general, the high refractive index of the capping layer material improves the ability to modify the optical properties, thus improving the emission efficiency and reducing the angle dependence.⁽²⁸⁻²⁹⁾ With the increase of the refractive index of CPL material, the light energy loss in TEOLED can be more coupled out by affecting the microcavity effect of the device, and the ability to change the optical characteristics of the device is stronger.^(28-29,39) In 2011, Wang group used Alq₃ (n = 1.7), TPD (n = 1.9) and MoO₃ (n = 2.1) as capping layer materials. The power efficiency of device was 1.4, 1.7 and 2.5 times enhanced when 45 nm Alq₃, MnO₃ and TPD capping layer was added.⁽²⁹⁾ The improvement of OLED efficiency through the capping layer can be attributed to

the redistribution of emission light and the improvement of outcoupling efficiency caused by the optical structure (by affecting the microcavity effect of TEOLED) modified by the capping layer.⁽³⁹⁾ However, the reported CPL materials are mainly concentrated in inorganic materials. The evaporation temperature of inorganic materials is too high, which is unacceptable in practical application. Therefore, organic materials are expected to be ideal CPL materials. However, the reported refractive index (n) of CPL organic materials is less than 2.0⁽²¹⁻²⁸⁾, which cannot effectively improve the light outcoupling efficiency and color purity. Therefore, finding organic materials with good thermal stability, high refractive index and no absorption in the visible band has become a research hotspot.

Here, organic materials with the highest refractive index were found. The effects of capping layer materials with different refractive index on the performance of TEOLEDs were studied. According to the reports, the planarity of molecules will positively affect the optical performance of OLEDs, because in the amorphous film, the better the molecular planarity is, the higher the refractive index of thin film is. The thin film of high refractive index is conducive to high light extraction coupling efficiency of OLED devices.⁽²⁹⁾ To be specific, N⁴,N⁴,N^{4'},N^{4'}-tetra((1,1'-biphenyl)-4-yl)-(1,1'-biphenyl)-4,4'-diamine (**CPL-ref**), 2,2'-((6-((1,1'-biphenyl)-4-yl)-1,3,5-triazine-2,4-diyl)bis(4,1-phenylene))bis(1-phenyl-1H-benzo(d)imidazole) (**CPL-1**) and 2,2'-((6-(9-phenyl-9H-carbazol-3-yl)-1,3,5-triazine-2,4-diyl) bis(4,1-phenylene))bis(benzo(d)oxazole) (**CPL-2**) were used as the capping materials. **CPL-ref** was used as a hole transport material originally. Because its refractive index is higher than that of CPL organic material reported in literature⁽²⁴⁻²⁹⁾, the author used it as reference material.

II. Experiment content

II-1. Materials and measurements

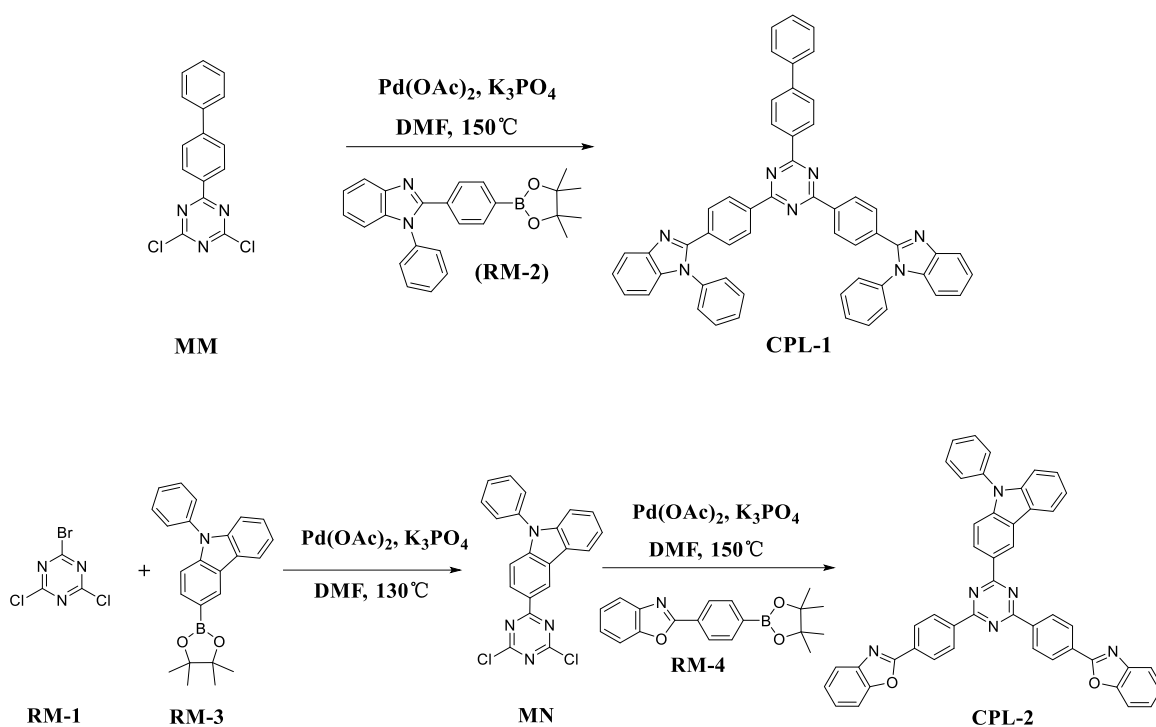
N⁴,N⁴,N^{4'},N^{4'}-tetra([1,1'-biphenyl]-4-yl)-(1,1'-biphenyl)-4,4'-diamine (**DBTBD**), 4,4',4''-((1E,1'E,1"E)-cyclopropane-1,2,3-triylidenetris(cyanomethanylylidene))tris(2,3,5,6-tetrafluorobenzonitrile) (**ECTFCN**),

N,N-bis(4-(dibenzo(b,d)furan-4-yl)phenyl)-[1,1':4',1''-terphenyl]-4-amine (**BFTA**), 9-(naphthalen-1-yl)-10-(4-(naphthalen-2-yl)phenyl)anthracene (**NAPA**), N¹,N⁶-bis(dibenzo(b,d)furan-4-yl)-3, 8-diisopropyl-N¹,N⁶-bis (4-isopropylphenyl) pyrene-1,6-diamine(**NFDIP**), 2-(4-(9,10-di(naphthalen-2-yl) anthracen-2-yl) phenyl)-1-phenyl-1*H*-benzo(d)imidazole (**NAPI**), 8-hydroxyquinolinolato-lithium (LiQ), Magnesium (Mg), Argentum (**Ag**), Ytterbium (**Yb**), N⁴,N^{4'}-diphenyl-N⁴,N^{4'}-bis(9-phenyl-9*H*-carbazol-3-yl)-(1,1'-biphenyl)-4,4'-diamine(**CPL-ref**), 2-bromo-4,6-dichloro-1,3,5-triazine, (**RM-1**), 1-phenyl-2-(4-(4,4,5,5-tetramethyl-1,3,2-dioxaborolan-2-yl)phenyl)-1*H*-benzo[d]imidazole(**RM-2**), 9-phenyl-3-(4,4,5,5-tetramethyl-1,3,2-dioxaborolan-2-yl)-9*H*-carbazole(**RM-3**), 2-((1,1'-biphenyl)-4-yl)-4,6-dichloro-1,3,5-triazine(**MM**), 2-(4-(4,4,5,5-tetramethyl-1,3,2-dioxaborolan-2-yl)phenyl)benzo[d]oxazole(**RM-4**), Palladium(II) acetate (Pd(OAc)₂), Potassium phosphate (K₃PO₄) and N,N-Dimethylformamide (DMF) were commercially available.

Refractive indices (n) and Extinction coefficients (k) were measured by an alpha-SE ellipsometry (J.A.Woollam). Ultraviolet-visible (UV-Vis) absorption and transmission spectra were obtained on a HP-8453 UV/Vis/NIR spectrophotometer (Agilent) with a 1 cm quartz cell. Photoluminescence (PL) spectra were obtained by a LS-55 spectrofluorometer (Perkin-Elmer) at room temperature. Both differential scanning calorimetry (DSC), on a DSC-60, and thermo-gravimetric analysis (TGA), on a Tg 209-F3, were performed under nitrogen atmosphere at a heating rate of 10°C/min. All materials for TEOLED fabrication were 99.9% purity via vacuum sublimation, and were identified via high-performance liquid chromatography (HPLC).

II-2. Synthesis and characterizations

The synthesis routes for CPL-1 and CPL-2 are depicted in Scheme 1.



Scheme 1 Synthesis of **CPL-1** and **CPL-2**.

II-2-1. Synthesis of CPL-1

MM (1.51g, 5mmol), **RM-2** (4.75g, 12mmol), Pd(OAc)₂ (0.11g, 0.5mmol), K₃PO₄ (2.54g, 12mmol) and dimethylformamide (DMF, 100ml) were stirred in a 250 mL three-necked flask under nitrogen for 10 h at 150°C. After cooling to room temperature, the solution was extracted with ethyl acetate and distilled water. The organic layer was dried over anhydrous MgSO₄ and rotary evaporated. The resulting residue was purified via column chromatography to yield a white powder CPL-1 (2.84 g, 83%, HPLC 98.5%). ¹H NMR (400 MHz, THF-d₈) δ 8.79 – 8.71 (m, 2H), 8.67 – 8.60 (m, 4H), 7.82 – 7.73 (m, 8H), 7.71 – 7.65 (m, 2H), 7.59 – 7.47 (m, 6H), 7.42 (ddq, 6H), 7.33 (t, 1H), 7.29 – 7.14 (m, 6H). LC-MS (m/z): 770.79 (M)⁺. Elemental analysis (C₅₃H₃₅N₇): C, 82.65%; H, 4.57%; N, 12.78%.

Synthesis of 3-(4,6-dichloro-1,3,5-triazin-2-yl)-9-phenyl-9H-carbazole (MN).

2-bromo-4,6-dichloro-1,3,5-triazine (1.14g, 5mmol), 9-phenyl-3-(4,4,5,5-tetramethyl-1,3,2-dioxaborolan-2-yl)-9H-carbazole (4.43g, 12mmol), Pd(OAc)₂ (0.11g, 0.5mmol), K₃PO₄ (2.54g, 12mmol) and DMF (100ml) were stirred in a 250-ml three-necked flask under nitrogen for 12 h at 130 °C. After cooling to

room temperature, the solution was extracted with ethyl acetate and distilled water. The organic layer was dried over anhydrous MgSO_4 and rotary evaporated. The resulting residue was purified via column chromatography to yield a white powder **MN** (1.67 g, 85.5%, HPLC 99.0%). ^1H NMR (400 MHz, Chloroform- d) δ 9.29 – 9.24 (m, 1H), 8.49 (dd, 1H), 8.23 (dt, 1H), 7.64 (td, 2H), 7.59 – 7.49 (m, 3H), 7.45 (ddd, 1H), 7.40 – 7.32 (m, 3H). Elemental analysis ($\text{C}_{21}\text{H}_{12}\text{Cl}_2\text{N}_4$): C, 64.53%; H, 3.07%; Cl, 18.14%; N, 14.26%.

II-2-2. Synthesis of CPL-2.

MN (1.90g, 5mmol), **RM-4** (3.84g, 12mmol), $\text{Pd}(\text{OAc})_2$ (0.11g, 0.5mmol), K_3PO_4 (2.54g, 12mmol) and dimethylformamide (DMF, 100ml) were stirred in a 250 mL three-necked flask under nitrogen for 10 h at 150 °C. After cooling to room temperature, the solution was extracted with ethyl acetate and distilled water. The organic layer was dried over anhydrous MgSO_4 and rotary evaporated. The resulting residue was purified via column chromatography to yield a white powder **CPL-2** (2.65 g, 75%, HPLC 98.2%), then purified to 99.9% by vacuum sublimation. ^1H NMR (400 MHz, THF- d_8) δ 9.73 (d, 1H), 9.11 – 9.00 (m, 4H), 8.96 (dd, 1H), 8.58 – 8.46 (m, 4H), 8.43 (d, 1H), 7.82 – 7.77 (m, 2H), 7.72 – 7.68 (m, 6H), 7.57 (dd, 2H), 7.44 – 7.37 (m, 7H). LC-MS (m/z): 709.38 (M) $+$. Elemental analysis ($\text{C}_{47}\text{H}_{28}\text{N}_6\text{O}_2$): C, 79.68%; H, 4.01%; N, 11.89%.

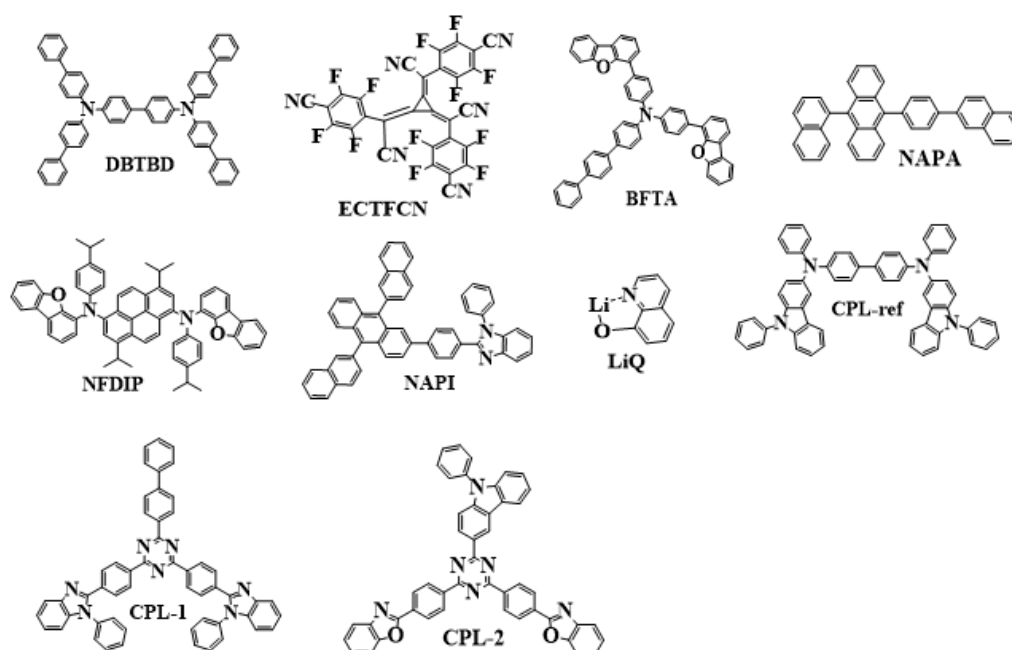


Fig.1 Molecular structure of organic compounds used in TEOLED

II-3. Fabrication and electroluminescence measurement of TEOLEDs

The molecular structures of the corresponding compounds are shown in Fig.1. Refractive index of each layer of organic materials between two electrodes at 450 nm are shown in Fig.2. The manufacturing details of TEOLED were as follows.

CPL (65nm)	
Ag:Mg (16nm)	
Yb (1.5nm)	
NAPI: LiQ (35nm)	n=1.921@450nm
NAPA: NFDIP (20nm)	n=1.946@450nm
BFTA (10nm)	n=2.099@450nm
DBTBD (x nm)	n=2.042@450nm
DBTBD: ECTFCN (10 nm)	n=1.967@450nm
Ag (100 nm)	

Fig.2 The TEOLED device structure and refractive index of each layer of organic materials between two electrodes

Device A: Ag (100 nm)/DBTBD: ECTFCN(96:4,10 nm)/DBTBD(119 nm)/BFTA (10 nm)/NAPA: NFDIP (95:5, 20 nm)/NAPI: LiQ (1:1, 35 nm)/Yb (1.5 nm)/Ag:Mg = 9:1 (16 nm)/**CPL-ref** (65 nm).

Device B: Ag (100 nm)/DBTBD: ECTFCN(96:4,10 nm)/DBTBD(123 nm)/BFTA (10 nm)/NAPA: NFDIP (95:5, 20 nm)/NAPI: LiQ (1:1, 35 nm)/Yb (1.5 nm)/Ag:Mg = 9:1 (16 nm)/**CPL-1** (65 nm).

Device C: Ag (100 nm)/DBTBD: ECTFCN(96:4,10 nm)/DBTBD(123 nm)/BFTA (10 nm)/NAPA: NFDIP (95:5, 20 nm)/NAPI: LiQ (1:1, 35nm)/Yb (1.5 nm)/Ag:Mg = 9:1 (16 nm)/**CPL-2** (65 nm).

In order to ensure that the chromaticity coordinates (CIE) of TEOLEDs were consistent, DBTBD was used to adjust the film thickness of hole transport layer. The mixed organic materials were evaporated at a rate of 1 Å/s at 4×10^{-6} Torr. It was necessary to use metal mask in the evaporation of both of cathode and anode. The area of the device was 5×5 mm². FPD (flat panel display) automatic test system (FS-1000GA4) was used to measure optical characteristics. All measurements were carried out in air at room temperature.

III. Results and discussion

III-1. Photophysical properties

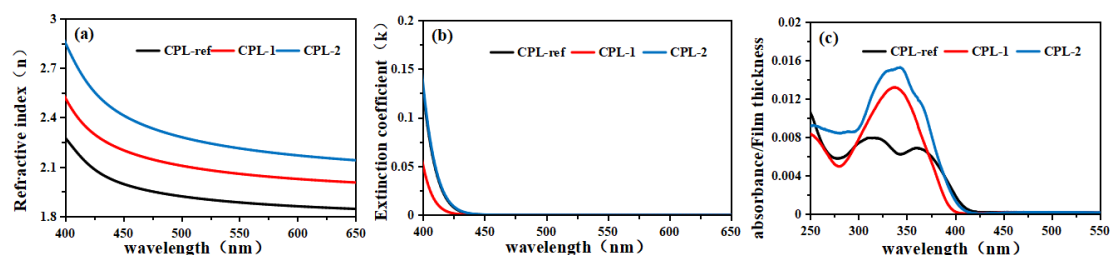


Fig.3 (a) Refractive indices (n) of **CPL-ref**, **CPL-1** and **CPL-2** measured by ellipsometer. (b) The extinction coefficients (k) of **CPL-ref**, **CPL-1** and **CPL-2** measured by ellipsometry. (c) UV absorption spectra of **CPL-ref**, **CPL-1** and **CPL-2** films with a thickness of 1 nm.

Fig.3(a) shows the relationship curves between the refractive indices (n) of **CPL-ref**, **CPL-1** and **CPL-2** with the wavelength. In the wavelength range of 400-650 nm, the refractive indices (n) of **CPL-1** and **CPL-2** were much higher than that of **CPL-Ref**, while that of **CPL-2** was the highest from the wavelength 400 nm to 650 nm. Fig.3(b) shows the relationship curves between the extinction coefficients (k) of **CPL-ref**, **CPL-1** and **CPL-2** with the wavelength. The extinction coefficients (k) of **CPL-ref** and **CPL-2** were overlapped, while those of **CPL-1** were lower. Lower K values imply weak visible UV-vis absorption. Therefore, none of three capping materials had visible ultraviolet absorption in the wavelength range of 430-650 nm. Fig.3(c) shows the UV absorption spectra of **CPL-ref**, **CPL-1** and **CPL-2** with 1-nm thick films. The absorption of **CPL-2** was the strongest at 300-400 nm, while that of **CPL-ref** was the weakest. Hence, compared with **CPL-ref**, **CPL-1** and **CPL-2** could better protect the device from UV damage.

Table 1 Refractive indices (n) and extinction coefficients (k) of **CPL-ref**, **CPL-1** and **CPL-2**







material	n@ 430nm	k@ 430nm	n@ 450nm	k@ 450nm	n@ 460nm	k@ 460nm	n@ 525nm	n@ 600nm	n@ 620nm
CPL-ref	2.061	0.0038	1.997	0.0002	1.975	0.0000	1.901	1.861	1.854
CPL-1	2.273	0.0006	2.201	0.0000	2.175	0.0000	2.080	2.027	2.017
CPL-2	2.567	0.0049	2.462	0.0002	2.424	0.0000	2.276	2.187	2.170

Table 1 sums up the refractive indices (n) and extinction coefficients (k) of **CPL-ref**, **CPL-1** and **CPL-2**. The refractive index of **CPL-1** was about 0.2 higher than that of **CPL-ref**, and that of **CPL-2** was about 0.4 higher than that of **CPL-ref**, which implied that **CPL-1** and **CPL-2** used as optical extraction materials were impactful.

III-2. Thermal performances

The thermal performances of **CPL-ref**, **CPL-1** and **CPL-2** were studied by TGA and DSC. The information generalized in Table 2. Since the glass transition temperature (T_g) of **CPL-ref** and **CPL-1** were 143.9°C and 159.6°C, respectively, it was not easy to crystallize for **CPL-ref** and **CPL-1** after film forming. As shown in Table 2, it could not be confirmed for T_g of **CPL-2**, while it was not easy to crystallize after long time heating. The thermal stabilities of **CPL-ref**, **CPL-1** and **CPL-2** were confirmed by crystallization experiments. Firstly, three groups of films were obtained on the glass substrate with evaporating the three materials respectively. The films were allowed to keep at 20°C for 1200 hours, 80°C for 1000 hours and 115 °C for 200 hours. The surface of these films which had no crystallization phenomenon were observed by the microscope, which demonstrated that thermal stabilities of all three CPL materials were outstanding. The thermal decomposition temperatures (TD, equivalent to 5% weight loss) of **CPL-ref**, **CPL-1** and **CPL-2** were 487.9°C, 527.2°C and 457.9°C respectively, which demonstrated that the three CPL materials had excellent thermal stabilities. Hence, **CPL-1** and **CPL-2** which had sufficient thermochemical stability could be applied for OLED.

Table 2 Thermal performances of CPL-ref, CPL-1 and CPL-2

Compounds	T_g (°C)	T_m (°C)	aT_d (°C)	20°C/1200h	80°C/1000h	115°C/200h
CPL-ref	143.9	b-	487.9			
CPL-1	159.6	319.3	527.2			

CPL-2

-

364.8

457.9



^a5% weight loss temperature. ^b not got. ^cthe films were kept at 20 °C for 1200 hours.

III-3. Electroluminescence characteristics

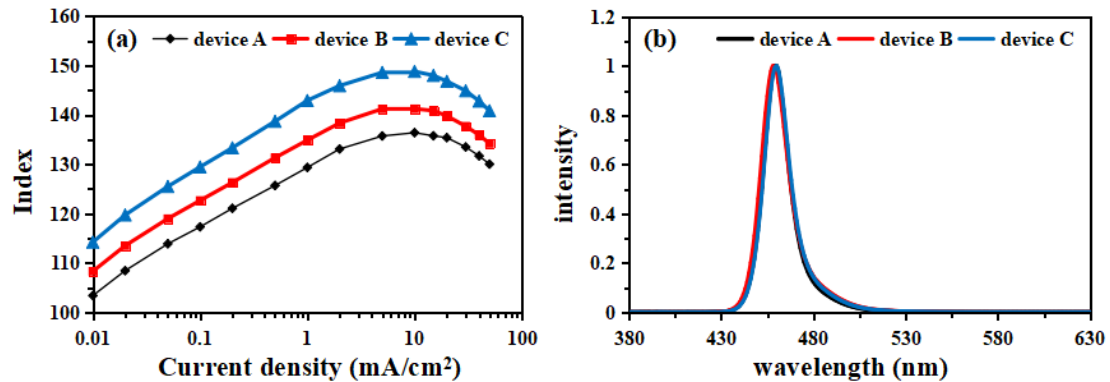


Fig.4 (a) CE-J of TEOLEDs manufactured with **CPL-ref**, **CPL-1** and **CPL-2**. Index, the ratio of current efficiency to CIEy. **(b)** The EL spectra of TEOLEDs manufactured **CPL-ref**, **CPL-1** and **CPL-2**.

Fig.4(a) shows the index, the ratio of current efficiency to CIEy, of TEOLEDs manufactured with **CPL-ref**, **CPL-1** and **CPL-2**. The peak of the index was reached with the current density at 10 mA/cm², while the index decreased with the increase of current density above 10 mA/cm². The CPL-1 device had much higher index than **CPL-ref** device, while the **CPL-2** device had much higher index than **CPL-1** device. The electroluminescence (EL) spectra of TEOLEDs manufactured with **CPL-ref**, **CPL-1** and **CPL-2** are showed in Fig.4(b). The coincidence of three curves with each other illustrated that the EL spectra was not affected with different capping materials. The electrical and optical characteristics of these devices are generalized in Table 3. Compared with the **CPL-ref** device, the **CPL-1** device had the higher index with 3.4% improvement rate, while the **CPL-2** device had the higher index with 9.1% improvement rate. The above results indicated that the index of TEOLEDs were promoted with the increase of the refractive index of the capping layer materials. Device A, device B and device C had similar voltage, indicating that Device voltage were almost free from the different refractive index of capping materials.

Table 3 Electrical and optical properties of devices at the optimum CPL film thickness

device	Current density (mA/cm ²)	Voltage (V)	Current efficiency (cd/A)	CIE _x	CIE _y	Index	EL _{peak} (nm)
device A	10	3.90	5.93	0.1400	0.0435	136.4	459
device B	10	3.89	6.43	0.1403	0.0455	141.2	458
device C	10	3.95	6.95	0.1389	0.0467	148.8	460

The angle dependent properties are illustrated in the variation of brightness and CIE. The dependence of luminance and CIE on viewing angles of 0°, 15°, 30°, 45°, 60° and 75° are showed in Fig.5. As showed in Fig.5(a,d), Compared with devices A, device B and device C had more directional emission and enhanced brightness in the range of 0-75°, resulting in improved brightness and efficiency in the forward direction. As shown in Fig.5 (b, e, c, f), the colors of devices A, B and C varied from 0° (0.140, 0.043) to 75° (0.149, 0.037), from 0° (0.140, 0.045) to 75° (0.148, 0.038) and from 0° (0.139, 0.046) to 75° (0.148, 0.037), respectively. Since the color coordinates of device A, device B and device C at 0° had some variations, the percentage change of color coordinates could be used to observe the variation tendency of color coordinates more directly. As shown in Fig.5(e, f), the color coordinates of device A, device B and device C had very small variations, indicating that the trend and amplitude of the color changes were basically identical. So we could find that the refractive index reaching a certain value ($n > 2.0$) had minor effect on the angle color shift. The above results proved that with the increase of the refractive index of the capping materials, the angle dependent properties could be optimized.

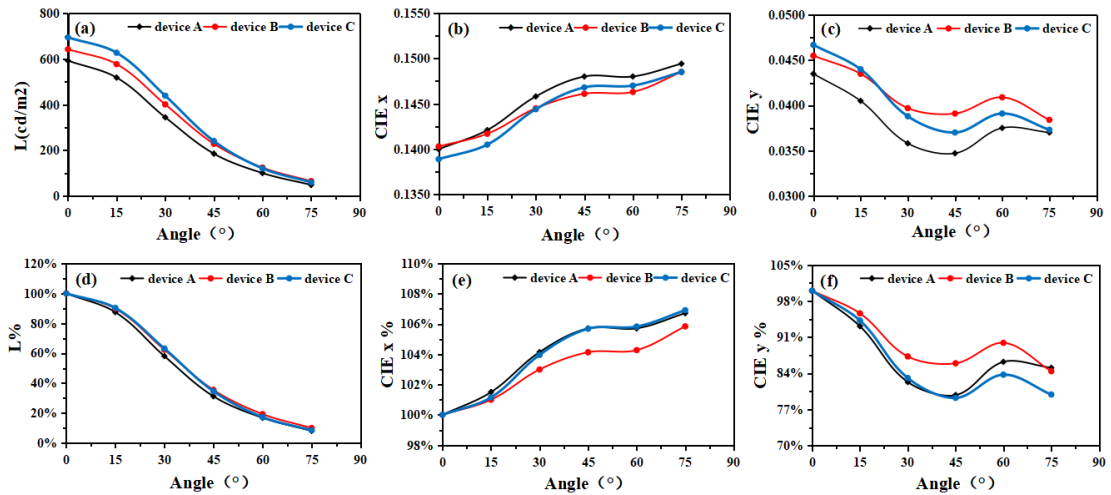


Fig.5 The angle dependence of L(a), CIE x (b), CIE y (c), L%(d), CIE x% (e) and CIE y%(f) for TEOLED manufactured with **CPL-ref** (device A), **CPL-1** (device B) and **CPL-2** (device C) at the viewing angles of 0°, 15°, 30°, 45°, 60° and 75° respectively.

As mentioned above, **CPL-1** possessed much higher refractive index than **CPL-ref** in the range of 400-650 nm, while **CPL-2** had much higher refractive index than **CPL-1** at 450-650 nm. Fig.6 proved that the reflectivity increased with the increase of refractive index, while the transmittance decreased with the increase of reflectivity. Reflectivity and transmittance have a direct influence on the microcavity effect of TEOLED. By influencing the microcavity effect of TEOLED, the capping material with the high refractive index improved the ability to optimize the optical properties for improving the emission efficiency and reducing the angle dependence. The improvement of OLED efficiency through the capping layer could be ascribed to the redistribution of emission light and the improvement of external coupling efficiency also caused by the optical structure modified by the capping layer (by influencing the microcavity effect of TEOLED).

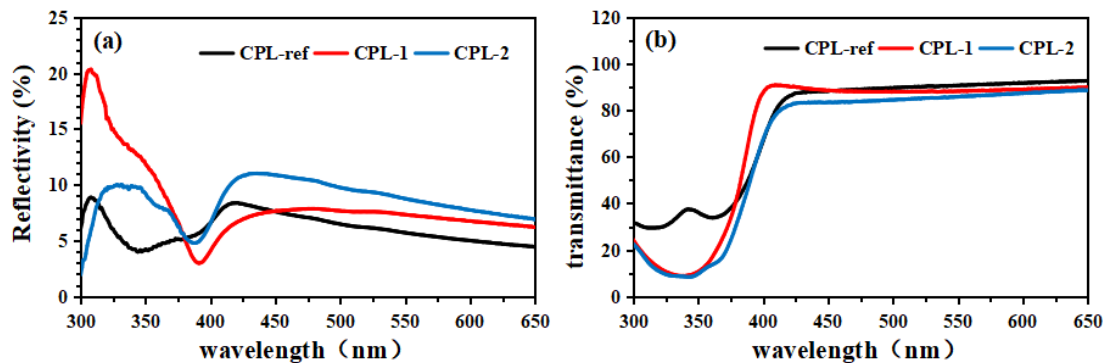


Fig.6 (a) Reflection spectra of **CPL-ref**, **CPL-1** and **CPL-2** in 65 nm thick films measured by lambda 950 UV/Vis /near-infrared spectrophotometer (PerkinElmer). (b) Transmission spectrum in the same 65 nm thick film.

IV. Conclusion

The influences of distinct capping layers on the performance of TEOLED were studied. Capping layer materials which had high refractive index could improve the brightness and power efficiency of the device in the forward direction. Compared with CPL-ref device, the light extraction efficiency (index) of **CPL-1** device and **CPL-2** device were improved by 3.4%, 9.1%, respectively. Compared with device A (**CPL-ref**), device B (**CPL-1**) and device C (**CPL-2**) showed more directional emission and higher brightness in the angle range of 0-7.5°. The colors with the viewing angle of devices A, B and C varied from 0° (0.140, 0.043) to 75° (0.149, 0.037), from 0° (0.140, 0.045) to 75° (0.148, 0.038) and from 0° (0.139, 0.046) to 75° (0.148, 0.037). This illustrated that these performances could be promoted due to the increase of the refractive index of the capping layer materials. It is necessary for more precise studies at some future time.

Chapter 5 References

- (1) M. A. Baldo, D. O'brien, Y. You, A. Shoustikov, S. Sibley, M. Thompson, and S. Forrest, *Nature*, 395, 151-154(1998).
- (2) M. Baldo, S. Lamansky, P. Burrows, M. Thompson, and S. Forrest, *Appl. Phys. Lett.*, 75, 4 (1999).
- (3) B. W. D'Andrade, M. A. Baldo, C. Adachi, J. Brooks, M. E. Thompson, and S. R. Forrest, *Appl. Phys. Lett.*, 79, 1045-1047 (2001).
- (4) M. Ikai, S. Tokito, Y. Sakamoto, T. Suzuki, and Y. Taga, *Appl. Phys. Lett.*, 79, 156-158 (2001).
- (5) L. Liao, K. Klubek, and C. Tang, *Appl. Phys. Lett.*, 84, 167 (2004).
- (6) B.W. D'Andrade, and S. R. Forrest, *Adv. Mater.*, 16, 1585-1595 (2004).
- (7) S. J. Su, E. Gonmori, H. Sasabe, and J. Kido, *Adv. Mater.*, 20, 4189-4194 (2008).
- (8) S. Reineke, F. Lindner, G. Schwartz, N. Seidler, K. Walzer, B. Lüssem, and K. Leo, *Nature*, 459, 234-238 (2009).
- (9) K. Hong, and J.-L. Lee, *Electron. Mater. Lett.*, 7, 77-91 (2011).
- (10) S. Nowy, B. C. Krummacher, J. Frischeisen, N. A. Reinke and W. Brütting, *J. Appl. Phys.*, 104, 123109 (2008).
- (11) A. Dodabalapur, L. J. Rothberg, R. H. Jordan, T. M. Miller, R. E. Slusher and Julia M. Phillips, *J. Appl. Phys.*, 80, 6954 (1996).
- (12) K. Pichler, W. E. Howard, and O. Prache, *Part of the SPIE Conference on Organic Light-Emitting Materials and Devices III*, 3797, 258-265 (1999).
- (13) M. Slocsky, and S. R. Forrest, *Appl. Phys. Lett.*, 94, 163302 (2009).
- (14) Y. Sun, and S. R. Forrest, *Nat. Photonics*, 2, 483-487 (2008).
- (15) H. Riel, S. Karg, T. Beierlein, W. Rieß, and K. Neyts, *J. Appl. Phys.*, 94, 5290-5296 (2003).
- (16) H. Riel, S. Karg, T. Beierlein, B. Ruhstaller, and W. Rieß, *Appl. Phys. Lett.*, 82, 466-468 (2003).
- (17) R. Pode, C. Lee, D. Moon, and J. Han, *Appl. Phys. Lett.*, 84, 4614-4616 (2004).
- (18) S. Han, D. Grozea, C. Huang, Z. Lu, R. Wood, and W. Kim, *J. Appl.*

- Phys.*, 96, 709-714 (2004).
- (19) S. K. Kim, R. Lampande, and J. H. Kwon, *ACS Photonics*, 6(11), 2957-2965 (2019).
- (20) S. Han, X. Feng, Z. Lu, D. Johnson, and R. Wood, *Appl. Phys. Lett.*, 82, 2715-2717 (2003).
- (21) M. H. Lu, M. S. Weaver, T. X. Zhou, M. Rothman, R. C. Kwong, M. Hack, and J. J. Brown, *Appl. Phys. Lett.*, 81(21), 3921–3923 (2002).
- (22) G. Tan, J. H. Lee, S. C. Lin, R. Zhu, S. H. Choi, and S. T. Wu, *Opt. Express*, 25, 33629-33642 (2017).
- (23) L. H. Smith, J. A. E. Wasey, and W. L. Barnes, *Appl. Phys. Lett.*, 84(16), 2986–2988 (2004).
- (24) L. S. Hung, C. W. Tang, M. G. Mason, P. Raychaudhuri and J. Madathil, *Appl. Phys. Lett.*, 78, 544-546 (2001).
- (25) S. Chen, X. Li, and W. Huang, *Org. Electron.*, 9, 1112-1117(2008).
- (26) S. Chen, R. Song, J. Wang, Z. Zhao, Z. Jie, Y. Zhao, B. Quan, W. Huang, and S. Liu, *J. Lumin.*, 128, 1143-1147 (2008).
- (27) J. Hou, J. Wu, Z. Xie, and L. Wang, *Org. Electron.*, 9, 959-963(2008).
- (28) M. Zhang, Z. Chen, L. Xiao, B. Qu and Q. Gong, *J Appl. Phys.*, 113, 113105 (2013).
- (29) Z. Wang, S. Naka, H. Okada, *Solid State Electronics*, 56(1), 155–158 (2011).
- (30) H. J. Park, D. Vak, Y. Y. Noh, B. Lim, and D. Y. Kim, *Appl. Phys. Lett.*, 90 (2007).
- (31) K. Y. Yang, K. C. Choi, and C. W. Ahn, *Opt. Express*, 17, 11495-11504 (2009).
- (32) A. Fujiki, T. Uemura, N. Zettsu, M. Akai-Kasaya, A. Saito, and Y. Kuwahara, *Appl. Phys. Lett.*, 96 (2010).
- (33) W. H. Koo, S. M. Jeong, S. Nishimura, F. Araoka, K. Ishikawa, T. Toyooka, and H. Takezoe, *Adv. Mater.*, 23, 1003-1007 (2011).
- (34) T. Tanaka, Y. Totoki, A. Fujiki, N. Zettsu, Y. Miyake, M. Akai-Kasaya, A. Saito, T. Ogawa, and Y. Kuwahara, *Appl. Phys. Express*, 4 (2011).
- (35) K. Saxena, V. Jain, and D. S. Mehta, *Opt. Mater.*, 32, 221-233 (2009).
- (36) S. Möller, and S. Forrest, *J. Appl. Phys.*, 91, 3324-3327 (2002).
- (37) K. Hong, H. K. Yu, I. Lee, K. Kim, S. Kim, and J. L. Lee, *Adv. Mater.*, 22,

4890-4894 (2010).

(38) Y. R. Do, Y. C. Kim, Y. W. Song, and Y. H. Lee, *J. Appl. Phys.*, 96, 7629-7636 (2004).

(39) Q. Huang, K. Walzer, M. Pfeiffer, K. Leo, M. Hofmann and T. Stübinger, *J Appl. Phys.*, 100, 064507 (2006).

(40) D. Yokoyama, *J. Mater. Chem.*, 21, 19187–19202 (2011).

Appendix

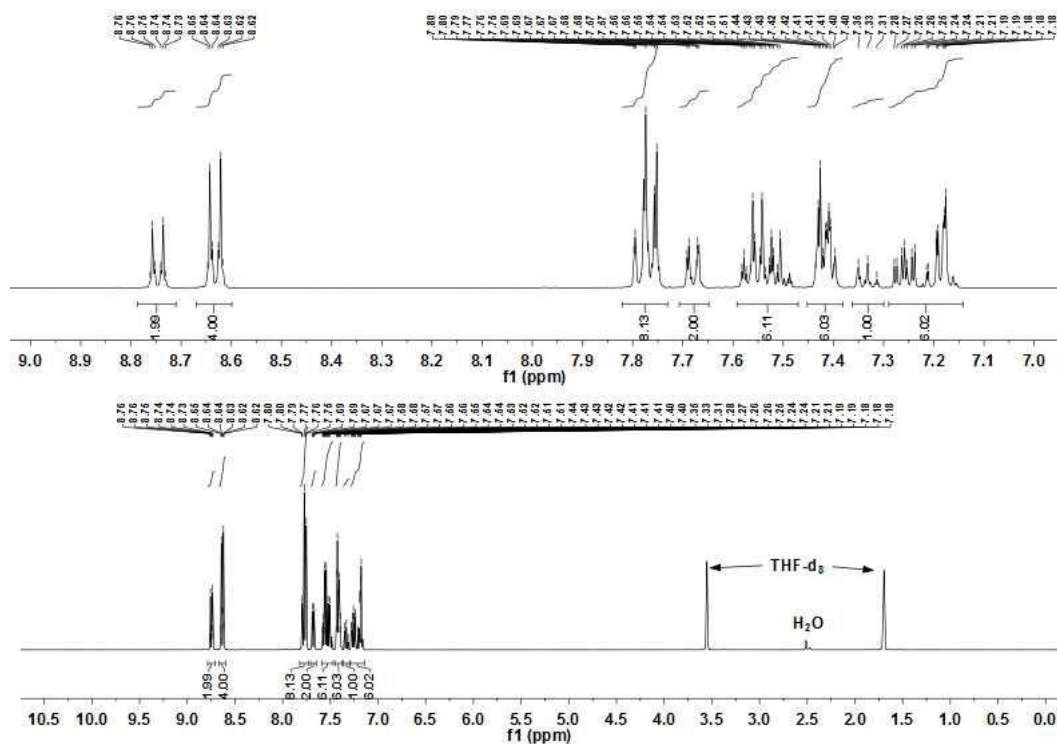


Fig.S1 ^1H NMR spectrum of CPL-1

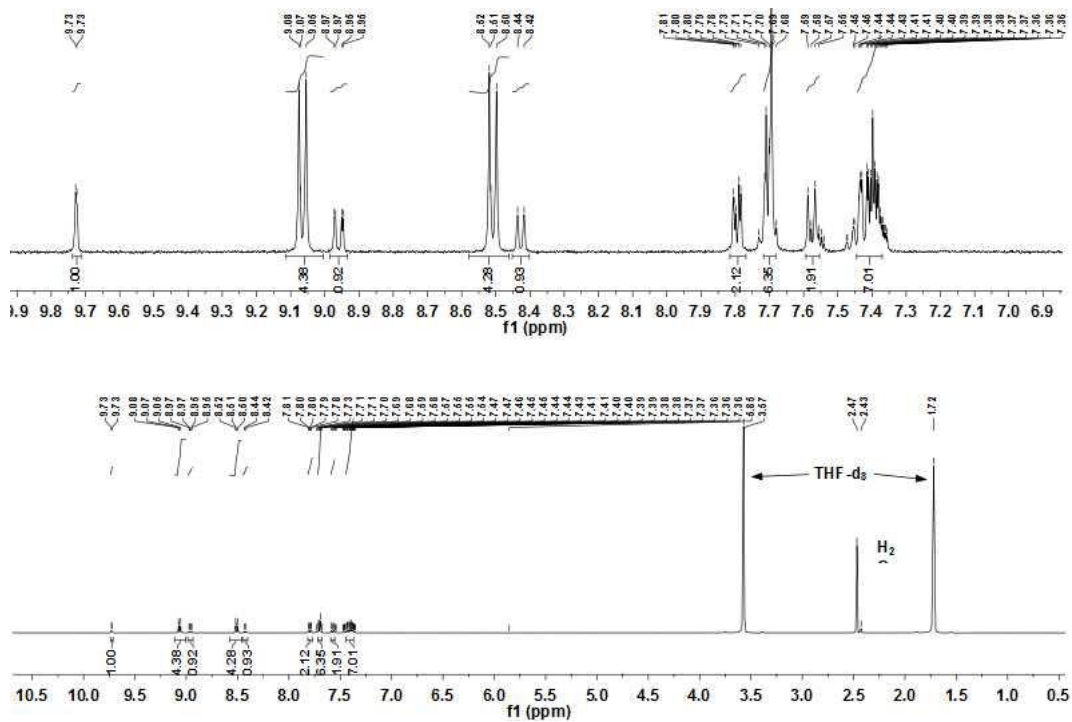


Fig.S2 ^1H NMR spectrum of CPL-2

Z105-ABP390-112 #2018-2073 RT: 20.22-20.77 AV: 56 SB: 181 0.87-2.68 NL: 1.21E4
T: ITMS + c APCI corona Full ms [150.00-2000.00]

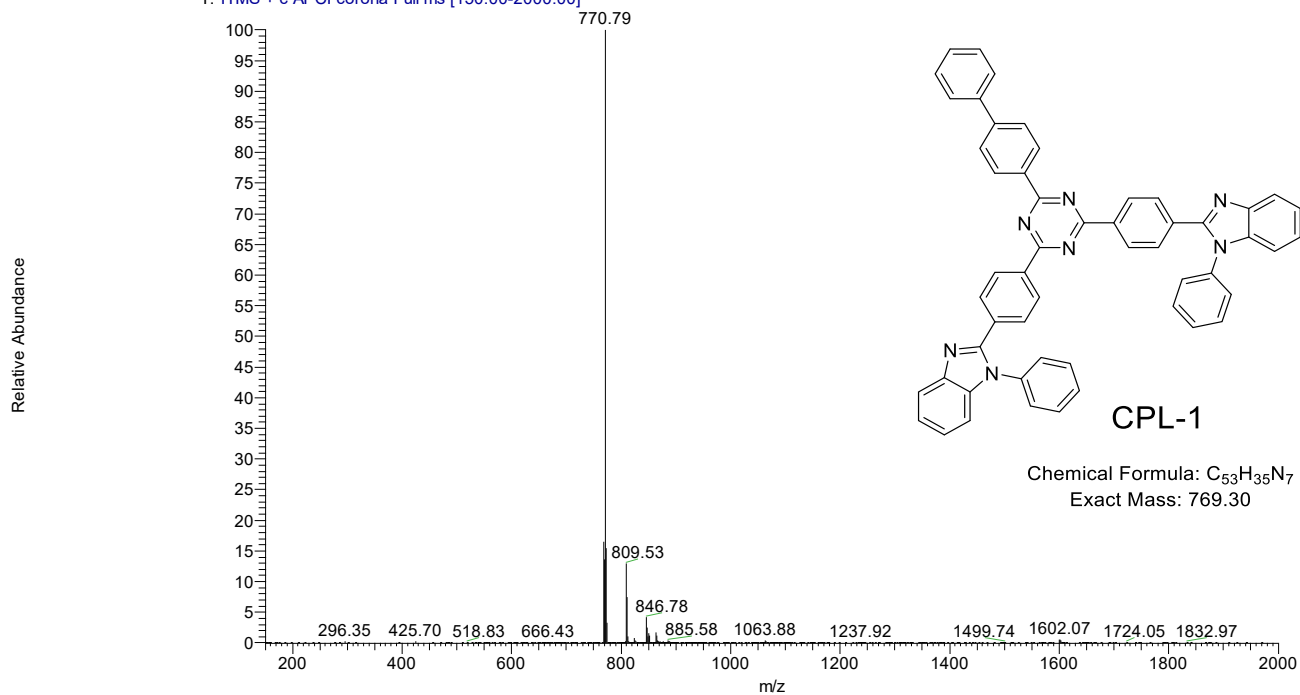


Fig.S3 MS spectrum $[M+H]^+$ of CPL-1

Z121-KGXP18273YZ #2084-2113 RT: 20.85-21.13 AV: 15 SB: 107 13.29-15.42 NL: 1.04E5
F: ITMS + c APCI corona Full ms [150.00-2000.00]

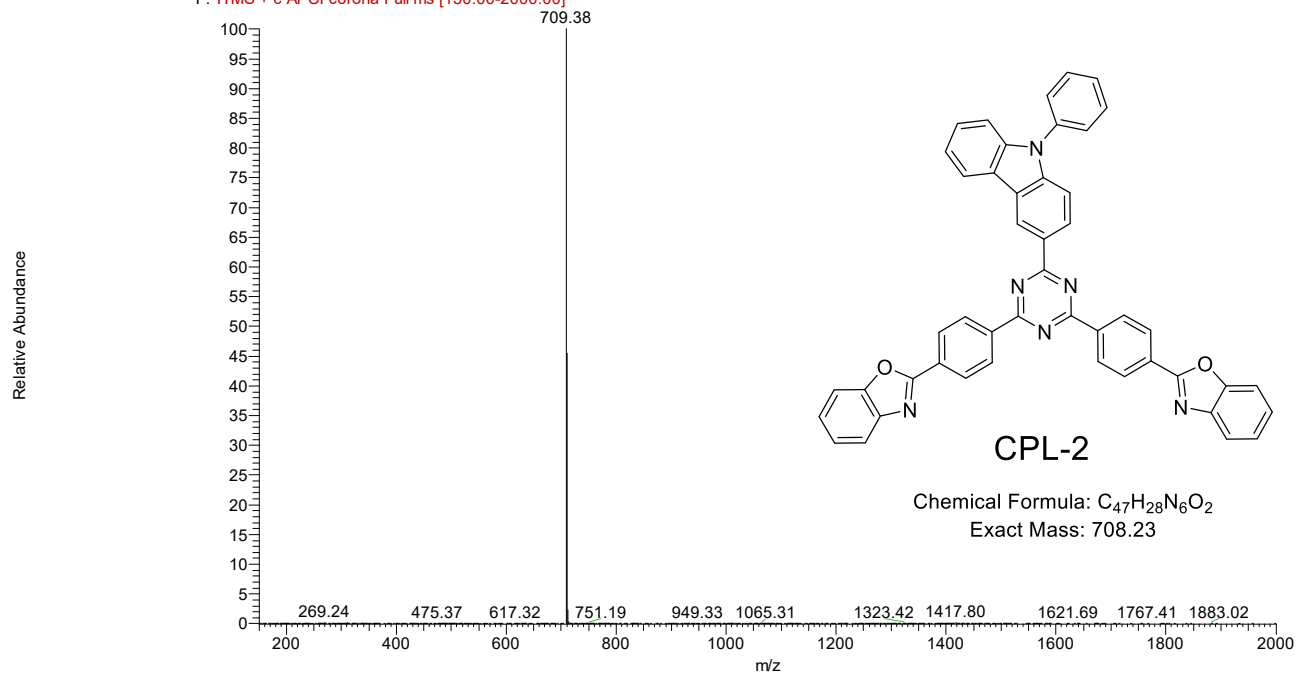


Fig.S4 MS spectrum $[M+H]^+$ of CPL-2

Conclusion

In this paper, hole-transport type material (electron blocking layer) is the main research content. At the same time, phosphorescent host material and capping layer material are also studied, and top light-emitting diodes are involved. In this paper, three categories of organic light-emitting materials were synthesized, including seven electron blocking materials, three phosphorescent host materials and two capping layer materials. The photophysical properties of these materials were comprehensively characterized, and the device performance of these materials were studied and evaluated.

BFS2A, **BFS3A**, **SF2DDA** and **SF4DDA** were synthesized by using seven membered cyclospiro and spirofluorene as basic units. Compared with the traditional electronic blocking materials **SF2AF** and **SF4AF**, the above materials can effectively improve the device efficiency and lifetime. When the film thickness is 50 nm, the maximum current efficiency of **BFS2A** and **BFS3A** are 10.46 cd/A and 9.26 cd/A respectively, and the lifetime (LT90) is 1592 hours and 1805 hours respectively, while that of **BFS2A** is 8.20 cd/A and the lifetime (LT90) is 724 hours. When the film thickness is 20 nm, the maximum current efficiency of **SF2DDA** and **SF4DDA** are 9.81 cd/A and 10.00 cd/A respectively, and the lifetime (LT90) of **SF2DDA** and **SF4DDA** are 430.46 hours and 420 hours, respectively, while the maximum current efficiency and LT90 of **SF4AF** are 9.35 cd/A and 429.25 hours, respectively. The experimental results show that the optical physical properties of the material can be effectively changed by changing the substituent point, thus improving the device performance and lifetime.

Furthermore, **DFBDDbA**, **BDFPDbA** and **BDFPDcA** were synthesized by using dimethyl-dihydroacridofuran as basic unit. It has high glass transition temperature and high triplet energy level, which is conducive to enhance the external quantum efficiency and lifetime of the device. Compared with TCTA, the EQE and lifetime of **DFBDDbA** are increased by 17% and 714%, respectively. The experimental results show that the material with dimethyl-dihydroacridofuran as the core can effectively improve the efficiency

and lifetime of the device when it is used as the electron blocking material by modifying the connecting group.

XanCarDipha, ***p*-XanCarDipha** and ***m*-XanCarDipha** were synthesized by using Xanthone as the basic unit and modified by bridge groups. The above materials are used as the host materials in green phosphorescent devices, and the performance and lifetime of the devices as single host and double host are studied respectively. The efficiency curves of **XanCarDipha** and ***p*-XanCarDipha** were significantly different due to the different combination of carbazole and Xanthone units. With ***p*-XanCarDipha: CarTria**. The maximum external quantum efficiency is 20.93% for the double host device and 16.86% for the single host device of ***p*-XanCarDipha**. The main reason is that the combination of ***p*-XanCarDipha** and CarTria can effectively improve the carrier balance in the emitting layer and inhibit the quenching of triplet excitons.

CPL-1 and **CPL-2** were synthesized by using triazine as basic unit. The material is applied to the top light-emitting diode as a capping layer. Compared with **CPL-ref**, **CPL-1** and **CPL-2** have better planarity and higher refractive index. Compared with the top-emitting diode of **CPL-ref**, the device efficiency of **CPL-1** and **CPL-2** are improved by 3.4% and 9.1%, and they have higher luminous brightness and smaller color deviation in the 0~75° viewing angle range.

In conclusion, the hole-transport type, phosphorescent host and capping layer organic luminescent materials were systematically studied in this paper. Several series of materials were designed and synthesized, and their application effects in organic light-emitting diodes were fully evaluated. The experimental results show that, compared with the traditional materials, several materials show excellent performance, and have potential application value in OLEDs.

Acknowledgment

This article is completed under the careful guidance of Professor Musubu Ichikawa. Here, I would like to express my sincerely respect and thanks to my teacher. No matter in the study or work, Professor Musubu Ichikawa has given me selfless care and help. Mr. Musubu Ichikawa's profound academic knowledge, rigorous academic attitude, active academic thought, full of enthusiasm for work, simple work style and noble personality charm have benefited me for life. I wish you good health, happy family and peace in your life.

Thanks for the teacher Professor Masahiro Suzuki and Professor Yoshinori Nishii for their concern for my scientific research support and life.

Thanks for the help and support in the experiment from the laboratory colleagues, especially in material synthesis, analysis and device fabrication, they are Yu Shi, Zhenhua Ci, from Valiant Co. Ltd...

Thanks for the support and help of colleagues from Jiangsu Sunera Technology Co., Ltd., they are Ming Cui, Chong Li, Zhaochao Zhang, Xiao Cai, Li Liang, Ying Lu and Haifeng Chen.

Special thanks to my parents, wife and other relatives. It is your silent dedication and unselfish care that have given me a strong spiritual motivation, so that I can concentrate on my study and research, and move forward bravely in the face of adversity.

Finally, I would like to thank all the teachers, classmates, relatives and friends who care and help me. I sincerely wish your good health and smooth work.

Appendix

Published Papers

(1) Baohua Hu, Xiao Cai, Chong Li, Wei Huang, and Musubu Ichikawa; “New xanthone derivatives as host materials: Improvement of carriers balance for high-efficiency green phosphorescent OLEDs using two host materials”, *Dyes and Pigments*, 178, 108333, (2020).

(2) Baohua Hu, Haifeng Chen, Chong Li, Wei Huang, and Musubu Ichikawa; “High-refractive-index capping layer improves top-light-emitting device performance”, *Applied Optics*, 59, 391419, (2020).

(3) Baohua Hua, Zhenhua Ci, Li Liang, Chong Li, Wei Huang, and Musubu Ichikawa; “Spiro derivatives as electron-blocking materials for highly stable OLEDs”, *Organic Electronics*, 86, 105879, (2020).

(4) Baohua Hu, Ying Lu, Zhenhua Ci, Chong Li, Wei Huang, and Musubu Ichikawa; “Electron blocking materials based on dimethyl-dihydrobenzofuran derivatives for highly efficient and long-lifetime blue fluorescent organic light-emitting diodes”, *Organic Electronics*, 87, 105916, (2020).